Spins, Disorder and Interactions in GaAs and Graphene

Inauguraldissertation

zur
Erlangung der Würde eines Doktors der Philosophie
vorgelegt der
Philosophisch-Naturwissenschaftlichen Fakultät
der Universität Basel

von

Dominikus Kölbl
aus Starnberg, Deutschland

UNI
BASEL

Basel, 2012

Genehmigt von der Philosophisch-Naturwissenschaftlichen Fakultät auf Antrag von

Prof. D. M. Zumbühl

Prof. C. van der Wal

Basel, den 22. Mai 2012

Prof. Dr. Martin Spiess
(Dekan)

Abstract

This thesis describes experiments on semiconductor spin physics under the influence of diverse disorder and carrier-carrier interaction. Motivated by recent observations of GaAs spin qubit coherence limited by hyperfine coupling to nuclear-spin ensemble fluctuations, we started out to find ways to study the electron-spin nuclear-spin coupling or to avoid the nuclear spin bath altogether. This can be done in several different ways and here we pursued two fairly different approaches. One is the investigation of the dynamics of nuclear spin polarization in GaAs and the other aims at spin-related effects in graphene nanostructures which possibly have negligible nuclear spin contributions due to the natural abundance ($\sim$99 %) of zero-spin isotopes.

The experiments on GaAs are performed using a non-local spin injection device with Fe ferromagnetic contacts on a degenerately n-doped epilayer. At low temperatures, where the injected spin polarization allows dynamic polarization of the nuclear spins via hyperfine interaction, distinct spin signals are used to study the dynamics of the nuclear spin system both in presence and absence of net electron spin polarization. The nuclear spin-lattice relaxation in an unpolarized environment reveals an unexpected breakdown of the Korringa law of nuclear spin relaxation otherwise valid for metallic systems. This is manifested in the observed deviation from a linear temperature dependence of the nuclear T_1 time and is interpreted as a result of hyperfine coupling to conduction electrons which are influenced by the interplay of disorder and carrier-carrier interaction. This finding therefore gives important insight into the strong influence of intimate coupling between the electron and nuclear spin sub-systems.

Transport experiments on lithographically defined graphene quantum dots are performed at low temperatures. Three graphene quantum dots of different nanometer sizes fabricated on a single graphene flake allow a detailed investigation of the size dependence of the Coulomb interaction, the energy spectra, and the influence of disorder within the nanostructures. The onset of Landau quantization in perpendicular magnetic fields reveals signatures of the electron-hole crossover reflecting the bandstructure symmetry of graphene. Suppression of orbital effects by applying external magnetic fields parallel to the sample plane allows to address spin effects of the charge transitions in the quantum dots. The observed field dependence of Coulomb blockade peak splittings is not inconsistent with the Zeeman splitting proportional to an expected g-factor of 2. The transport data evidence strong influence of disorder supposably induced by both charged impurities in the close vicinity of the quantum dots and by edge disorder as a result of the fabrication process lacking precise control of the edge structures.

Acknowledgments

First and foremost I wish to express my gratitude to Dominik Zumbühl not only for being the my PhD supervisor but also for all the scientific and personal input I enjoyed during the last couple of years in the Quantum Coherence Lab in Basel. In German, a PhD supervisor is often called *Doktorvater* which I understand to capture some of the father-and-son attribute (including motivation and admiration but also rivalry and frustration) of the relationship between a graduate student and the supervisor. I appreciate the work experience with Dominik as my *Doktorvater* who has always been a great source of physical understanding and an essential help with even the minor details of the experimental work.

I would like to thank the committee member professor Caspar van der Wal for his interest in my experimental work, reading the thesis, and for attending the thesis defense.

A great part of the research presented in this thesis was only made possible by the collaboration with IBM research in Rüschlikon. Therefore, I owe a lot to Santos Alvarado, Gian Salis and Andreas Fuhrer for the fabrication of the spin injection devices and for the patience in explaining the physics of spin valves and during the publication process.

In particular, I would like to thank Tony Clark: for being a great (and for along time the only) postdoc in our group, being of invaluable help especially with all problems concerning fridges and measurement setups and for becoming a good friend.

I would like to thank all members of the Zumbühl group for the friendly collaboration, vivid discussions, Bildungsviertelstunden and permanent exposure to Schwizerdütsch. In particular, I enjoyed sharing the office with Florian Dettwiler, Dorothee Hug, Lucas Casparis, Dario Maradan, and Leon Camenzind and sharing the labs additionally with Christian Scheller and Daniel Biesinger. Further, I want to thank Petar Jurcevic for setting up the 3-axis magnet, a very important ingredient of the setup for the spin transport experiments. I want to thank explicitly the former graduate students of our group, Sarah Heizmann, Kai Schwarzwälder, Charulata Barge, and Christine Bedner, for paving the way for the subsequent PhD projects by setting up the fabrication processes, labs, fridges and measurement setups. I would like to thank the later postdocs, Tai-Min Liu and Myrsini Lafkioti, for the valuable scientific and intercultural input to the group.

I also want to thank professor Christian Schönenberger and all the members from his group for very good collaboration in the cleanroom and the labs. Further, I thank for the desperate attempts to keep the MMM, shared with the group of Christian Schönenberger and the the group of Christoph Bruder, short and efficient.

Thanks to Dominik's scientific network, I had the pleasure to discuss some of the data with distinguished physicists during my PhD projects. I want to thank Daniel Loss, Guido Burkhard, Björn Trauzettel, and Dmitrii Maslov for explaining some theoretical aspects of the results and for the patience with the experimental deficiencies.

The experiments in our labs require a lot of support from many helping hands. I would like to thank the members of the mechanical workshop and the electronics workshop for the assistance and Dominik Sifrig for the flexible liquid-He supply. For all the administrative support I cordially thank Barbara Kammermann and Astrid Kalt who really ensure a comfortable start for everyone being new in Basel and are of great help at any time.

Within the four years in Basel I met many interesting people and found new friends certainly not requiring explicit listing. I am very thankful to everyone who made me feel welcome in Basel.

> *There is no doubt that it is around the family and the home that all the greatest virtues are created, strengthened and maintained.*
>
> – Winston Churchill

Contents

1 Introduction and Motivation

The great and ongoing success of semiconductor electronics is based on an impressive progress in integration density by miniaturization and in operation speed by use of high-mobility devices. Altogether this had a tremendous effect on the economic success of the semiconductor industry and lead to quite substantial changes to how we live and work today. However, obstacles of physical nature rather than technological problems are believed to get into the way of continuous progress of semiconductor technology in the near future. This means that there is a strong need for new approaches to circumvent the fundamental limits in miniaturization, power consumption and operation-speed of charge-based devices.

Spintronics and spin quantum computation are two promising ideas for this quest and possibly offer outstanding improvements using a combination of highly-developed electronics and the unique prospects given by the spin degree of freedom [1]. Spintronics generally entitles the up-and-coming combination of spin properties with conventional electronics possibly adding functionality to established devices or helping to circumvent the obstacles on the semiconductor road map of ever-growing operation speed, miniaturization and cost reduction [2]. On the contrary, the ambitious field of quantum computation implies a paradigm shift using coherent superpositions of quantum mechanical states, instead of the conventional binary logic, for the realization of a completely new kind of algorithms expected to offer an incomparable boost in computational power [3–5].

Today, spintronics and spin quantum devices are widely studied topics, which became pretty established over the years in conventional semiconductor materials like gallium arsenide and silicon. Gallium arsenide (GaAs) offers some technologically relevant key aspects for present high-performance components and most likely for the new device concepts to come, both for high-speed applications and spin-based logic and memory devices. Due to its direct bandgap it is also the material of choice for optical operations and opto-electronic interfaces. The modern techniques of nano-structuring via sophisticated lithography processes on extremely clean heterostructures provides the necessary controllability and flexibility for the study of spins in these distinct devices dominated by quantum effects [6, 7].

Graphene, though a zero-bandgap semiconductor only arising within the last ten years, is another promising material which apart from prominent scientific interest possibly is of technological importance including applications for charge, spin, and heat transport. As graphene is a fairly new material much less is known (experimentally, at least) about actual applicability for electronic and in particular spin-based devices. Although graphene has already been studied for a long time theoretically and has been first synthesized as a segregation layer on a metal surface in the 1970's [8], its actual stable existence has only been shown experimentally in 2004 by A. Geim and K. Novoselov [9], awarded with the Nobel prize in 2010. Apart from many other outstanding properties (see chapter 2.2 and [10, 11]) graphene is believed to be superior in terms of spin coherence in a solid state system [12]. In particular, spin qubits in graphene quantum dots are predicted to have almost ideal properties due to comparably weak decoherence effects like low spin-orbit coupling and vanishing hyperfine interaction in natural carbon materials [13]. Further, the unique symmetry of the graphene bandstructure combined with the astonishing Klein-tunneling of its massless quasi-particles facilitates a very special non-local coupling possibly enabling fault-tolerant quantum computation [14, 15].

The subject of this thesis are investigations of spin properties in both GaAs and graphene applicable to the field of spintronics and solid state spin quantum computation [1]. The presented experiments are motivated by the quest to understand and possibly eliminate perturbing effects that induce electron spin relaxation and limit coherence times in spintronics and quantum computation devices. Electron and nuclear spin properties of GaAs are studied in an all-electrical spin transport device over a temperature range between 20 K and down to 100 mK. In the new material graphene, experimental investigations, though potentially very exciting, typically bare complications in the fabrication processes and in the sample characterization. Still, we managed to investigate confined charge carriers and their spins in graphene quantum dot structures. Both systems share the strong influence of various kind of disorder and carrier-carrier interactions. Whereas current graphene nanostructures generally all suffer from significant disorder induced by the fabrication processes, we deliberately chose a relatively low doping level in the disordered (and interacting) regime for the GaAs study where spin lifetimes are longest. In this low-density metallic GaAs for instance, we observe a surprising deviation from the expected Korringa law of nuclear spin relaxation at low temperatures which we understand as a result of the combined influence of disorder and interactions within the electron system.

The presentation of the work is structured as follows:
The body text begins in chapter 2 with a detailed discussion of the background relevant for our experiments, which starts with an introduction to the electronic and spin properties of gallium arsenide and graphene, respectively. In addition, the metal insulator transition in doped semiconductors is discussed as it is of some relevance for the results presented in chapter 4. The basics of electron and nuclear spin relaxation are given with the focus on effects applicable to the present experiments on bulk n-doped GaAs in chapter 3 and 4 and graphene quantum dots in chapter 5. Further, the principles of electrical spin-injection and non-local spin valve devices are introduced.

In chapter 3, the nuclear environment of electrons in the n-doped GaAs lattice is studied at low temperatures using lateral spin-valve devices as a model system. Different signatures of nuclear spin polarization are presented for various experimental configurations, magnetic fields and temperatures.

A new method for the measurement of nuclear spin relaxation in a spin valve device is established by the experiments presented in chapter 4. The intriguing result is an observed invalidness of the naively expected Korringa law of linear temperature dependence otherwise valid in an extremely wide range of metallic solids including doped semiconductors. The possible relaxation mechanisms of the nuclear spins are discussed and compared to our observations. Further, the experimental signatures of inhomogeneities and dynamics of the nuclear spins in presence of polarized electrons are discussed.

In chapter 5, low-temperature transport experiments in graphene quantum dots including electron spin effects are presented. Three graphene quantum dots of different sizes below 100 nm are fabricated on a single graphene flake via a combination of e-beam lithography and oxygen plasma-etching. The size-dependence of the transport properties of the graphene quantum dots in in-plane and perpendicular magnetic fields is investigated. The experimental data reveal a strong influence of disorder on the transport features commonly observed in state of the art graphene nanostructures. Nevertheless, experimental evidence for Landau quantization in perpendicular magnetic fields marking the electron-hole crossover and spin-related effects of in-plane fields are observed.

Finally, future experiments, on both GaAs spin-valves and graphene quantum dots, based on the presented findings are proposed and first experimental steps towards improved graphene nano-structuring are shown in the outlook, chapter 6.

2 Background

2.1 GaAs spin- and electronic devices

For the semiconductor technology GaAs with its high carrier mobility is of interest for specialized high-frequency applications widely used in the telecommunication infrastructure and in particular mobile electronic devices [16]. The GaAs crystal is a zincblende structure and the bandstructure forms a direct bandgap of 1.42 eV between the conduction band and two valence bands (heavy- and light hole) making it important for many optical applications in light emitting diodes, lasers and detectors where it acts as an opto-electronic interface [16, 17].

From the scientific point of view, GaAs is of great interest because it has proven to be a versatile testing ground for new physics and novel device concepts. This is due to various technical reasons among which are its possibly high carrier mobilities and the associated extremely long mean free paths allowing ballistic transport experiments in mesoscopic and nano-scaled devices achieved in clean growth processes of bulk crystals and heterostructures. Semiconductor heterostructures leading to a two-dimensional electron gas (2DEG) of charge carriers in a triangular potential well at the interface facilitate convenient electrostatic tuning of carrier densities and additional confinement to nanostructures, like 1D wires or quantum dots, using metallic surface gates. In these structures many exciting effects have been observed reaching from the integer and fractional quantum Hall effect [18–20] over single-mode quantum-wire transport [21] to realization of single electron spin relaxation times up to $T_1 \simeq 1$s [22] and coherent manipulation of single spins in quantum dots [7, 23, 24].

Further, the GaAs crystal properties and modern growth processes not only allow the combination with other semiconductors (e.g. AlGaAs/GaAs heterostructures) but are also compatible with incorporation of magnetic elements (e.g. MnGaAs) resulting in semiconducting magnetic materials which are of technological importance for possible future spintronics devices [1, 25]. Overall, GaAs is a promising material for the realization of novel devices in the field of spintronics and spin quantum computation and is therefore subject of many investigations.

2.1.1 Properties of doped semiconductors

The success of semiconductor electronics relies to a great deal on the extreme tunability of semiconductor properties by the use of doping and electrostatic gating. Doping is done by replacing a fraction of atoms in the otherwise very clean semiconductor lattice by atoms from neighboring groups in the periodic table. This creates either acceptor or donor states within the bandgap of the intrinsic semiconductor. As a consequence, the Fermi-energy is shifted towards the conduction band edge for n-doping or the valence band edge for p-doping. Therefore it is possible to tune a specific semiconductor material from insulating behavior, where all charge carriers are localized at low temperatures, to a metallic state, where the Fermi-energy resides within an (impurity-) band down to lowest temperatures. Associated with this doping range is a change of the low-temperature conductivity by more than six orders of magnitude [26], impressively demonstrating the great flexibility of semiconductor electronic devices. Moreover, similar dynamic ranges are attained by tuning magnetic field or pressure instead of doping [27, 28].

Starting from an extremely pure crystal (intrinsic SC) the $T = 0$ electrical properties change by addition of doping atoms from insulating behavior, where all charge carriers are frozen out in a completely filled band, to a regime of hopping conduction between impurity sites described by percolation models [28]. It is clear though, that the charge transport mechanism will change fundamentally when the density of doping atoms is increased even further and the conductivity starts to be quasi-metallic[1].

The impurity band

To understand the effect of doping on the electronic properties of semiconductors it is necessary to recognize the influence of the donors on the band structure of the crystal. The following discussion is focused on n-doped materials, but the effects are similar for acceptors. After a certain doping density is reached, depending on the effective Bohr radius of the impurity given by the host material, the randomly placed shallow impurity states start to overlap and eventually form a quasi-continuum in the density of states

---

[1] The reason for the classification as *quasi-metallic* is that the zero-T conductivity is finite but much lower than in native metals

(DOS) at high doping densities. This is called the impurity band usually having all features of a disordered narrow band, though it is not comprised of Bloch states due to the absence of periodicity. In the case of compensation, meaning presence of acceptor impurities, the Fermi level is shifted from the center of the impurity band (half filling) towards the forbidden gap region, where states tend to be localized as a result of the random distribution of doping sites. If we further include Coulomb interaction between the charge carriers (e.g. using the Hubbard model) the impurity band splits into two narrow bands separated by an energy region of strongly suppressed density of states. In consequence one can distinguish three thermally activated transport regimes, each having a characteristic activation energy: (*i*) intrinsic conduction in the conduction band at highest T, (*ii*) conduction in the upper Hubbard (D^-) band at intermediate temperatures, and (*iii*) hopping conduction between donor sites at lowest temperatures. If the doping density is high enough and compensation and disorder allow the Fermi energy to lie in the central region of delocalized states in the impurity band, hopping conduction will be replaced by a metallic conductivity, which accordingly is not temperature activated.

2.1.2 The metal-insulator transition

The interaction-driven splitting of the impurity band mentioned in the previous paragraph is closely related to the *Mott transition.* This type of metal-to-insulator transition (MIT) was first described by N. F. Mott [29] as a consequence of Coulomb interaction between charge carriers energetically separating single- and double-occupied states if the overlap integral $I(\bar{r})$ of neighboring carriers with average distance $\bar{r}$ is small compared to the interaction. In this picture, the increase of impurity density (decrease of $\bar{r}$) leads to broadening of the upper and lower Hubbard band proportional to $I(\bar{r})$ eventually resulting in a metallic DOS distribution when both sub-bands overlap [28]. At decreased doping densities the lower impurity band is completely filled as every donor only contributes a single charge carrier and the system is therefore insulating at $T = 0$.

Another kind of MIT is a result of disorder, instead of interaction, and is called *Anderson transition* [30]. The disorder which is driving the system into an insulating regime in this model is given by the distribution of donor energies or the random lateral distribution of donor sites naturally present in doped semiconductors. If the disorder strength is increased relative to the band width, a growing fraction of states in the tails of the impurity band is bound to the donors. If the disorder exceeds some critical value, all impurity states are localized even in this single-particle picture and the impurities do not contribute to low-temperature transport [28].

In general, the transition in a doped semiconductor will be an *Anderson-Mott* transition, meaning that it is induced by the concurrent presence of both disorder and electron-electron interaction. This specific regime, though it is very common not only in doped semiconductors, still lacks a comprehensive theoretical description in the transition region. However, phenomenological models motivated by some experiments on thermodynamic properties in this regime do exist. One of them is the 2-fluid model [31–34] describing the MIT as a rather smooth transition where localized spin-moments extent from the insulating into the metallic side of the MIT where they are in coexistence with itinerant conduction electrons. This gives rise to a diverging susceptibility and an anomaly of the specific heat (Schottky hump) close to the MIT [35] in agreement with experiments on doped IV-semiconductors [34, 36]. Which mechanism is actually forming these localized moments in the metallic phase and further stabilizes them against Kondo-screening by the conduction electrons or quenching by RKKY interaction is a question still lacking a conclusive answer.

A modern theoretical approach to this specific regime might be statistical dynamic mean field theory [37]. With this method the influence of both the electron-electron interactions and disorder can be included simultaneously leading to a non-Fermi liquid phase on the metallic side of the MIT characterized by the coexistence of localized and delocalized electron states. This phase has been shown to be closely related to the *Griffith's phase* of heavy fermion systems [35, 38] and its specific properties are therefore not captured by any model within a simple free-electron gas picture [39]. This means that special care has to be taken when applying physical laws derived for purely metallic systems to materials in this specific regime.

2.2 The physical properties of graphene

The group IV element carbon is among the most important elements we know, as it is the fundament of all organic chemistry and with that for life. The great variety of chemical and physical properties found in the virtually unlimited diversity of carbon structures is primarily given by the underlying bonding among the atoms and by their dimensionality.

The solid-state allotropes of carbon are divided into two classes. First there is the diamond class where all atoms form four covalent bonds via sp^3-hybridized orbitals. The resulting pure crystal has very prominent mechanic and optical properties but is an insulator as all valence electrons participate in forming the lattice. Via insertion of impurities diamond turns into a wide-bandgap semiconductor and the unique NV-centers, a combination of a nitrogen impurity with a neighboring vacancy, has attracted much research interest as they form very stable single-spin systems [40, 41].

The second class comprises all allotropes made up of sp^2-hybridized carbon atoms which are therefore covalently bond to three partners leaving the fourth valence electrons to form delocalized π-systems. This makes these materials generally well conducting and mechanically very stable as the tight covalent bonds making up the trigonal lattice are even stronger than within diamond. The prototype in this class is a single-atom thick layer of carbon atoms in a honeycomb structure of hexagons, called graphene. A stack of graphene layers, weakly coupled by van-der-Waals forces, forms the 3D structure graphite, well-known for ages. Particular important carbon structures results from stacking of two (bilayer) or three (trilayer) graphene layers forming the intermediate system between graphene and graphite but having special features. By rolling up a narrow graphene layer and reconnecting the carbon bonds one-dimensional carbon nanotubes are obtained [42]. Further, by incorporation of pentagons into the honeycomb lattice a curvature is geometrically induced eventually forming zero-dimensional fullerenes [43].

Here, we focus on the physics of graphene dominated by its prominent bandstructure and the strictly two-dimensional nature together evoking an anomalous quantum Hall effect [44, 45] and possibly mimic features of quantum electrodynamics on the solid-state level [46].

2.2.1 The Dirac spectrum of graphene

The hexagonal lattice of graphene has primitive lattice vectors $\mathbf{a}_1 = a_0(1,0)$ and $\mathbf{a}_2 = a_0(\frac{1}{2}, \frac{\sqrt{3}}{2})$ which form the unit cell containing two atoms A and B with a distance $a_0 = 1.42$ Å. The reciprocal lattice is again hexagonal. The important features of the bandstructure at low energies can be obtained by tight-binding methods using a linear combination of Bloch wavefunctions $\Psi_n(\mathbf{k},\mathbf{r}) = \sum_i b_i\, e^{i\mathbf{k}\cdot\mathbf{r}}\Phi_i(\mathbf{r})$ set up from the atomic p_z-orbital wavefunctions $\Phi_i(\mathbf{r})$ at site i [47]. Generally, the eigen-energies are then given by

$$E_n(k) = \frac{\left\langle \Psi_n|\hat{H}|\Psi_n \right\rangle}{\langle \Psi_n|\Psi_n \rangle} \tag{1}$$

and the eigen-value problem has a simple solution when only considering nearest-neighbor interaction with the overlap integral $s = \langle \Phi_A(r_A)|\Phi_B(r_B)\rangle$ and the nearest-neighbor hopping amplitude $\gamma_h = \left\langle \Phi_A(r_A)|\hat{H}|\Phi_B(r_B) \right\rangle$. Setting the on-site energies of the atomic wavefunctions to zero one gets the result

$$E(k) = \frac{\pm\,\gamma_h|\alpha(k)|}{1 \pm\, s|\alpha(k)|}\ , \tag{2}$$

$$|\alpha(k)| = \sqrt{1 + 4\cos\left(\frac{3ak_y}{2}\right)\cos\left(\frac{\sqrt{3}ak_x}{2}\right) + 4\cos^2\left(\frac{\sqrt{3}ak_x}{2}\right)}\ . \tag{3}$$

This is plotted within the first Brillouin zone in Fig. 1 using $\gamma_h = -2.9$ eV and $s = 0.1$ where the latter ($s \neq 0$) induces the slight asymmetry between electron and hole states away from zero energy [47, 48]. The low-energy dispersion at the symmetry points $\mathbf{K}, \mathbf{K}'$ is obtained by a linear expansion using $\mathbf{k} = \mathbf{K} + \boldsymbol{\kappa}$ and $E(\mathbf{k}) = E(\mathbf{K}) + \epsilon(\boldsymbol{\kappa}) = \epsilon(\boldsymbol{\kappa})$, where $\boldsymbol{\kappa}$ is the wavevector measured relative to the $\mathbf{K}(\mathbf{K}')$ point. This gives the eigen-energies

$$\epsilon(\kappa) = \pm\frac{3\gamma_h a_0}{2\hbar}\,|\boldsymbol{\kappa}|\ , \tag{4}$$

which is equivalent to $\epsilon(\kappa) = \pm\hbar v_F|\boldsymbol{\kappa}|$ as the velocity of the wavepaket at the Fermi energy is given by $v_F = \hbar^{-1}\partial\epsilon/\partial\kappa \approx 10^6$ m/s [49]. This linear dispersion reflects the massless nature of the low-energy quasi-particles in graphene which is therefore analogous to relativistic Dirac particles except for the reduced velocity $v_F \simeq \frac{1}{300}\,v_c$, v_c being the speed of light. The effective value of v_F has been found to be slightly changed upon inclusion of interaction making the Dirac cones around K, K' more narrow [50].

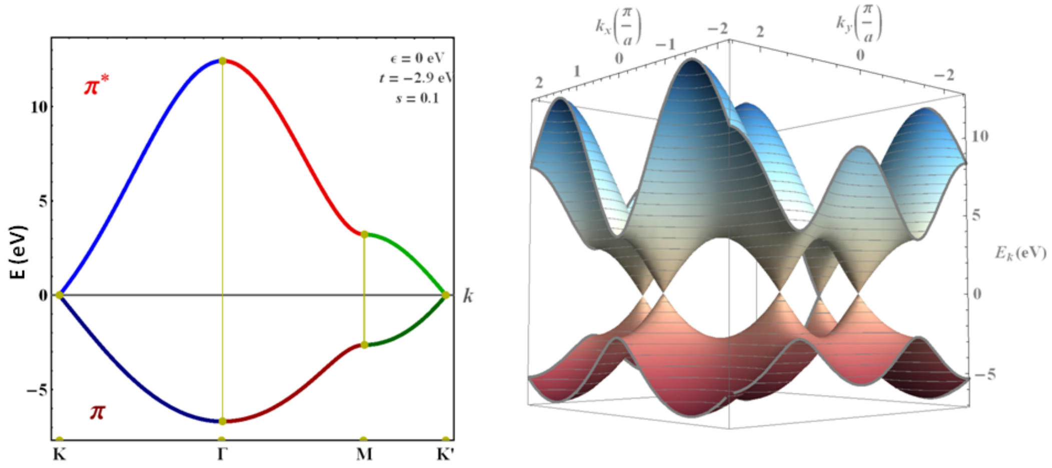

Figure 1: **Dirac spectrum of graphene.** The bandstructure of graphene (left) as calculated by the tight-binding method given by equation (2) and (3) using a nearest-neighbor hopping integral of $\gamma_h = -2.9$ eV and an overlap integral $s = 0.1$ giving the asymmetry between the π-bonding and the π^*-antibonding band. The Brillouin zone center is at $\mathbf{\Gamma}$ and $\mathbf{M}$ is at the saddle point between the characteristic cones at the zone boundary. To the right the 2D dispersion with the degeneracy points at $\mathbf{K}, \mathbf{K}'$ is shown within the first Brillouin zone [51]. The linear dispersion at low energies results in the massless nature of the quasi-particles in graphene.

Further, at higher energies the three-fold lattice symmetry leads to trigonal warping of the Dirac cones.

The bandstructure of graphene is therefore very distinctive and also differs from bilayer and trilayer graphene systems which have a non-zero band mass due to band curvature induced by the interlayer coupling.

2.2.2 Chirality and Klein tunneling

The linear dispersion around the K, K' points is not enough to understand the intriguing properties of graphene. The effective Hamiltonian with eigenvalues given in equation (4) can be written in the form of a Dirac-Weyl Hamiltonian

$$\hat{H}_{\mathbf{K}} = \pm \hbar v_F \, \hat{\boldsymbol{\sigma}} \cdot \boldsymbol{\kappa} \tag{5}$$

with the Pauli matrices $\hat{\boldsymbol{\sigma}} = (\sigma_x, \sigma_y)$ acting on the *pseudo-spin* vector (Φ_A, Φ_B) [52]. As it turns out, this Hamiltonian has eigenvectors which have their two-component spinor (Φ_A, Φ_B) coupled to the direction of the momentum $\boldsymbol{\kappa}$:

$$\begin{pmatrix} \Phi_A \\ \Phi_B \end{pmatrix} = \frac{1}{\sqrt{2}} \begin{pmatrix} \pm e^{i\varphi/2} \\ e^{-i\varphi/2} \end{pmatrix} \,, \tag{6}$$

with the angel $\varphi = arg(\kappa_x + i\kappa_y)$. This is a direct consequence of the sublattice symmetry of graphene and implies that around the symmetry points right-moving states ($\partial\epsilon/\partial\kappa > 0$) are comprised of wavefunctions Φ_A whereas left-movers ($\partial\epsilon/\partial\kappa < 0$) are comprised of wavefunctions Φ_B [53][2]. This helical nature of the quasi-particles is called the chirality of graphene. Another result of the dependence of the eigenvectors on the direction of the momentum is the appearance of a sign-change upon a 2π rotation in k-space ($e^{i\pi} = -1$) indicating a Berry's phase of π, a characteristic feature of spinors (e.g. real physical spin of an electron).

The chirality of the quasi-particles has an important effect on the transport properties of graphene. For example, the intrinsic mobility is expected to be very large since a backscattering event requires an inter-valley transition with large momentum transfer or a pseudo-spin flip which can only be induced by short range impurity potentials differing between sublattice A and B [54].

A related effect of the chirality is the transmission through a barrier with probability one (at normal incidence). This is the well-known Klein paradox of relativistic particles [55]. In graphene this results from the fact that any electron impinging on a barrier meets a counter-propagating hole within the barrier region with the same pseudo-spin enabling perfect tunneling [53, 56, 57].

Combined with the absence of a bandgap in graphene, it is therefore not possible to confine charge carriers by local electrostatic gating, a versatile technique widely used in conventional, gapped 2D systems to create local barriers defining quantum wires, quantum point contacts or quantum dots. Hence, for the study of similar nanostructures in graphene it is necessary to employ alternative techniques of confinement, one of which is presented in chapter 5 where graphene structures are cut down to nanometer-sized samples which possibly gives rise to a confinement gap and allows disorder induced Coulomb blockade effects.

---

[2] In other words: the pseudo-spin vector is parallel to the momentum for electrons and anti-parallel for holes in graphene.

Minimum conductivity of graphene

Another aspect of the transport properties of Dirac particles linked to the inability of 2D localization due to the chirality and Klein tunneling is the conductivity at zero energy. From a classical point of view the conductivity $\sigma(E = 0)$ at the Dirac point given by the Einstein relation $\sigma = e^2\rho(E_F)D_c$, with the charge diffusion constant D_c, is expected to be zero due to a vanishing density of states $\rho(E_F)$. However, a quantum description predicts a finite conductivity of $\sigma_0 = \frac{4}{\pi}\frac{e^2}{h}$ even at zero density with the factor 4 accounting for spin and valley degeneracy [58, 59]. This value is considered universal for infinite graphene without interaction and disorder [60, 61]. In experiments, the Dirac point is typically not accessible due to charge inhomogeneities leading to broadening and an effective minimum residual density n_s at the charge neutrality point (CNP). Even for high-mobility samples, where n_s is typically small, the observed minimum conductivity is spread with typical $\sigma_{min} \gtrsim 3\frac{e^2}{h}$ [45, 62–64] and the non-universality (and e.g. the missing π) is attributed to effects of sample geometry [58] or charged impurities [65, 66].

Due to the ultra-thin (2D) nature of graphene the whole system can be considered to be at the surface and therefore it is extremely susceptible to all kinds of disturbances from the outside: charged impurities on top and below the graphene layer or within the substrate, dislocations within the lattice, ripples and phonons. All of them will influence the conductivity measured at the CNP and might contribute to the formation of electron-hole puddles observed close to the CNP giving rise to the residual density n_s and a percolation network of n- and p-doped regions [67].

Figure 2 shows measurement data from a 1 μm wide graphene Hall-bar device[3] with an aspect ratio of 1:3 (see SEM picture in inset Fig. 2) taken at T = 4K. The carrier density n is tuned by the applied backgate voltage V_{BG} with $n = \alpha\, V_{BG}$ and $\alpha = 7.9 \times 10^{10}$ $\mathrm{V^{-1}cm^{-2}}$. The prefactor α was extracted from the backgate dependence of the Hall slopes ($\rho_{xy}(\mathrm{B}) = \frac{B}{en}$) in perpendicular magnetic fields and is consistent with a simple parallel plate capacitor model. We observe the expected linear density dependence of the conductivity following the Drude model $\sigma - \sigma_0 = e\,\mu\,n$ with a constant mobility μ

---

[3] The large area graphene flakes presented in the thesis are purchased from *Graphene Industries Ltd.*, Manchester. More information on the sample fabrication are given in chapter 5.2.

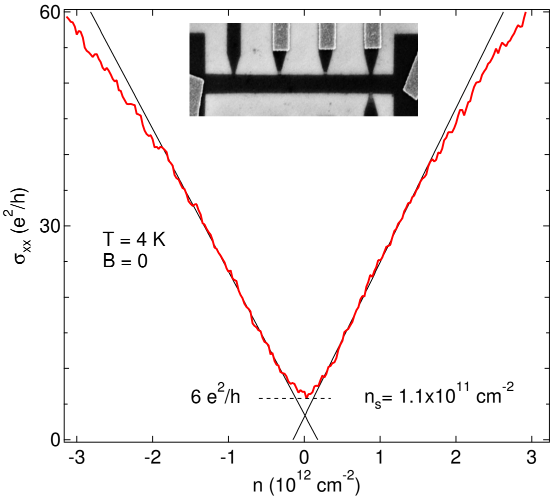

Figure 2: **Field effect and minimum conductivity in a graphene Hall-bar device.** Four-terminal conductivity (red) of a 1 μm wide Hall bar device (inset: SEM picture) as a function of density, tuned by the backgate voltage, at T = 4 K (current bias of 1 nA). Apart from the expected linear density dependence (see line fit, black) for intermediate densities, we observe a saturation close to charge neutrality with a finite value of $\sigma_{xx} \sim 6 \times e^2/h$ corresponding to a residual minimum density $n_i \sim 1.1 \times 10^{11}$ cm^{-2}.

for moderate densities (see line fit, black). Around the CNP the conductivity saturates at a finite value of $\sim 6\, e^2/h$, which indicates a corresponding minimum residual density $n_s = 1.1 \times 10^{11}$ cm^{-2} at the CNP when compared to the fitted Drude model. These findings are consistent with theory models for the influence of charged impurities [65] and with similar experiments [66, 68] on samples where n_s is not explicitly low. The sample quality of our device is fairly limited as indicated by an average mobility of $\sim$ 2000 cm^2/Vs extracted from Hall measurements at a density of $n = 1 \times 10^{12}$ cm^{-2} in low perpendicular magnetic fields. The sub-linearity of σ_{xx} at elevated densities, where long-range charged-impurity potentials are effectively screened, is generally referred to an increasing influence of ripples and short-range scattering away from the CNP [62, 66, 69].

2.2.3 The anomalous quantum Hall effect in graphene

When graphene is placed in a magnetic field, the according action is incorporated into the Hamiltonian given in equation (5) by the customary substitution of the momentum operator $\boldsymbol{\kappa} = -i\nabla \rightarrow -i\nabla + \frac{e}{\hbar}\mathbf{A}$, where $\mathbf{A}$ is the vector potential of the field. This

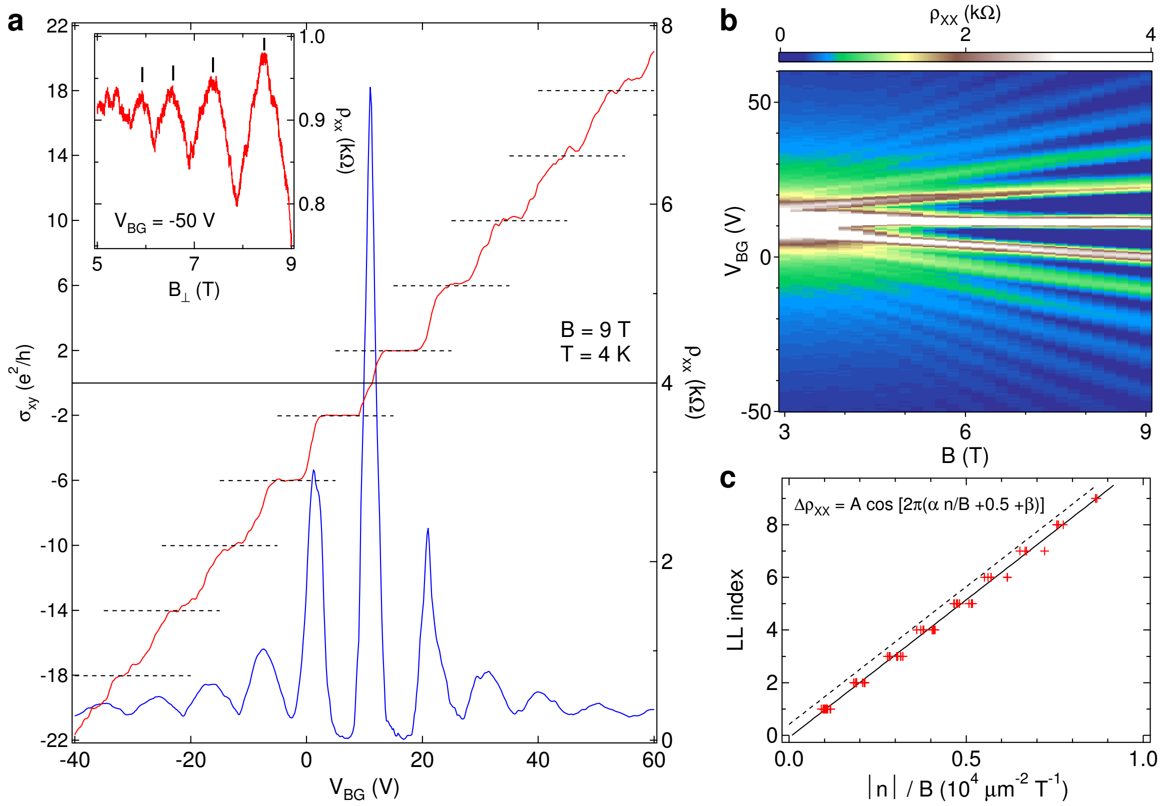

Figure 3: **Probing the Dirac spectrum of graphene via magnetotransport. a,** Longitudinal resistivity and transversal conductivity measured in a perpendicular field of 9 T. The dashed lines indicate the expected values of the half-integer quantum Hall effect. The inset shows Shubnikov-de Haas oscillations at high hole-density and large fields. **b,** Longitudinal resistivity as a function of backgate voltage ($\propto$ density) and perpendicular magnetic field. The characteristic Landau-level fan reflects the electron-hole symmetry and the Dirac physics of the graphene charge carriers. **c,** Analysis of the Shubnikov-de Haas oscillations pattern shown in **b,**. Plotted is the LL index versus n/B of the according maxima in ρ_{xx} expected to give a line according to equation (9). The solid line is a fit giving good agreement with expectations (see text) with $\alpha = 1.046\,(\pm 0.008)$ mT $\mu\mathrm{m}^2$ and $\beta = -0.585 \pm 0.031$ to be compared with conventional 2D systems with a Berry's phase of integer multiples of 2π (dashed line, β=0).

results in a Landau level (LL) spectrum given by [70]

$$E_N = \pm v_F \sqrt{2e\hbar B\,|N|} \tag{7}$$

with the LL indices $N = 0, \pm1, \pm2, \ldots$. Compared to conventional 2D systems with $E(N) = \hbar\omega_C(N + \frac{1}{2})$ there are two strong distinctions. First, equation (7) allows a Landau level at zero energy which is comprised on equal parts of electrons and holes, directly reflecting the bandstructure symmetry and therefore is also observed in bilayer graphene[4]. Second, the Landau levels are not equally spaced in energy, a consequence of the linear increase of the density of states. As the surface potential at the edges of the sample increases the energy of the electrons whereas it equally decreases the energy of the holes the zeroth LL is split and forms separate edge states of transport for the two types of carriers. Accordingly, the first edge state above (or below) $E = 0$ has only half the degeneracy of the edge states of higher LLs which are solely comprised of electron or hole states with a degeneracy of four (spin + valley) [45]. This gives a half-integer sequence (in units of $4\frac{e^2}{h}$) of transverse conductivity plateaus in the quantum Hall regime:

$$\sigma_{xy} = 4\,\frac{e^2}{h}\,(N + \frac{1}{2})\,, \tag{8}$$

where the factor of 4 again accounts for the degeneracy of spin and pseudo-spin in graphene. From the theoretical perspective, this shifted sequence is a manifestation of a Berry's phase of π in graphene.

A typical measurement is shown for our Hall-bar device in Fig. 3a, varying the charge carrier density with the applied V_{BG} at 9 Tesla. The peaks in ρ_{xx} (blue) at the LL-energies following eq. (7) where scattering between edge-states through the bulk is allowed and the quantized plateaus in σ_{xy} (red) given by eq. (8) as indicated by the dashed lines nicely agree with the expectations. As the Landau levels are broadened by disorder and temperature, the plateaus at higher N get smeared out and the peaks in ρ_{xx} start to overlap since the LL spacing shrinks following equation (7). The influence of small angle scattering by disorder on the LL width can be used to test the strength of disorder in graphene devices. In chapter 5, we use this to check the homogeneity of the

---

[4] In bilayer graphene the inter-layer symmetry can be broken by a potential difference between the layers which induces a bandgap and leads to the disappearance of the zeroth Landau level [71]

disorder potential across a large area graphene flake with several devices. The longitudinal resistivity ρ_{xx} (blue) quite prominently marks the zero-energy LL at $V_{BG} \approx 11.0$ V indicating (chemical) hole-doping possibly due to adsorbates or fixed charges in the environment both of which are possible sources of charge inhomogeneities. Further tests of the Dirac spectrum in graphene are possible via measurements of the Shubnikov-de Haas (SdH) oscillations of ρ_{xx} (see inset Fig. 3a) as a function of density n and magnetic field B shown in Fig. 3b. Theory predicts an oscillation pattern [44, 45]

$$\Delta\rho_{xx} = A \cdot \cos\left[2\pi\left(\alpha\frac{n}{B} + \frac{1}{2} + \beta\right)\right] \tag{9}$$

where $\alpha = \frac{\Phi_0}{f}$ is the magnetic flux quantum $\Phi_0 = 4.14$ mT μm^2 divided by the band degeneracy f and β is the Berry's phase in units of 2π. In Fig. 3c the analysis of the data from 3b is shown (red) and a line fit (solid black) giving $\alpha = 1.046\,(\pm 0.008)$ mT μm^2 and $\beta = -0.585 \pm 0.031$ is in very good agreement with the theory for graphene including a degeneracy of $f = 4$ ($\alpha = 1.035$ mT μm^2) and a Berry's phase of π ($\beta = \nu\frac{1}{2}$; $\nu = \pm 1, \pm 3, \pm 5, ...$). The slight deviation from the exact theory values possibly reflects the uncertainty resulting from smearing of the SdH oscillations due to LL broadening.

2.2.4 Graphene nanoribbons: bandgaps and magnetic edge states

The absence of a bandgap in graphene is considered a major drawback when thinking of electronic applications and devices. In conventional semiconductor electronics the inherent energy gap provides the possibility to switch between conduction states with high on/off ratios and it is therefore at the heart of the functionality of almost every semiconductor electronic device. Further, a bandgap facilitates a plenty of mesoscopic devices like 2DEGs at semiconductor interfaces and additional confinement via local electrostatic gates.

Several ways to overcome the gapless nature of graphene are theoretically predicted and a number of approaches have been investigated experimentally: (*i*) breaking of the sublattice symmetry via interaction with a particular substrate (SiC) [72, 73] or (*ii*) breaking of the layer symmetry via asymmetric doping of a bilayer system [74, 75] and (*iii*) changing of the bandstructure by introducing additional boundary conditions in narrow graphene ribbons [76–79]. In close analogy to semiconducting carbon nanotubes a non-vanishing bandgap is predicted for narrow stripes of graphene (graphene nanoribbons (GNR)) with a width $w \lesssim 100$ nm. This finite-size effect results from the periodic boundary conditions for the calculation of eigen-states allowing only a discrete set of wavevectors k_q within the Brillouin zone. For all widths w giving k_q not matching with $\mathbf{K}, \mathbf{K}'$ a resulting gap is estimated to be twice the quantization induced subband splitting [47, 80, 81]:

$$\Delta E = 2\pi\hbar v_F / w \ . \tag{10}$$

This analysis predicts armchair-terminated GNR to be semiconducting only if the number of atomic A-B pairs across the ribbon width is $N = 3n - 2$ or $N = 3n$ and n is integer. For zigzag-terminated GNR this predicts no gap, as in this direction $k_q = 0$ always cuts through the K-points where the conduction and valence band merge. In these cases (zz-GNR) a flat band at $E = 0$ of states localized at the edges is calculated making additional effects of carrier-carrier interaction very important.
More elaborated *ab-initio* and local spin density approximation calculations in fact predict a non-zero bandgap of similar size for both termination directions with a $1/w$ dependence and additionally magnetic states at the zigzag edges [82–84]. The strong Coulomb interaction within the flat band of a narrow zigzag GNR results in an antiferromagnetic ground state with opposite spin polarization of the two opposed edges made up of the two different sublattices [11].

A situation more relevant for most of the current experiments is the one of straight edges with uncontrolled directions giving uncontinuous edge-termination as most experiments up to now do not allow atomical precise structuring. Calculations suggest the zigzag edge-states to be quite generic [11, 85], but show strong tendency to complete localization even upon small edge disorder which therefore might dominate the transport properties in such situations [80, 86, 87]. Hence, transport experiments on nanostructured graphene today generally show gap-like features induced by (edge- and charge-) disorder and localization via Coulomb interaction effects. Therefore, interpretation in terms of the appearance and the size of a possible bandgap remains inconclusive as it turns out very difficult to avoid these localization effects. Nevertheless, some experimental approaches to fabricate GNRs with controlled edge termination have been shown to be quite promising. The different techniques include unzipping carbon nanotubes [88], selective (anisotropic) dry-etching [89], or exfoliation of natural GNRs [90]. The latter attempt relies on the fact that cautious mechanical exfoliation might lead to preferred ripping of the graphene layers along symmetry directions of the crystal [91]. First steps in this direction done in our lab are described in chapter 6.

Further experimental features of nanometer-sized graphene devices probed by low-temperature transport are presented and discussed in chapter 5.

2.3 Electron spins in semiconductors

After the materials used in our experiments are introduced in the preceding chapters we now can look into the physics of the electron and nuclear spins in these systems. For this purpose the discussion is limited to mechanisms relevant for the experimental situations of the later chapters, namely in graphene and in bulk, n-doped GaAs at low temperatures.

The quantum mechanical degree of freedom *spin*, a quantity with no classical analog, with its inherent magnetic moment has gained a lot of interest in the field of condensed matter physics and electronics during the last decades. The spin and spin-related phenomena developed from its first observations and fundamental theoretical description into one of the widest studied subjects in today's fundamental and applied research. In GaAs, both the electrons with the spin quantum number $s = \frac{1}{2}$ and the holes with the effective spin $s = \frac{3}{2}$ provide interesting spin-related effects to be studied. The symmetry of the graphene lattice, however, results in the spin $s = \frac{1}{2}$ for both the electrons and holes. Here, we report on experiments on n-doped GaAs and graphene, and therefore the focus lies on situations with $s = \frac{1}{2}$. The spin, as it is coupled to the electron with charge e and it carries a magnetic moment of $\boldsymbol{\mu}$, can undergo a number of different interactions in a solid state environment. For the experiments in the subsequent chapters the relevant effects include Zeeman coupling to magnetic fields, exchange interaction, spin-orbit (SO) interaction, and hyperfine interaction with nuclear spins of the host material, which are therefore introduced in the following.

2.3.1 Electron spin interactions in semiconductors

Zeeman interaction

The Zeeman interaction of the electrons in solid-state systems is given by the classical coupling of its magnetic moment $\boldsymbol{\mu} = \vec{g}\mu_B\mathbf{S}$ (μ_B is the Bohr magneton) to an external magnetic field $\mathbf{B}$ given by the Hamilton operator

$$\hat{H}_Z = \vec{g}\mu_B\,\hat{\mathbf{S}} \cdot \mathbf{B}, \tag{11}$$

where $\vec{g}$ is the isotropic g-tensor of the specific material with a value close to the free-electron situation of $+2.0$ in graphene [92, 93] and with a value of -0.44 at the conduction band edge of GaAs due to a relatively large spin-orbit coupling energy[5] of $\Delta_{SO} = 0.341$ meV. The Zeeman term therefore provides two ways to access the spin in an experiment: first and most important, a magnetic field can be used to energetically separate spin states proportional to the specific $\vec{g}$ and second, a position dependent g-tensor resulting from modifications in the local environment results in a lateral variation of the Zeeman splitting enabling controlled precession of the spins by time-dependent gate voltage modulations laterally shifting the electron wavefunction [95].

Exchange interaction

Exchange interaction results from the combination of Coulomb repulsion and the antisymmetric wavefunction of fermions. It therefore provides a rather indirect coupling between the spins of the electrons. Apart from the important case of coupling to magnetic impurities in dilute magnetic semiconductors (e.g. GaMnAs) it is mostly relevant for localized electron states like at ionized impurities or in quantum dots as it scales with the wavefunction overlap of the interacting carriers. Nevertheless, for itinerant carriers there is an exchange effect resulting from the Hartree-Fock self-energy term, which is only important in the case of spin polarization where it results in a quite large effective magnetic field along the direction of the spin polarization and can lead to a considerable increase of the electron spin lifetime [96, 97].

In terms of interaction strength an extra comment on graphene is in order. The interaction parameter r$_S$ is a general measure of the relative importance of carrier-carrier interaction given by the ratio of the average Coulomb energy and the Fermi energy and reaches from $r_s < 1$ for weakly interacting systems to $r_s \gg 1$ for strong interaction. In graphene r_s is independent of the density n as both E_C and E_F are $\propto \sqrt{n}$ as a result of the linear energy dispersion of equation (4):

$$r_S = \frac{e^2}{\kappa \, \hbar v_F} \, , \tag{12}$$

---

[5] For semiconductors with s-type bands: $g = 2.0 - \delta g \, ; \, \delta g \propto \frac{\Delta_{SO}}{E_g(E_g + \Delta_{SO})}$ [94]

with the effective dielectric constant κ and the constant Fermi velocity $v_F \approx 10^6$ m/s of graphene. This contrasts conventional 2D systems with parabolic band dispersion where $\mathrm{r}_S \propto \frac{1}{\sqrt{n}}$. Further, according to equation (12) graphene has a maximal r_S value of 2.2 in vacuum (0.8 for one-side support on SiO_2) and is therefore generally considered as only weakly interacting in most experimental situations [98] also making exchange interaction unimportant in graphene.

Spin-orbit interaction

The spin-orbit interaction (SOI) is very often the most important one for the electron spin dynamics in semiconductors. It stems from the relativistic effect of an effective magnetic field $\boldsymbol{B}_i = \frac{m}{e\hbar}\, \mathbf{\Omega}(\mathbf{k})$ felt by an electron moving with momentum $\mathbf{p} = \hbar\mathbf{k}$ in the potential landscape $V(\mathbf{r})$ of surrounding charges:

$$\hat{H}_{SO} = \frac{1}{2}\, \mathbf{\Omega}(\mathbf{k}) \cdot \hat{\boldsymbol{\sigma}}, \tag{13}$$

where $\hat{\boldsymbol{\sigma}}$ are the Pauli matrices and the precession vector $\mathbf{\Omega}(\mathbf{k})$ reflects the lattice potential symmetry. SOI therefore provides a coupling of the spin to $V(\mathbf{r})$ given by the crystal lattice, phonons, defects and any symmetry-breaking, external potential (e.g. at heterostructure interfaces or electrostatic gates). In GaAs, $\mathbf{\Omega}(\mathbf{k})$ is an odd function of $\mathbf{k}$ reflecting the space inversion asymmetry of the zinc-blende structure. In general, for unstrained III - V semiconductors SOI in the bulk is usually dominated by the Dresselhaus coupling $\Omega_i = 2\gamma_D\; k_i(k_j^2 - k_k^2)$ with the Dresselhaus coefficient γ_D (in GaAs $\gamma_D \simeq 9$ eV Å^3 [99]) and the components i, j, k along the different crystal axis [100], [010], [001] given by cyclic permutation. At surfaces and heterostructure interfaces the built-in electric field can also result in a significant spin-orbit interaction, called Rashba SO-coupling. The SO-field of both terms in GaAs is depending on the propagation direction of the charge carriers.

In graphene the intrinsic SOI, induced by the intra-atomic Coulomb potential, is associated with a very small energy $\lesssim 24$ μeV due to the small atomic number Z=6 of carbon [100, 101]. However, transverse electric fields (Rashba-type SOI) and local curvature (rippled graphene) can give effective contributions on the same order of magnitude [102]. The latter effect leads to the rather large SO-splittings (≈ 0.3 meV) observed in carbon nanotubes with a diameter of a few nanometers [103] which is much smaller than the typical curvature radius $R > 30\,\mathrm{nm}$ of rippled graphene [67, 102, 104]. Even though the curvature of the ripples in overall flat graphene might average out over the device area, charge carriers will still be exposed to small locally fluctuating SO-fields. Nevertheless, SOI in graphene is expected to be among the weakest of relevant solid-state systems.

Hyperfine interaction

The hyperfine interaction (HF) constitutes the coupling of the spin ($\mathbf{S}$) and orbital ($\mathbf{L}$) angular momentum of the electrons with the nuclear spin momentum $\mathbf{I}$. As the nuclear magnetic moment is very small ($\mu_N \sim 10^{-3}\mu_B$) mostly states with s-wave symmetry having non-zero wavefunction amplitude $\Psi(\mathbf{R})$ at the nucleus site give relevant contributions. At the same time, these s-like states have a negligible angular momentum and the hyperfine interaction reads

$$\hat{H}_{HF} = \sum_n A \; v_0 \;\; |\Psi(\mathbf{R}_n)|^2 \;\; \hat{\mathbf{S}} \cdot \hat{\mathbf{I}}_n, \tag{14}$$

with the sum over all nucleus sites $\mathbf{R}_n$ within the unit cell volume v_0.[6] In GaAs the average hyperfine coupling constant A $\simeq 90$ μeV [105] and with that more than two orders of magnitude larger than in silicon. This points out the great importance of the nuclear spin environment in GaAs spin-related devices.

In natural graphene, which is comprised of the two stable isotopes ^{12}C and ^{13}C with the relative abundances of 99:1, only the latter has a non-zero nuclear moment. Therefore, the hyperfine interaction is negligible in graphene except for ^{13}C-enriched samples (e.g. CVD-grown graphene from isotope enriched hydrocarbons [106]) where the hyperfine coupling constant A is expected to be ≈ 1 μeV [12].

2.3.2 Electron spin relaxation in semiconductors

All the interactions listed above facilitate various spin relaxation mechanisms leading to different regimes of the electron spin dynamics in a semiconductor, primarily

---

[6] In chapter 4.7.6 we use the resulting probability at a given site $\mathbf{R}$: $|\phi(\mathbf{R})|^2 = v_0 \, |\Psi(\mathbf{R})|^2$

governed by the carrier density (intrinsic, non-degenerate, degenerate regime) and temperature. Time-dependent fluctuations of the effective magnetic fields can induce spin relaxation, where longitudinal fluctuations induce dephasing (T_2 process) due to the variation in precession frequency and transversal ones lead to relaxation (T_1 process)[7]. Furthermore, the spins in the semiconductor can also relax spontaneously, e.g. via SO-mediated emission of phonons, not requiring any magnetic interaction.

As spin-orbit coupling results in a mixture of the spin states in the electronic eigenstates (e.g. $\Psi_{\mathbf{k}\uparrow} = (\alpha_k(\mathbf{r})\,|\uparrow\rangle + \beta_k(\mathbf{r})\,|\downarrow\rangle)\, e^{i\mathbf{kr}}\,;\ |\beta| \ll 1)$, the spin is no longer a good quantum number for large SOI. In this situation, the propagating spins will be perturbed by the electric field of a (non-magnetic) scattering center (e.g. at the impurity site) [108]. This is called Elliot-Yafet (EY) relaxation and typically gives a spin relaxation rate [109]

$$\tau_{SO}^{-1} = A\ \tau_p^{-1}, \tag{15}$$

where τ_p^{-1} is the momentum scattering rate and the prefactor A is depending on the relative value of SO-splitting and the semiconductor bandgap [110].

Further, the anisotropic nature of the SO-coupling in materials lacking bulk inversion symmetry results in the momentum dependent precession vectors $\mathbf{\Omega}(\mathbf{k})$. This opens a relaxation channel by spin-precession around axes randomly changing with scattering into different momentum states. The resulting decay of the spin states is called D'yakonov-Perel' (DP) relaxation. Doped semiconductors are mostly in the regime of strong scattering, $\langle\omega_0\rangle\,\tau_p \ll 1$, resulting in the motional-narrowing spin flip rate[8]

$$\tau_{SO}^{-1} \propto \left\langle\omega_0^2\right\rangle \tau_p \tag{16}$$

as a consequence of a random walk of the electron spin on the Bloch sphere due to the fluctuation of the wavevector dependent precession axes given by the SO effective field $\mathbf{B}_i$ which is constant in between scattering events. Thus, the D'yakonov-Perel'

---

[7] Typically, spin decay is described using the Markov approximation where the correlation time τ_c of the fluctuations is short compared to the average precession frequency $\langle\omega_0\rangle$, e.g. $\langle\omega_0\rangle\,\tau_c \ll 1$. Though, there might also be a relevant Non-Markovian regime when spin relaxation results from hyperfine coupling to a slowly varying nuclear spin bath [107].

[8] τ_{SO} is the time required to accumulate to a phase of π by the number of random walk steps $N(t) = t/\tau_p$ each leading to a phase change of $\delta\Phi = \langle\omega_0\rangle\,\tau_p$: $\Phi(\tau_{SO}) = \delta\Phi\,\sqrt{N(\tau_{SO})} \equiv 1$.

mechanism leads to longer spin lifetimes for stronger momentum scattering, opposite to the Elliot-Yafet mechanism. This quite intuitively reflects the fact that the DP relaxation acts between momentum scattering events whereas with the EY mechanism the spin relaxation occurs at the scattering events. The DP relaxation is typically important in n-doped III-IV semiconductors for temperatures down to a few Kelvin where the charge carriers still occupy extended states. In semiconductors with small bandgaps and large SO-splitting EY-relaxation is of increased importance, e.g. in InSb [108].

For clean, intrinsic graphene the DP mechanism should be much more important than EY-relaxation ($\tau_{EY}/\tau_{DP} \approx (k_F \ell)^2 \approx 300$)[111, 112]. At very low density, and high mobility, the spin lifetime will be additionally limited by a relaxation mechanism via fluctuating, effective fields induced by lateral corrugation (ripples) or strain [112]. These local gauge fields create an additional kind of SO-relaxation fairly specific to graphene. However, the experimental results seem to contrast the expectations in that the DP relaxation only dominates in bilayer graphene, whereas in single layer graphene the EY-mechanism is fastest presumably due to short-range impurity scattering (adatoms) [113]. Therefore, the longest spin relaxation times up to now are found in bilayer graphene ($\tau_s \lesssim 3$ ns)[113, 114] and single layer graphene devices do not meet the expectations of large spin lifetimes up to now.

Another special system in terms of spin relaxation are p-doped semiconductors where the Bir-Aronov-Pikus (BAK) relaxation mechanism becomes the most efficient at low temperatures. This BAK relaxation results from electron-hole exchange interaction due to conduction-band valence-band mixing [115, 116]. In n-doped semiconductors this is always negligible in lack of a significant hole density.

In intrinsic or low-doped GaAs, where most charge carriers are localized at impurities or ionized dopants, and for spins in semiconductor quantum dots, dephasing and relaxation via hyperfine interaction is an efficient process [107]. On the one hand, the free induction decay of an ensemble of non-interacting spins due to a random Overhauser field of the nuclear moments can be echoed away as the long-lived nuclei create a quasi-static environment. On the other hand, temporal fluctuations of the Overhauser field driven by nuclear dipole-dipole interaction or by variation of the hyperfine coupling itself cannot be harnessed by the echo technique and do lead to spin relaxation which can only be damped by more elaborated field pulsing [117, 118]. Electron spin relaxation via hyperfine coupling is therefore often one major source of limited coherence in confined semiconductor systems. In bulk degenerately doped semiconductors, instead, the hyperfine interaction mediates a very weak spin-flip scattering and therefore provides a negligible relaxation channel compared to the dominant SO-relaxation mechanisms as discussed above.

In a situation where different local moments are weakly coupled, exchange interaction can relax the spins whereas hopping between the electron sites leads to motional narrowing. This is usually the situation of n-doped semiconductors right below the metal-insulator transition (MIT) or in coupled states in nanostructures, e.g. double quantum dots.

In semiconductor nanostructures like nanowires, quantum dots or quantum point contacts other spin relaxation mechanisms like spin-phonon scattering and relaxation due to g-factor inhomogeneity or due to a spatial confinement-potential can become especially important [6, 110]. As the spin valve experiments under consideration are performed in bulk GaAs at low temperatures, these effects are not discussed in more detail here. In graphene, except for the gauge field effects induced by static ripples (quenched phonons), spin-phonon scattering is supposed to be negligible due to the weak SOI, allowing μm-long spin relaxation lengths even at room-temperature currently limited by extrinsic spin scattering [111–113, 119].

2.4 Nuclear spins in semiconductors

Apart from the electron spins in the GaAs lattice there are also nuclear moments of the isotopes ^{69}Ga, ^{71}Ga, and ^{75}As present which all carry a nuclear spin $\mathrm{I} = \frac{3}{2}$. In natural graphene only 1% of the atoms in the lattice are ^{13}C having a non-zero nuclear spin ($\mathrm{I}[^{13}\mathrm{C}] = \frac{1}{2}$, $\mathrm{I}[^{12}\mathrm{C}] = 0$) and are therefore not discussed further in the remainder of this chapter. All the nuclear moments (with $\mathrm{I} \neq 0$) undergo interactions with the electronic system (as already mentioned above), the lattice and within the nuclear spin system itself.

Due to the absence of electrostatic dipole moments of the nuclei, the only possible electrostatic coupling to the electron charges is via quadrupolar moments present for I ≥ 1. Further, quadrupolar couplings are zero for cubic environments for symmetry reasons [120]. However, in a zinc-blende crystal like GaAs the quadrupolar coupling provides an important relaxation channel via phonons at high temperatures as will be discussed in chapter 2.5.

The more important nuclear spin interactions are of magnetic type. First, there is the classical dipole-dipole (DD) coupling between neighboring nuclear magnetic moments. This interaction depends on the magnitude and direction of the moments $\boldsymbol{\mu}_i = \gamma_i \hbar \, \mathbf{I}_i$ and on the vector $\mathbf{r}_{i,j}$ between the positions of the interacting dipole moments i and j, giving the according Hamiltonian for the total system

$$\hat{H}_{DD} = \sum_{i<j} \frac{\gamma_i \gamma_j \hbar^2}{r_{i,j}^3} \left(\hat{\mathbf{I}}_i \cdot \hat{\mathbf{I}}_j - 3 \frac{\left(\hat{\mathbf{I}}_i \cdot \mathbf{r}_{i,j}\right)\left(\hat{\mathbf{I}}_j \cdot \mathbf{r}_{i,j}\right)}{r_{i,j}^2} \right). \tag{17}$$

With this, one can identify an effective local dipole field $\mathbf{B}_d^i$ felt by any nuclear moment $\boldsymbol{\mu}_i$ caused by the surrounding nuclei, writing $\hat{H}_{DD} = -\sum_i \boldsymbol{\mu}_i \cdot \mathbf{B}_d^i$. This DD coupling leads to motional narrowing in liquids and gases, where $\mathbf{r}_{i,j}$ is a rapid function of time. In solids however, the DD interaction with many (potentially different) neighboring moments leads to a broad distribution of Larmor-frequencies. As $\mu_n \propto 10^{-3}\mu_B$ and $\mathrm{r}_{i,j} \propto$ Å the local dipole field in GaAs is of the order of Gauss ($\mathrm{B}_d \lesssim 0.21$ mT), if all dipolar and exchange couplings are included [105] and is therefore negligible compared to the nuclear Zeeman energy except for very small or zero external fields.

The magnetic coupling of the nuclear moments to the electron system generally consists of two major contributions. One is the coupling to the orbital angular momentum of the electron charge, called *chemical shift*, and one stems from the interaction with the magnetic field created by the spin moments of delocalized electrons, called *Knight shift*. The former, giving substantial effects for many free atoms, is evidently zero for s-state electron orbits (L=0) and usually vanishes for solid state systems due to quenching of the orbital momentum by the surrounding charges in the lattice. The *Knight shift* is a result of the hyperfine coupling to s-band electrons responsible for the drastic differences of the environment of the nuclei in a metal and in an insulator, and further mediates a second order coupling between nuclear moments via the electronic system. As we are interested in nuclear spin effects in metallic and semiconducting solid state systems we focus on the electron-spin nuclear-spin hyperfine interaction as the coupling mechanism.

2.4.1 The Fermi contact interaction

As already mentioned above, the magnetic coupling between the magnetic moments of the electron and the nuclear spin is very small but still is important in terms of the interactions of the nuclei in system of delocalized electrons - and in some cases the most important one, as it will turn out later. Further, the description with the dipole-dipole Hamiltonian like in (17) –with one **I** replaced by **S** – leads to a radial catastrophe (logarithmic divergence) for very small distances where the DD-coupling predominates and therefore requires careful analysis. To get a realistic result one has to take into account the spatial extent of the nucleus and its overlap with the volume of finite wavefunction amplitude of the electron under consideration, which therefore are mostly s-state electrons. Additionally, the large electronic potential energy close to the nuclei in principle advises a relativistic treatment of the problem. Nevertheless, a non-relativistic and quasi-classic derivation is possible by averaging the magnetic moment created by a current distribution within the nucleus radius over the orbital probability density of the electron [121, 122]. The resulting single-spin eigenvalue of the hyperfine Hamiltonian given in (14) is

$$E = -\frac{8\pi}{3} \left|\Psi(0)\right|^2 \boldsymbol{\mu}_n \cdot \boldsymbol{\mu}_e = \frac{8\pi}{3} \gamma_e \gamma_n \hbar^2 \left|\Psi(0)\right|^2 \mathbf{I} \cdot \mathbf{S}. \tag{18}$$

This interaction term was first derived by E. Fermi [123] and the factor $\left|\Psi(0)\right|^2$ makes the name *contact interaction* obvious reflecting the fact that peripheral moments give zero magnetostatic contributions as a result of angular integration.

2.4.2 Dynamic nuclear polarization and the Overhauser field

The hyperfine coupling described above mediates a nuclear relaxation process involving simultaneous electron and nuclear spin flips. Although other interactions, like orbital hyperfine coupling, might also relax the nuclei without an accompanying electron spin flip, the contact interaction usually dominates in metallic systems at cryogenic temperatures where spin-phonon relaxation is frozen out. For such a situation, A. W. Overhauser proposed a technique for creating large nuclear polarization by saturating an electron-spin resonance (ESR) transition [124]. Generally, this can create an enhancement of nuclear polarization by three orders of magnitude and is called *dynamic nuclear polarization* (DNP) as it is driven by pumping the electron spin system continuously out of equilibrium. The method of DNP has since been applied in many different ways apart from ESR: optical pumping using polarized light [108], single electron pumping using Pauli spin-blockade in quantum dots [125], spin polarized modes in quantum point contacts [126], and electrical spin injection using ferromagnetic contacts [127–129]. The effective magnetic field resulting from the dynamically polarized nuclear system is called *Overhauser field* symbolized with B_N throughout this thesis. In steady-state, it amounts to

$$\mathbf{B}_N = f b_n \frac{\langle \mathbf{S} \rangle \cdot (\mathbf{B} + \alpha \langle \mathbf{S} \rangle)}{B^2 + \xi B_d^2} \, \mathbf{B} \; , \tag{19}$$

where $b_N \simeq 5.3$ T is the Overhauser field of total nuclear polarization in GaAs [105], $\langle \mathbf{S} \rangle$ is the ensemble averaged electron spin, α is a prefactor giving the average electronic field $\mathbf{B}_e = \alpha \langle \mathbf{S} \rangle \lesssim$ mT, $\xi \approx 2.2$ is a measure of the relative relaxation strength by the local dipole field $\mathrm{B}_d \sim 0.2$ mT [105], and f is a leakage factor due to nuclear spin diffusion and the competing relaxation channels mentioned above [105].

2.5 Nuclear spin relaxation in solids

The dynamic evolution of solid state nuclear spins is determined by the coupling to the lattice and between nuclear moments. Here, the 'lattice' has to be seen as a collection of all coupling terms of the surrounding crystal possibly relaxing the nuclei. Especially at very low temperatures, where only a few degrees of freedom of the lattice are excited, a quantum mechanical description of the lattice is most appropriate and one can make use of the well established models of modern solid state physics. Further, due to the relatively tight coupling between individual nuclear spins in most solid state systems (compared to e.g. liquids and gases), dynamics within the nuclear spin system (T_2 process) have rather different time scales then the equilibration time with the lattice

(T_1 process). Thus, for $T_1 \gg T_2$ it is feasible to assign at any time a single spin temperature to the nuclei, which than evolve towards the equilibrium temperature with a single exponential decay in the natural way. Doing so, one avoids complications in the analysis of the details within the spin system, which not necessarily have an exponential time evolution, and this method is therefore very successful in a variety of different materials and situations.

2.5.1 Relaxation by phonons

Maybe the most obvious mechanism of lattice relaxation results from coupling to thermal vibrations of the crystal lattice, the phonons. For example, relaxation by this coupling can be induced by time-dependent effective magnetic fields or electric-field gradients causing nuclear spin flips. In second quantization language a situation of n phonons of a specific mode with its frequency ω in the crystal is created by a series of creation and annihilation operators giving a thermal energy of $E = (n + \frac{1}{2})\hbar\omega$. As phonons are bosonic quasi-particles, the total number present at the crystal temperature T is given by the Planck's law $\mathrm{N} = (e^{\frac{\hbar\omega}{kT}} - 1)^{-1}$ and is therefore rapidly vanishing at very low T.

As already indicated before, the only important phonon-relaxation channel is mediated by electrostatic coupling to the quadrupole moments of the nuclei. All other phonon assisted (magnetic) relaxation processes, like nuclear spin-spin and nuclear spin-orbit coupling, can be shown to be negligible [120]. In principle, there are two classes of scattering events: one involves the emission or absorption of a single phonon (direct process) and another requires two phonons either both emitted/absorbed or one absorbed and one emitted (Raman process).

For the direct process, the relaxation rate can be estimated to be

$$T_1^{-1} = C\ B_{ext}^2\ T\ , \tag{20}$$

where the linear temperature dependence is a result of a high-temperature approximation of the Planck distribution justified by the extremely small nuclear Zeeman energy $\hbar\omega_0 \ll \mathrm{k}_B T$. The quadratic dependence on the field is a direct consequence of the phonon spectral density. However, the prefactor C turns out to be negligible

small representing the fact that only a very small fraction of the phonon spectrum, where additionally the spectral density is not very large, can contribute to the direct process making it irrelevant for nuclear relaxation. The same is true for the process by the emission or absorption of two phonons with frequencies ω_1 and ω_2 restricting the contributing spectrum even further as $\omega_1 + \omega_2 = \omega_0$ has to be fulfilled.
For the Raman process the frequencies must fulfill $\omega_1 - \omega_2 = \omega_0$ and therefore the hole phonon spectrum can participate in this relaxation. The temperature dependence within the Debye model is given by

$$T_1^{-1} \propto T^{\alpha} \ , \tag{21}$$

with α=7 for very low temperatures (typically in the sub-Kelvin range) and α=2 for higher temperatures. The absolute strength of this relaxation mechanism depends on many details of the phonon spectrum and the spin-phonon coupling, but experiments on zinc-blende III-V semiconductors show it to be the relevant relaxation channel in the high temperature range with $\alpha = 2$ [130]. The low temperature range, which is experimentally not easy to resolve as magnetic relaxation takes over, seems to require the use of the detailed spectral density beyond the simple Debye model possibly leading to an even stronger T-dependence [130, 131].

2.5.2 Relaxation by fixed paramagnetic impurities

In non-metallic solids, where the electron spins occupy fixed positions in the lattice, the nuclear relaxation is a combined process of spin-flip scattering with impurities having a single unpaired spin and nuclear spin diffusion to the positions of these localized moments. In case of rapid spin diffusion, meaning that diffusion equilibrates the nuclear spins faster than the lattice can relax the nuclei, we can expect a exponential decay of the common nuclear spin temperature and

$$T_1^{-1} = \frac{4}{3}\pi N \ C \ b^{-3} \ , \tag{22}$$

with N is the number of impurities per volume, b is the radius of the diffusion barrier in the circumference of the impurity where the magnetic field of the impurity equals the local dipole field B_d, and C is given by the spectral density of the dipolar (or scalar contact hyperfine) coupling between the impurity and the nuclear spin [132]. In a situation of a diffusion bottleneck on the other hand, it is not possible to assign a common spin temperature to the nuclei and it is hard to make generally valid predictions apart from a $\sqrt{t}$ transient behavior expected for very short times t.

2.5.3 Relaxation by conduction electrons

In metallic systems the nuclear spins couple to the environment mostly via the contact hyperfine interaction with the delocalized electrons. An individual nuclear spin therefore 'sees' the effective magnetic field of many, if not all, conduction electrons occupying Bloch-states in the s-type band of the metal. The nuclear relaxation in such systems can be described in a classical scattering picture: if the hyperfine coupling induces a electron spin *flip* and an opposed nuclear spin *flop* simultaneously, the mismatch in Zeeman energies has to be compensated for by a momentum change of the electrons $\mathbf{k} \to \mathbf{k}'$. As this energy difference is quite small and the electron occupation is given by the Fermi-Dirac distribution function, only electrons occupying states very close to the thermally broadened Fermi edge can participate. The phase space for this scattering mechanism is therefore proportional to $k_B T$. The famous Korringa law describing this flip-flop relaxation in metals has been derived in several ways [120, 133] and results in

$$\frac{1}{T_1} = \frac{4\pi}{\hbar} \frac{\gamma_n^2}{\gamma_e^2} K^2 \cdot k_B T \,, \tag{23}$$

where $K = \frac{8\pi}{3} |\phi(0)|^2 \, \chi$ is the Knight shift induced by the conduction electrons and χ is the according susceptibility. As equation (23) is derived for the contact hyperfine coupling only, the given relaxation rate at a temperature T might be a lower bound due to possible, though very small, additional relaxation via dipolar and orbital electron-nucleus coupling.

Further, equation (23) assumes a free electron model and the effective rate in metals, where electron interactions are present, is usually reduced by the factor $\xi = \left[\frac{\chi_s}{\chi_0} \frac{\rho_0(E_F)}{\rho_s(E_F)} \right]^2$ with the indices s and 0 respectively indicate the renormalized and independent values of the susceptibility (χ_s, χ_0) and the density of states (ρ_s, ρ_0) averaged over the Fermi-energy E_F [134, 135]. The fact that the Korringa law is based on general grounds and the consideration of electron-electron correlation by the factor ξ makes it very successful for a wide range of materials from metals to doped semiconductors where it has been observed in numerous experiments of the past decades.

However, there is a regime where similar arguments lead to a different relaxation rate in semiconductors. This is the class of non-degenerate semiconductors with a rather low doping level keeping the Fermi-energy well below the conduction band edge. As a result, the occupation of conduction band states by charge carriers is given by the Boltzmann tail of the distribution function. Using this for the calculation of the number of available scattering states directly gives a deviation from the linear temperature dependence of the Korringa law:

$$\frac{1}{T_1} = \frac{64\pi}{9} \, \gamma_n^2 \gamma_e^2 \, n^2 |\phi(0)|^4 \, \left(\frac{m^3 k_B T}{2\pi} \right)^{\frac{1}{2}} , \tag{24}$$

with the effective mass m at the conduction band minimum (neglecting m-anisotropies and interband transitions). This $\sqrt{T}$ dependence has been observed in semiconductors having a doping level right below the metal-insulator transition [36, 136].

2.6 The non-local spin valve

In the following two subsections the working principle and basic techniques for the spin transport measurements on GaAs presented in the chapter 3 and 4 are introduced. Generally, the spin valve is a prototypical spintronics device combining the all-electrical realization of spin-injection and detection applicable in metals and semiconductors. An all-metal spin valve was first successfully realized by Johnson and Silsbee [137] using permalloy contacts on an Al slab. It turned out to be a very important model and testing tool as the device layout of a spin valve is rather simple once the challenging problem of spin-sensitive electric contacts for injection and detection is solved. The setup of lateral spin valve devices is motivated by the spin-based field-effect transistor (spin-FET) proposed by S. Datta and B. Das [138]. This transistor is based on a source-contact creating a 'spin signal' which is detected at the drain side depending on an applied electrostatic gate. This requires several spin-related features all highly non-trivial to realize in a solid state device: first one needs a technique to create a spin polarization by only electrical means, second the drain-contact has to be a spin-sensitive (voltage) probe, and third the actual transistor action relies on some electrostatic manipulation of the coherent spin transport or the spin dynamics (coherent precession) in between source and drain. The last feature was proposed to be realized by the electric field tunability of the Rashba-SO coupling in semiconductors or semiconductor heterostructures (see chapter 2.3.1) and crucially requires single-mode coherent spin propagation or fine-tuning of the Rashba- and Dresselhaus-coupling strength (e.g. $\alpha = \beta$, where α, β are the respective coupling coefficients of a 2DEG)[139]. First experimental hints for the feasibility of a spin-FET structure has been shown recently by Koo et al. [140].

2.6.1 Electronic spin injection and detection

Whereas the electrical spin injection from a metallic ferromagnet (FM) into metals, though fairly complicated in all its details, turned out to be conceptually straight forward [137], it was a long standing problem to realize an efficient way for purely electrical creation of spin polarization by carrier injection from a ferromagnetic metal into a non-magnetic semiconductor. The reason is the *conductivity mismatch* problem between FM metals and semiconductors [141], as the injection-current polarization P_i is a function of the involved resistances r_{FM}, r_{SC}, r_c of the FM, the SC, and the contact-interface, respectively (here normalized to the common cross-section area):

$$P_i = (r_c P_c + r_{FM} P_{FM})/(r_c + r_{FM} + r_{SC})\,, \tag{25}$$

with the respective steady-state current polarizations P_{FM} and P_c in the FM and across the contact interface [6, 110]. From equation (25) one expects a very weak injection efficiency from FM into a SC for highly transparent contacts ($r_c \sim 0$), where $r_{SC} \gg r_{FM}$, giving $P_i \ll 1$. After first experimental hints by S. F. Alvarado [142], a way to avoid this problem by the use of a high-resistive (or tunneling) interface was proposed by E. I. Rashba [143], making the polarization to be dominated by r_c instead of r_{FM}/r_{SC} [144]. This yields a polarization P_i proportional to the spin-selectivity P_c of the contact, which in the simplest case stems from the exchange energy and the according spin-dependent Fermi wavelengths and transmission coefficients [6]. This concept has been successfully applied to get reasonable injection efficiencies into superconductors [145], organic [146] and inorganic semiconductors via thin dielectric barriers or narrow Schottky barriers formed at the interface [127, 147–149]. An alternative route to spin

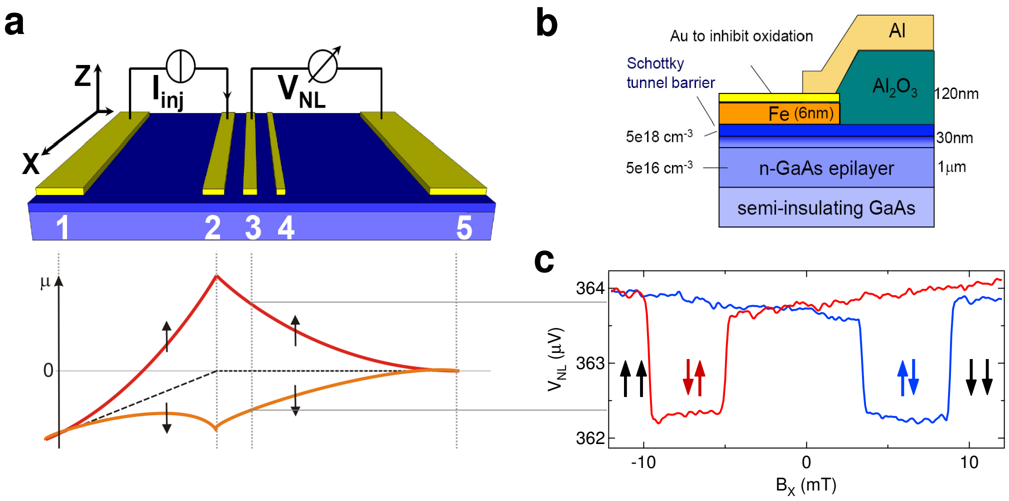

Figure 4: **Working-principle of a non-local lateral spin-valve device. a,** Spin valve device scheme for separation of charge- and spin-transport in the non-local geometry (top). Below, the spatial variation of the chemical potential for the two spin subsets is illustrated schematically for applied bias between contact 1 and 2. **b,** Structure of the GaAs wafer used for the spin valve experiments presented in this study. The highly doped surface layer ensures a thin Schottky barrier for efficient spin injection. **c,** A typical spin valve measurement trace of our devices, applying $I_{dc} = 5\,\mu$A at 40 K.

injection is possible using a magnetic semiconductor (e.q. GaMnAs) as spin source [25], especially relevant for situations where a Schottky barrier is not practicable. A completely different approach avoiding the conductivity mismatch problem has been presented recently where the spin polarization is induced by dynamic spin exchange across an Ohmic contact between a FM ($Ni_{81}Fe_{19}$) and the semiconductor (GaAs) using angular momentum transfer rather than charge-transfer across the interface [150].

A convenient method for testing the spin injection by all-electrical means is done in the non-local spin valve geometry, where the spin signal is probed outside the regions of charge currents avoiding spurious contributions from ohmic resistances, anisotropic giant (and tunneling) magneto-resistances and local Hall effects[9].

A suitable device schematic is shown in figure 4a, which is similar to the spin valve devices used for our experiments described in chapter 3 and 4. If a spin polarization in the non-magnetic semiconductor (blue) below the ferromagnetic contact 2 (yellow) is built up by a spin polarized injection-current into the semiconductor, spin diffusion will

---

[9] The local Hall effect induced by stray fields of the ferromagnets can still give contributions to the non-local spin signals for certain sample geometries [1].

spread out the polarization along magnetization gradients inside the semiconductor. This leads to a net magnetization and a difference in chemical potential of the spin channels (schematically shown Fig. 4a, bottom) away from the site of injection and in particular also outside the charge-current paths. In the open-circuit case of the non-local geometry (zero current across the detector interface), a voltage will be built up across the detector interface proportional to the remanent excess magnetization δM in the semiconductor and the detector spin-sensitivity P_c (χ is the magnetic susceptibility of the SC)[137]:

$$V_{NL} = \frac{\mu_B}{e\chi}\ P_c\ \delta M\,. \tag{26}$$

Therefore, the spin-sensitive probes 3 and 4 show an electron-spin induced voltage difference to the reference contact 5 which is placed far away so that no spin polarization will survive at this distance ($\delta M = 0$) as also indicated at the bottom of figure 4a.

The typical spin valve signal $\Delta V_{NL} = V_{NL}^{\uparrow\uparrow} - V_{NL}^{\uparrow\downarrow}$ is obtained by reversing the magnetization of one of the FM contacts (e.g. the detector) with an external magnetic field larger than its specific coercive field and therefore probing the chemical potential (or δM) of the opposite spin-direction. From Fig. 4a it is clear that this gives different voltages having opposite signs in the ideal case for detector magnetization parallel and anti-parallel to the injected spins. Generally, the absolute spin valve signal depends on the amount of spin polarization in dependence of the injection-efficiency for a given injection current, the injector-detector distance, the spin lifetime, the spin diffusion constant, and external magnetic fields as the injected excess-spins decay, diffuse and precess (if $B \neq 0$) on the way to the detector as explained in the following chapter.

The devices used in our experiments are engineered and fabricated by S. Alvarado, G. Salis, and A. Fuhrer at IBM research in Rüschlikon, Switzerland. The wafer material consists of a 1 micron thick, Si-doped GaAs epilayer grown by molecular beam epitaxy on a semi-insulating GaAs substrate. This epilayer is overgrown with a 30 nm thick, highly doped layer where the doping density is gradually increased from the bulk value of $n = 5\,\times\,10^{16}\,cm^{-3}$ within 15 nm to a maximum density of $n = 5\,\times\,10^{18}\,cm^{-3}$ (see Fig. 4b). This surface layer ensures a thin Schottky barrier, necessary for efficient spin injection, forming at the interface to the 6 nm thick Fe-electrodes which are thermally evaporated onto the clean c4x4 reconstructed GaAs surface in a ultrahigh-vacuum chamber. A final, few-nm thick Au layer protects the Fe film from oxidation. Further fabrication and design details are given in chapter 3.3.

Given by the small thickness and the elongated shape of the Fe contacts indicated in Fig. 4a, the easy-axis of magnetization is parallel to the surface along $\hat{\mathbf{x}}$ in Fig. 4a. Due to the shape anisotropy each of the electrodes 2, 3, and 4 has a slightly different coercive field (B_c^i, $i = 2, 3, 4$) as they are fabricated with different widths (see chapt. 3.3). When applying magnetic fields along $\hat{\mathbf{x}}$ in a spin valve measurement the magnetizations of the Fe contacts can be forced to align parallel to B_X for fields larger than the respective B_c^i. This leads to the characteristic square-like steps in the measured V_{NL} with distinct voltage levels for probing majority and minority spins with parallel and anti-parallel magnetization of injector and detector contact, as seen in Fig. 4c and indicated by horizontal lines between 4a and 4c. A thermoelectric offset-voltage (e.g. $V_{off} \sim 363\mu V$ in Fig. 4c) might be induced magnetically and thermally by a possible non-equilibrium region right at the FM-SC interface [151]. This is generally observed in lateral spin valves [128, 129, 137, 152] and we therefore usually subtract the constant offset for data presentation.

The polarity of the injected spins results from spin injection or spin filtering depending on the sign of the applied bias as generally majority spins (which have $\mathbf{S}$ anti-parallel to the magnetization $\mathbf{M}$ of the FM [153]) are injected from the Fe into the GaAs epilayer or extracted vice versa [128, 129, 154]. In our devices, the spin valve signal ΔV_{NL} is positive for spin injection with $I_{DC} > 0$ and negative for filtering with $I_{DC} < 0$ and increases with $|I_{DC}|$ for small injection currents indicating an expected growing spin polarization in the SC. At high bias, the spin valve signal shows a typical deviation from linear scaling, where the injection efficiency saturates (and in some devices even shrinks at higher bias [128, 155, 156]).

This is shown in Fig. 5 for our devices at T = 4 K, where the Lorentzian background, also depending on the bias current, is induced by nuclear polarization as discussed in chapter 3.4. The extracted spin signal amplitude[10] is shown for varied injection voltages V_{int} at the FM-SC interface, approximated by the measured voltage between contact

---

[10] For the details of the extraction of ΔV_{NL} in presence of the Lorentzian background see chapt. 3.4.

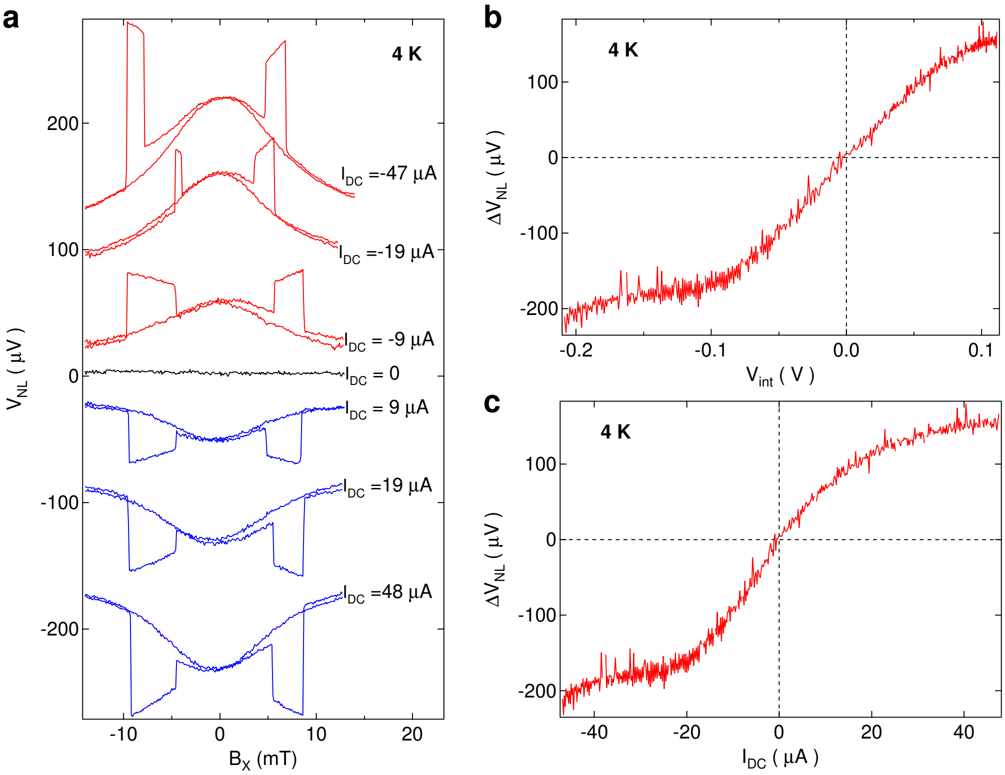

Figure 5: **Bias-dependence of the non-local spin-valve signal at 4K. a,** Exemplary spin valve traces for different injection bias currents, as indicated. The Lorentzian-shaped background results from nuclear polarization as discussed in chapter 3.4. Traces are offset for clarity. **b,** ΔV_{NL} extracted from measurements like in **a,** as a function of the injection voltage V$_{int}$ at the interface approximated by the measured voltage between contact 2 and 3, ignoring a small spin-sensitive contribution ($< 200\,\mu$V for V$_{int}$ $= 0.1\,$V) in this configuration, see Fig. 4a. **c,** Same data as in **b,** here plotted as function of injection current for comparison with **a,**.

2 and 3, in Fig. 5b and for according bias currents in Fig. 5c. The bias-dependence is subject of ongoing investigation and is found to be given by the energy-dependent tunneling properties induced by the specific properties of the interface states [157, 158] and by a transition from majority- to minority-spin injection at higher bias [159–162]. For the experiments described in chapter 4 we limit the injection bias to below saturation ($I_{DC}^{max} = \pm 20\mu A$).

2.6.2 The Hanle effect

If a magnetic field is applied perpendicular the injected spins, the evolution of the spin moments is given by the Hanle effect, as discussed below. In contrast to the spin valve feature of magnetization dependent voltages/resistances, which can also result from extrinsic effects like magnetoresitance effects or local Hall effects, the Hanle effect is the smoking gun of true spin signals [1] and further provides a very important method to study the spin-properties of a device.

Hanle line shape and the Overhauser field

As the injected spins diffuse to the detector site on arbitrary paths with accordingly different travel times, a perpendicular magnetic field randomizes the spins due to the induced precession. The steady-state spin polarization at the detector contact of the spin valve is generally described in the drift-diffusion model including spin diffusion, drift induced by the electric field **E**, and the spin precession of spin **S** induced by a perpendicular magnetic field **B**:

$$\frac{d\mathbf{S}}{dt} = D\ \nabla^2\mathbf{S} - e\mu\mathbf{E}\cdot\nabla\mathbf{S} + \frac{g\mu_B}{\hbar}\mathbf{B}\times\mathbf{S} - \frac{1}{\tau_s}\mathbf{S}\,, \tag{27}$$

where D is the diffusion constant, μ is the charge mobility, $\frac{g\mu_B}{\hbar}\mathbf{B}$ is the Larmor precession frequency ω, and τ_S is the spin relaxation time. In the non-local geometry, we can set[11] $\mathbf{E} = 0$. For the actual spin polarization at the detector the spin diffusion can be accounted for by integration over a Gaussian distribution of travel times of the

---

[11] With this we ignore effects due to lateral current spreading requiring an at least two-dimensional drift-diffusion model [163]

spins propagating from the injector (y=0) to the detector. The spin along the specific direction of spin injection ($\hat{\mathbf{x}}$) at the detector site (position y) is given by [128]

$$S_x(y,B) = S_0 \int_0^\infty \frac{1}{\sqrt{4\pi D t}} e^{-\left(\frac{t}{\tau_s}+\frac{y^2}{4Dt}\right)} \cos\left(\omega t\right)\ dt. \tag{28}$$

The result is a damped oscillation as a function of both the injector-detector distance y and the magnetic field B. For small fields ($\omega\,\tau_S \ll 1$), the detectable spin polarization is [108, 110, 164]:

$$S_x(y,B) = S_0\ e^{-\frac{y}{L_s}} \cos\left(\frac{y}{L_0}\right), \tag{29}$$

with the magnetic field dependent spin injection length $L_s = \left[\sqrt{\frac{1+(\omega\tau_s)^2}{D\tau_s}} \cos\left(\frac{\arctan(\omega\tau_s)}{2}\right)\right]^{-1}$ and the field dependent oscillation length $L_0 = \left[\sqrt{\frac{1+(\omega\tau_s)^2}{D\tau_s}} \sin\left(\frac{\arctan(\omega\tau_s)}{2}\right)\right]^{-1}$. The Hanle line shape therefore contains valuable information about the spin properties of the device like the spin lifetime τ_s and the spin diffusion constant D.

An example is given in Fig. 6 for our spin valve device on the GaAs epilayer with a doping density of $n = 5 \times 10^{16}$ cm^{-3} at 4 K. The zero-field peak corresponds to the maximum spin polarization in absence of externally induced spin precession. When the perpendicular field is increased the spins start to precess. As the diffusion paths lead to random spin phases, precession does not simply lead to a continuous oscillation of the average spin component parallel to the detector magnetization but strongly suppresses the spin signal. The spin transport parameters $\tau, D, y,$ and ω determine the number of observable oscillation periods and here only allow one sign change of $V_{NL} - V_0$ before the spin polarization is lost ($V_{NL} = V_0$, where V_0 is a subtracted, parabolic background voltage [128, 129]). Fitting equation (29) to the data in Fig. 6 gives an electron spin lifetime $\tau = 4.4 \pm 0.4$ ns and a spin diffusion constant D $= 0.0074 \pm 0.0008$ m^2/s at T $= 4$ K in good agreement with previous experiments [128, 129].

However, as the electron spins in materials having non-zero nuclear moments are exposed to the Overhauser field for non-zero nuclear polarization (see chapter 2.3.1), which is aligned parallel or anti-parallel to the external field as given by equation (19), the actual Hanle line shape can be distorted. Depending on the relative orientation (parallel/ anti-parallel) of the external and the Overhauser field, the Hanle line shape will therefore be narrowed or broadened, making the extraction of the spin lifetime and

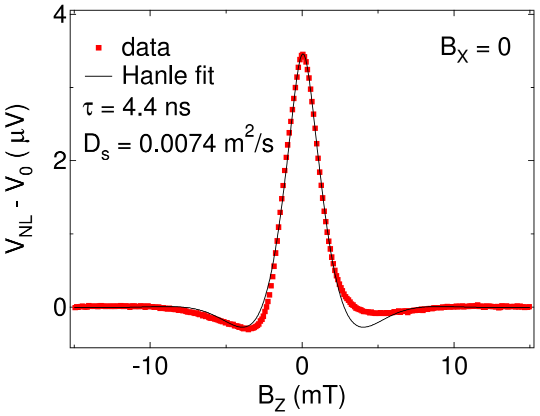

Figure 6: **Hanle line shape of the GaAs epilayer at 4K.** Standard Hanle measurement data (red) with scanning B_Z at B_X=0 and parallel magnetization of the injector and detector contact. V_0 is a subtracted, parabolic background voltage generally found in lateral spin valve geometries. The injection current is set to I_{DC}= 2.0 μA and I_{AC}= 1.7 μA. The fitted curve (black) using equation (29) gives the electron spin lifetime τ = 4.4 ± 0.4 ns and the spin diffusion constant $D_s = 0.0074 \pm 0.0008$ m^2/s .

the diffusion constant difficult if the nuclear spin system is polarized [165, 166]. The slight asymmetry of the line shape in Fig. 6, indicating a larger effective field on the positive-B_Z side, might also be interpreted in terms of a non-zero Overhauser field lagging behind its steady-state situation at every B_Z due to field ramping (0.2 mT/s) fast compared to the nuclear equilibration time, see chapter 3.5.3. The further appearance of satellite peaks and a detailed discussion of experiments on the effect of the nuclear spin polarization on the Hanle-type precession are presented in chapter 3.5.

3 The Nuclear Spin Environment in Lateral GaAs Spin Valves

3.1 Introduction

In this chapter we present experiments on the influence of the nuclear spin system on the spin signals detected in the spin valve ($\mathbf{B} \mid\mid \hat{\mathbf{x}}$) and the Hanle geometry. In the first place, this is of general interest as the interplay of the electron and nuclear spin systems in GaAs and GaAs nanostructures leads to many interesting effects, including dynamic nuclear polarization (DNP) [167, 168], intricate mutual feedback [169–171], electron spin decoherence [172], and further allows coherent manipulation of the nuclear system [173]. Second, the experimental signatures of nuclear polarization in the spin valve devices allow the study of the nuclear dynamics under various conditions and lead to the observation of the breakdown of the Korringa law of nuclear spin relaxation in these devices, which is discussed in chapter 4.

3.2 Spin valve measurements as a probe of the nuclear spin environment

We use the lateral spin valve device geometry, well-established for the study of electron spin transport [137, 152], as a model system to investigate the GaAs nuclear spin environment. A spin valve offers an efficient way to inject, manipulate and detect electron spins in GaAs [128, 129, 160], as seen in the introductory chapter 2.6.1. Electron spin polarization can be transferred by a DNP process [105, 127, 174, 175] to the nuclear system, mediated by the hyperfine contact interaction via spin flip-flop processes. The spin valve thus allows us to manipulate and investigate the native nuclear spin environment by all-electrical means, rather than using optics [108], making easily accessible the low-temperature regime $T \ll 1\,K$ which was previously not explored. In a situation of non-zero nuclear spin polarization, the electron spins are exposed to an effective Overhauser field B_N [124]. As the nuclei instantaneously follow the direction of an external magnetic field, B_N will induce electron spin precession for field vectors not pointing parallel to $\hat{\mathbf{x}}$ (the direction of spin injection). This results in clear features in spin transport measurements, including a depolarization peak [128, 129, 165] and satellite peaks in the Hanle geometry when the applied magnetic field cancels the internal Overhauser field B_N [129]. The depolarization peak saturates already for relatively small nuclear polarization, whereas the Hanle satellites can easily serve as a sensitive probe of B_N, in particular for large polarizations and down to the lowest temperatures.

3.3 Device structure and the spin valve measurement setup

The basic principles and the main features of the spin valve device used in this study are introduced in chapter 2.6.1. A schematic layout of the device is shown as inset in Fig. 7b. Apart from the wafer processing explained in the previous chapter, the Fe electrodes are structured by lithography and ion milling into defined geometries with a common length of 60 μm, widths of 6, 2 and 1 μm, and edge-to-edge distances of 3 and 4.5 μm for the three contacts in the center, respectively.

For the measurement we drive currents from the injector 2 to the 100 μm distant contact 1 and measure the non-local voltage V_{NL} between contacts 3 and 5 outside the charge current path (see inset Fig. 7b). Apart from a different coercive field, all the results can similarly obtained using contact 4 as detector contact where the size of the spin signals is reduced due to the increased ratio of the injector-detector distance to the spin diffusion length ℓ_D of several microns [129]. V_{NL} is detected via a lock-in technique using a small ac-modulation on top of a dc-injection current. The devices are measured in a dilution refrigerator equipped with a home-built 3-axis vector magnet consisting of a solenoid magnet with the field primarily along $\hat{\mathbf{y}}$ and two Helmholtz pairs creating fields mainly along $\hat{\mathbf{x}}$ and $\hat{\mathbf{z}}$, respectively. After determining the magnetization direction of the iron bars as described in chapter 3.4.3 the parallel field B_X is applied very precisely along the magnetization of the Fe bars using the field of both split-coils simultaneously.

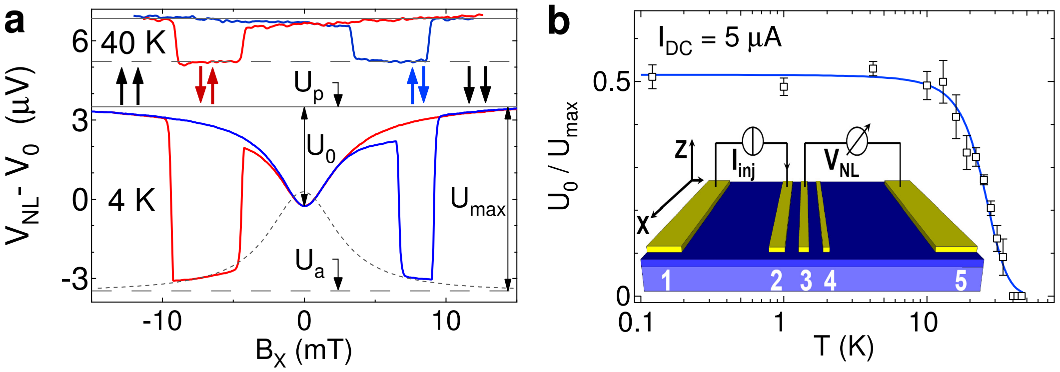

Figure 7: **Emergence of the nuclear depolarization peak at low temperatures.** **a,** Spin valve measurements as a function of applied field B_X for two different temperatures. At 40 K (upper traces offset by 6 μV for clarity) the characteristic valve switches are observed. At lower temperatures (4 K) an additional peak/dip centered around $B_X = 0$ emerges. The absolute spin signal $U_{max} = U_p - U_a$ grows for lower temperatures due to an increased electron spin lifetime. **b,** Relative depolarization peak height U_0/U_{max} from Lorentzian fits for temperatures between 40 K and base temperature. The saturation for $T \leq 10\,K$ at a value of half the absolute spin signal indicates zero spin polarization for $B_X = 0$.

3.4 The nuclear depolarization signature

Standard spin valve measurements are shown in Fig. 7a for two different temperatures. Clearly distinguishable voltage levels for parallel (U_p) and anti-parallel (U_a) alignment of injector and detector magnetization are apparent. Further, the non-local spin signal appears suppressed around $B_X \sim 0$ at low temperature [128], as the electron spins start to precess and depolarize due to $B_N \neq 0$ [129]. This in principle requires a non-zero angle between the electron spin polarization and B_N possibly due to stray fields or small perpendicular components of the external field. When B_N is strong enough to completely wash out the polarization of electron spins on their diffusive path to the detector the depolarization peak height U_0 reaches half the maximal spin signal[12] $U_{max} = U_p - U_a$ and further is not sensitive to larger B_N.

---

[12] U_{max} is equivalent to ΔV_{NL} introduced in chapter 2.6.1 and renamed here to distinguish between measured voltages V_{NL} and extracted fit parameters U_{max} and U_0.

3.4.1 The depolarization signature at low temperatures

As stated above, the depolarization signature is a result of electron spin precession in the additional field of polarized nuclei. This naturally leads to a growing depolarization amplitude U_0/U_{max} with increasing injection current and with decreasing temperature as the DNP process becomes more and more efficient (Fig. 7b). The relative dip height saturates for $T \leq 10$ K and $I_{DC} = 5\mu$A as the Overhauser field suffices to completely suppress the electron spin polarization at the detector site. This indicates that the depolarization signature becomes insensitive for larger B_N above ∼10 mT [13], equivalent to about 0.2% of the GaAs nuclei beeing polarized. As a result, the depolarization dip cannot easily serve as a sensitive detector for large nuclear spin polarizations and a different technique has to be used in this regime. Further, the width of the depolarization signature is influenced by nuclear spin inhomogeneities leading to a variation of the electron spin precession and with that generally increasing the width.

Just like the Overhauser field, any external magnetic field not parallel to the electron spins will of course also induce precession and with that a suppression of detected spin signals for low B_X. The depolarization signature therefore has the general form of a Lorentzian dip (or peak) with its half-width ΔB given by the sum of all field components ($B_{ext}^{\perp}$ and $B_N^{\perp}$) perpendicular to the electron spins [129]:

$$\Delta B = \sqrt{(B_Z + B_N^z)^2 + (B_Y + B_N^y)^2}\,. \tag{30}$$

This behavior is observed in Fig. 8a where the depolarization signature is measured for various perpendicular fields B_Z at 4K. As shown in Fig. 8b, for $B_Z > 1$ mT the width ΔB is proportional to B_Z as expected from equation (30). At low B_Z the width deviates from linear dependence on B_Z remaining at a non-zero value together with a sharp decrease of the peak amplitude (see Fig. 8c). The low-field saturation first of all indicates perpendicular field components other than B_Z to be present, including the one from B_N, together giving a field of $B_0^{\perp} = 1.0$ mT. However, in this picture the low-field behavior of the height U_0 is expected to follow the typical Hanle line shape

---

[13] This saturation value is experimentally determined by comparison with Hanle measurements described further down.

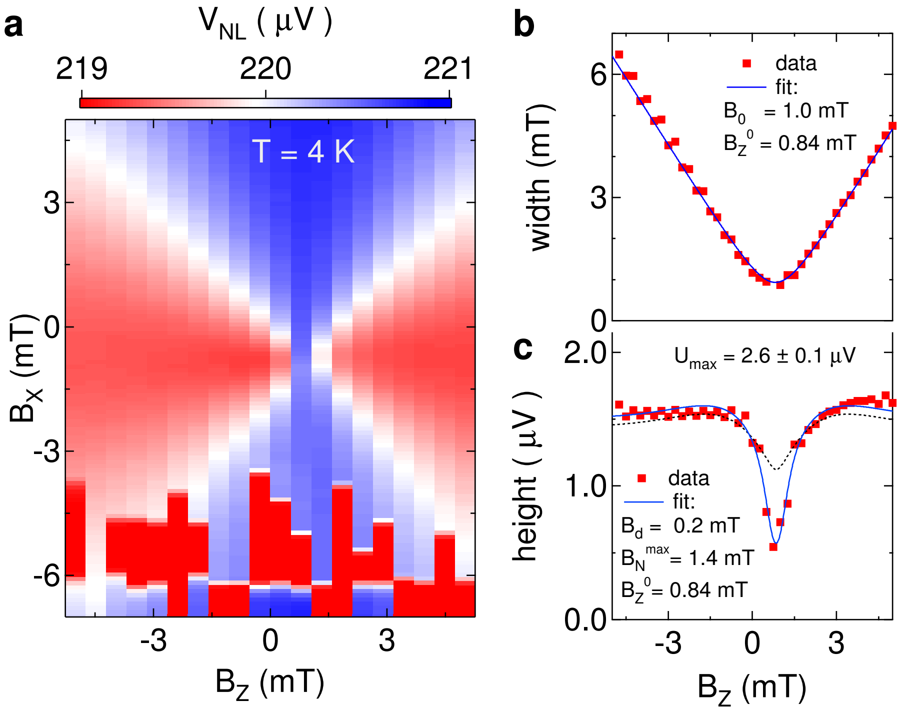

Figure 8: **Dependence of the nuclear depolarization peak on transverse magnetic fields.** **a,** Spin valve measurements as a function of additional field B_Z ($I_{AC} = 1.5\ \mu A$, $I_{DC} = 0$). The apparent offset in B_X results from slow nuclear dynamics compared to the ramp speed during measurements (0.25 mT/s). **b,** and **c,** Results from Lorentzian fits (red) to the depolarization peak in **a** showing linear dependence of the width for $B_Z > 1$ mT and a saturation at low fields together with a dip in the peak height. Solid curves in **b** and **c** are fits to equation (30) for the width and equation (31) for the height, respectively (keeping τ=4.4 ns and D_s=0.0074 m^2/s fixed, see Fig. 6). Using only static field components in equation (31) gives weak matching with our results (black dotted curve). We get a much better fit (blue curve) when a low-field depolarization of the nuclei is included (see text). Both fits (for the height and the width) consistently give a repeatable field offset B_Z^0= 0.82 mT which might be a result of local stray fields, small misalignment of the sample plane and field axis, trapped flux in the magnet, or long *RC* transients of the solenoid magnet.

H($\mathbf{B}$) from equation (29) [129]:

$$U_0 = \frac{U_{max}}{2} \left[1 - \frac{H(\mathbf{B})}{H(0)} \right] . \tag{31}$$

Fitting this form to the data in Fig. 8c with fixed parameters τ and D from Fig. 6 and static perpendicular components of $B_N = 1.4\,\mathrm{mT}$ and $B_Y = 0.2\,\mathrm{mT}$ as free parameters (black dotted curve) gives only weak agreement with our results indicating additional low-field effects to appear for B_Z very close to $B_Z^0 = 0.82$ mT where the depolarization signature is minimal. The sharp dip in U_0 can rather be understood as a depolarization within the nuclear spin system at low fields induced by the fluctuating local dipole-dipole field (B_d ~0.2 mT [105]) leading to a reduced Hanle-type dephasing of the electron spins as a result of the lowered Overhauser field [129]

$$B_N = B_N^{max} \frac{B_{ext}^2}{B_{ext}^2 + B_d^2} . \tag{32}$$

Using this field-dependent nuclear spin contribution in equation (31) gives very good agreement with the observed dip in U_0 (blue curve in Fig. 8c) with reasonable fit parameters $B_N^{max} = 1.4 \pm 0.2\,\mathrm{mT}$ and $B_d = 0.2 \pm 0.1\,\mathrm{mT}$. The rather low value of B_N^{max} is expected as no net injection current is applied ($I_{AC} = 1.5\ \mu$A, $I_{DC} = 0$).
Starting from B_Z^0 the electron spin precession accordingly is induced by static components (e.g. B_Y), followed by an increasing influence of the Overhauser field when the nuclear spins get stabilized against the dipole-dipole interaction with growing external field, and finally is dominated by the perpendicular applied field B_Z.

3.4.2 Nuclear spin dynamics detected with the depolarization signature

DNP driven reversal of the Overhauser field

The origin of the depolarization signature can be further demonstrated to be the Overhauser field of polarized nuclei by an experiment described in the following. After polarizing the nuclei at large in-plane fields B_X^{init} with a constant injection current $I_{AC,DC}^{init}$ until the saturation field B_N^{sat} given by equation (19) is reached, the orientation of the Overhauser field which instantaneously follows the external field is reversed by sweeping B_X through zero to a field B_X^{set} while keeping $|B_N^{sat}|$ essentially unchanged.

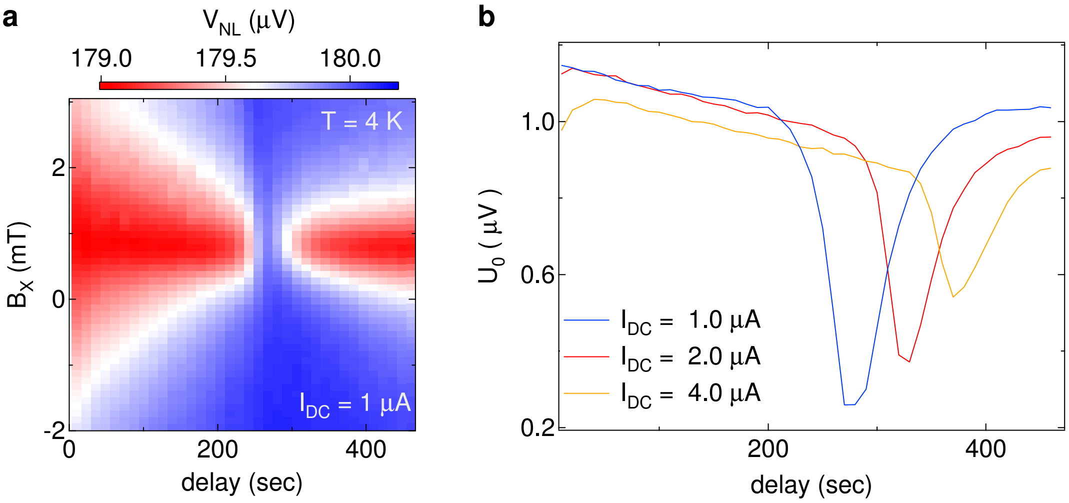

Figure 9: **Dynamics of the DNP process in the spin-valve device. a,** Spin valve measurements for increased delay times for which the DNP is reversing the nuclear spin polarization (see text). **b,** Results from Lorentzian fits to the depolarization peak showing the typical timescale (270 - 400 s) of the DNP mechanism for three different injection currents I_{DC}.

This field B_X^{set} is kept below the coercive field of both the injector and detector contact and thus the injected spin direction remains constant throughout the experiment. Driving a constant injection current I_{DC}^{set} for different delay times at this configuration first depolarizes the nuclei as they are now oriented opposite to the injected electron spins, and finally re-polarizes the nuclei to the original situation of equation (19) as probed by a fast spin valve measurement.

Such an experiment is shown in Fig. 9a using $I_{DC}^{init} = 1.2$ μA, $I_{AC}^{init} = 1.0$ μA, $B_X^{init} =$ -45 mT, $B_X^{set} = +3$ mT, and $I_{DC}^{set} = 1.0$ μA. The extracted depolarization amplitude U_0 for various delay times is shown in Fig. 9b (blue) in comparison with repeated experiments using two- and four-times the injection current of $I_{DC}^{init,set} = 2.0$ μA (red) and $I_{DC}^{init,set} = 4.0$ μA (orange). The timescale for re-polarization of several minutes and its increase with growing injection current is a strong indication for dynamically polarized nuclear spins being the origin of this behavior. The less pronounced signature of the DNP-driven nuclear polarization reversal for higher currents most likely results from an increased nuclear spin inhomogeneity for larger currents as it goes along with increased widths of the depolarization dip (not shown).

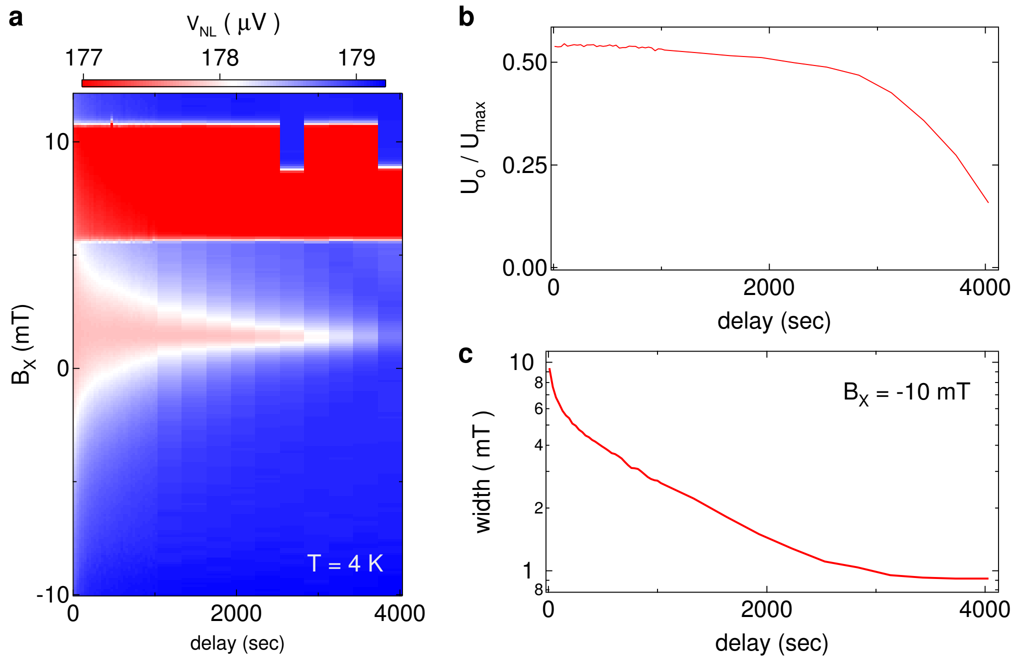

Figure 10: **Decay of the depolarization peak in an unpolarized environment. a,** Spin valve measurements for increased delay times for which the DNP is shut off ($I_{AC,DC} = 0$). **b** and **c,** Results from Lorentzian fits to the depolarization peak showing very long decay times of the nuclear polarization at 4K. Neither the amplitude U_0 nor the width is suitable to extract the T_1 relaxation time (see text).

Free decay of the Overhauser field

Similarly to the nuclear-spin reversal experiment above, one can probe the timescale of the nuclear polarization decay in an unpolarized environment. To do so, one shuts off DNP ($I^{set}_{AC,DC} = 0$) during delay so that the nuclear spins tent towards thermal equilibrium via spin-lattice relaxation. This is shown in Fig. 10a with $I^{init}_{DC} = 20\ \mu$A, $B^{init}_X = $ -20 mT, and $B^{set}_X = $ -10 mT at T = 4 K. The reduced B^{set}_X compared to B^{init}_X is used to enable faster probe scans with $I_{DC} = 0$ avoiding any further DNP and has been checked to not affect the decay dynamics observed with this method.

The extracted height and width of the depolarization signature given in Fig. 10b and c, respectively, indicate a delay time above 1 hour required for the nuclear depolarization peak to disappear. This extremely long timescale of the depolarization signature can only be understood as being induced by nuclear polarization. At the same time, both parameters (U_0 and ΔB) are not suitable to directly extract nuclear T_1 times. This is true for U_0 as it already saturates for relatively small B_N (see Fig. 7b) and the non-linear scaling with smaller B_N according to the underlying Hanle line-shape given

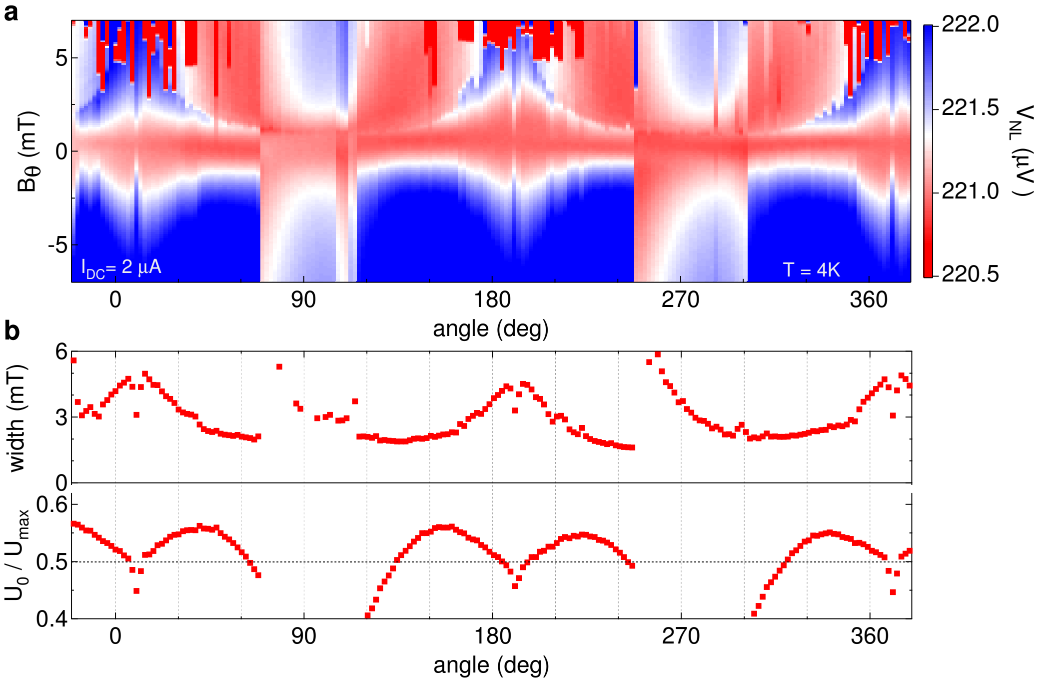

Figure 11: **Signatures of the nuclear depolarization peak in dependence of in-plane field orientation.** **a,** Spin valve measurements for a full rotation of the in-plane angle with a clear two-fold symmetry. **b,** Results from Lorentzian fits to the depolarization peak showing sharp dips in both the height and width whenever the external field is aligned to the magnetization direction of the Fe-contacts (10°, 190°, 370°).

by eq. (31). Similarly, the width ΔB is not a good measure of the actual size of the Overhauser field as it strongly depends on the homogeneity of the nuclear polarization and is additionally induced by other precession fields (e.g. $B_{ext}^{\perp}$) as discussed earlier.

3.4.3 The depolarization signature as a sensitive alignment tool

An unexpected feature of the nuclear depolarization signature is its strong sensitivity to small angles between the direction of spin injection and the applied field. When the external field is swept not parallel to the Fe-magnetization ($\hat{\mathbf{x}}$) as in the previous sections but with a certain angle $\theta = \arctan(\sqrt{B_Y^2 + B_Z^2}/B_X)$ the non-local voltage deviates from a simple Lorentzian peak and is described by the general from

$$V_{NL} = \frac{U_{max}}{2} \left[\cos^2(\theta) + \sin^2(\theta) \cdot \tilde{H}(\mathbf{B}) \right] , \tag{33}$$

where $\tilde{H}(\mathbf{B}) = H(\mathbf{B}) / H(0)$ is the normalized Hanle line shape of equation (31). Thus, with increasing θ the Hanle-line contribution (second term on the right) grows accordingly making the amplitude and shape of the measured V_{NL} curves very sensitive to the size of static perpendicular components and in particular B_N. This is consistent with our observation that a repeatable angle dependence of the depolarization peak is only seen when the nuclear spin system is kept in steady-state during the measurement indicating a intricate feedback between the angle and the internal field B_N experienced by the electrons.

In Fig. 11a 'spin valve' traces (sweeping an in-plane field) are shown spanning more then a full in-plane rotation -20° $\longrightarrow$ 380° of the scanning field direction. We observe a clear two-fold symmetry given by the magnetization direction of the ferromagnets (10° and 190°). Motivated by the Lorentzian peak for $\theta \sim 0$ we fit the same function for all angles fitting the data surprisingly well for not too large θ with results given in Fig. 11b. Interestingly, apart from an apparent growing width and a slight decrease in height when approaching the symmetry directions there are cusp-like dips in both the height and the width for precise field alignment.

This effect is, at least to some extent, described by equation (33) where the additional Hanle dephasing term ($\propto sin^2$) disappears for precise alignment. Further, this is consistent with the fact that we only find $U_0 > U_{max}/2$, a distinct feature resulting from the Hanle line shape in equation (31), for angles between applied field and injected spins exceeding a few degrees.

As mentioned above, for this observation thorough initialization of the nuclear spin system and slow rotation of the field is required. This suggest a dependence of the nuclear spin polarization and its lateral variation on the field angle, an effect not further investigated so far. The cusp signature, though not completely understood yet, is therefore a very useful tool to align the direction of applied magnetic fields to the magnetization direction of the injection and detection contact with a precision better than 1°.

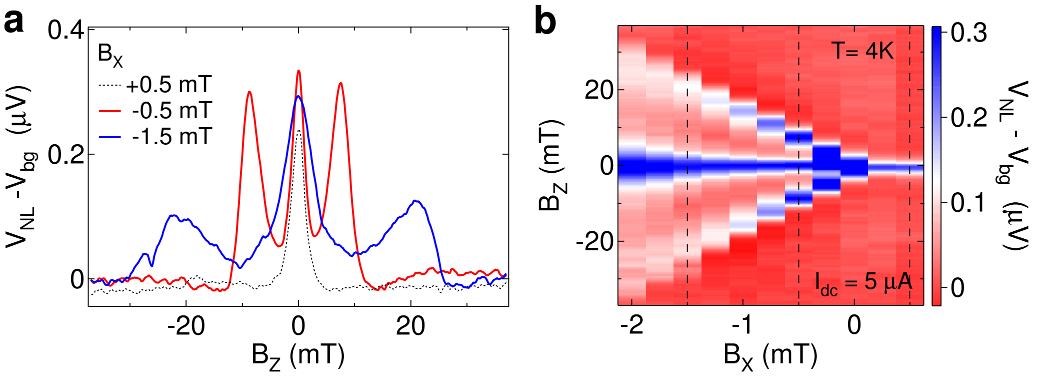

Figure 12: **Signatures of nuclear spin polarization in Hanle measurements. a** and **b,** Hanle measurements at 4 K. Displayed is V_{NL} (in **b** as color scale) versus B_Z applied perpendicular to the sample plane for various B_X. The same parabolic background is subtracted for all B_Z sweeps (0.34 mT/s). Dashed lines correspond to cuts shown in **a**. We use the satellite peaks seen for $B_X < 0$ as a measure of B_N, see text.

3.5 The signature of nuclear polarization in Hanle measurements

3.5.1 Hanle satellite peaks

As shown above, the depolarization dip cannot easily serve as a sensitive detector for large nuclear spin polarizations. To overcome this limitation, we now turn to Hanle measurements [137, 152], where an additional external field B_Z is scanned perpendicular to the sample plane, see Fig. 12a and b. The injected electron spins precess, diffuse and dephase in the perpendicular field B_Z. Around $B_Z \sim 0$, the spins do not precess much and reach the detector mostly unchanged, giving a peak in the spin signal (Hanle line-shape). For the following, both injector and detector were initialized along the positive x-direction and are kept parallel throughout. For $B_X < 0$, two satellite peaks appear (Hanle satellites) [129] as seen in Fig. 12a and b, displaying a recovery of the spin signal and hence a suppression of spin precession and dephasing [176, 177]. The satellite peaks thus indicate that B_Z is effectively canceled by the z-component of B_N. The reduced amplitude and increased width of the satellites when compared to the central Hanle peak indicate an inhomogeneous nuclear field as a result of lateral variation of the polarization of the diffusing electron spins which are the source of the DNP. The signatures and additional effects of inhomogeneity are further discussed in chapter 4.8 and 4.8.

3.5.2 High-field approximation of the Overhauser field

Theory estimates the Overhauser field $\mathbf{B}_N$ in steady-state and for large $B_{ext} = |\mathbf{B}_{ext}| \gg B_L$, where $B_L \sim 1\,\mathrm{mT}$ is the rms field seen by a nuclear spin, as [105, 127]:

$$\mathbf{B}_N = b_N^0 \frac{B_X S_X}{B_{ext}^2} \mathbf{B}_{ext}, \tag{34}$$

where b_N^0 is the maximum nuclear field obtainable with DNP and $|S_X| \leq 1$ is the resident electron spin polarization along the x-direction. Following eq. (34) and also eq. (19), $\mathbf{B}_N$ is either parallel or antiparallel to $\mathbf{B}_{ext}$ and in particular, $\mathbf{B}_N$ points opposite $\mathbf{B}_{ext}$ for $B_X < 0$ and $S > 0$. Thus, the external field *vector* $\mathbf{B}_{ext}$ can cancel the Overhauser *vector* $\mathbf{B}_N$. This leads to a recovery of the electron spin polarization and appearance of the satellite peaks, which can therefore be used to measure $\mathbf{B}_N$ [108, 129, 177]. For $B_Z \gg B_X, B_Y$, we have $B_N \sim B_Z$ on the satellite peak. Nuclear fields achieved here are $\sim 50\,\mathrm{mT}$, about one percent of the $\sim 5\,\mathrm{T}$ for fully polarized nuclei in GaAs.

3.5.3 Dynamic effects of long nuclear equilibration times

The steady-state situation assumed in eq. (34) is not typically reached in our measurements, since the ramp rates employed are fast compared to the time scales of the nuclear spins. Performing a time average $\langle\cdot\rangle_t$ of the magnitude of eq. (34) gives [129]

$$\langle B_N \rangle_t \approx b_N^0 B_X S_X \left\langle \frac{1}{B_{ext}} \right\rangle_t . \tag{35}$$

Note that the largest contributions to $\langle\cdot\rangle_t$ arise around $B_Z \sim 0$ and therefore $B_{ext} \sim B_X$, where the equilibrium $B_N = b_N^0 S_X$ is maximal. The resulting average nuclear field B_N and therefore satellite peak splitting is linear in B_X, as seen in Fig. 12b [129]. Further, significant broadening of all three peaks is visible for increasingly negative B_X. For the measurements of the nuclear spin relaxation in chapter 4, we fix $B_X = -1.5\,\mathrm{mT}$ as a compromise between peak splitting and broadening.

4 Breakdown of the Korringa Law of Nuclear Spin Relaxation in Metallic GaAs

Dominikus Kölbl, Dominik M. Zumbühl
Department of Physics, University of Basel, Klingelbergstrasse 82, CH-4056 Basel, Switzerland

Andreas Fuhrer, Gian Salis, Santos F. Alvarado
IBM Research, Zürich Research Laboratory, Säumerstrasse 4, 8803 Rüschlikon, Switzerland

Abstract

We present nuclear spin relaxation measurements in GaAs epilayers using a new pump-probe technique in all-electrical, lateral spin-valve devices. The measured T_1 times agree very well with NMR data available for $T > 1\,\mathrm{K}$. However, the nuclear spin relaxation rate clearly deviates from the well-established Korringa law expected in metallic samples and follows a sub-linear temperature dependence $T_1^{-1} \propto T^{0.6}$ for $0.1\ \mathrm{K} \leq T \leq 10\ \mathrm{K}$. Further, we investigate nuclear spin inhomogeneities.

This chapter is published in *Phys. Rev. Lett.* **109**, 086601 (2012).

4.1 Introduction

The coupling between the electronic and nuclear spin systems in condensed matter is of fundamental importance, leading to many interesting effects including dynamic nuclear polarization (DNP) [105, 108, 174], Overhauser fields [124] as well as Knight shifts [178]. The Overhauser fields can induce electron spin decoherence but can also be exploited for coherent electron spin manipulation – relevant in spintronics [2, 138] and quantum computation [5, 7]. The nuclear spin system, on the other hand, is likewise affected by the electrons, e.g. by the hyperfine field and nuclear-electron spin flip-flops, contributing to nuclear spin polarization and relaxation.

In metallic systems, the small nuclear Zeeman splitting restricts the electrons participating in flip-flops to the thermally broadened Fermi-edge, resulting in a nuclear spin relaxation (NSR) rate T_1^{-1} proportional to the electronic temperature T – the Korringa law of nuclear spin relaxation [133]. This NSR law holds for temperatures T smaller than the electronic Fermi temperature but exceeding the nuclear Zeeman splitting and further assumes a free electron model and a dominant Fermi-contact interaction. The Korringa law has been confirmed over many years in numerous experiments in a wide range of metals [120, 121, 135] as well as metallically doped semiconductors [136, 179, 180] and is well established as the preeminent law of NSR in metallic systems at low temperatures. As an application, the Korringa law provides the crucial link for cooling the electronic degree of freedom in nuclear demagnetization refrigeration [181, 182]. Deviations from the Korringa law have been reported in samples at the metal-insulator transition (MIT) showing non-metallic conductivity [36] or in various exotic materials.

4.2 Previous experiments and our findings

In this Letter, we report the breakdown of the Korringa law in n-doped GaAs epilayers displaying metallic conductivity. NSR is measured with a novel pump-probe technique in lateral, all-electrical spin-valve devices [137, 152] on GaAs [128, 129, 160], making easily accessible the low temperature regime $T \ll 1\,\mathrm{K}$ which was not previously explored. This technique is in principle applicable to any spin-valve device. The

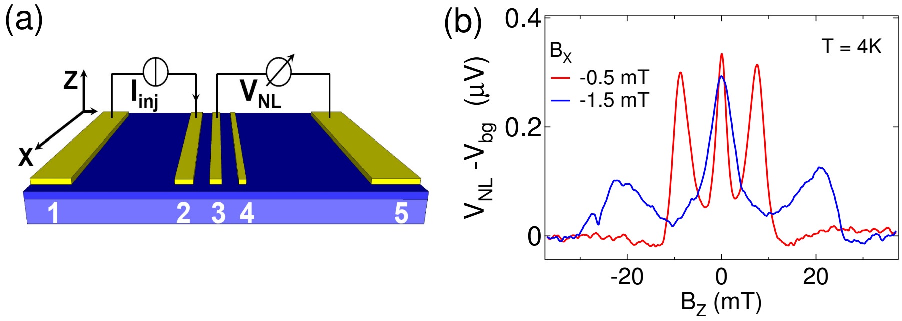

Figure 13: (a) Illustration of spin-valve device and measurement setup. (b) Hanle measurements at 4 K with satellite peaks indicating the nuclear Overhauser field B_N. The non-local voltage V_{NL} is shown as a function of perpendicular field B_Z (ramp rate 0.34 mT/s) for B_X as labeled. A parabolic background $V_{bg}(B_Z)$ has been subtracted.

measured T_1 times agree well with NMR experiments available for high temperatures $T > 1\,\mathrm{K}$ [180, 183]. The temperature dependence of the NSR rate follows a power law $T_1^{-1} \propto T^{0.6\pm0.04}$ over two orders of magnitude in temperature $0.1\,\mathrm{K} \leq T \leq 10\,\mathrm{K}$, deviating substantially from the Korringa law $T_1^{-1} \propto T$ for the present doping a factor of ~ 2.5 above the GaAs MIT well on the metallic side. The observed NSR power law $\propto T^{0.6}$ is qualitatively consistent with the combined effects of disorder and electron-electron interactions [37, 184] within a hyperfine-mediated NSR mechanism applicable here, though an appropriate theory is not currently available. At low T, relatively strong coupling and correspondingly fast NSR rates are found, potentially enhancing electron cooling in nuclear refrigeration schemes. Finally, we investigate effects of nuclear spin inhomogeneities.

4.3 Spin valve devices and the measurement setup

The spin-valves, shown in Fig. 13(a), consist of 6 nm thick Fe bars on a c(4x4) reconstructed surface of a 1 μm thick GaAs epilayer with carrier density $n = 5 \times 10^{16}\,\mathrm{cm}^{-3}$. A 15 nm thick, much higher doped GaAs surface layer ensures efficient spin injection. The center contacts have widths of 6, 2 and 1 μm, with edge-to-edge gaps of 3 and 4.5 μm, respectively. Further device details are described in [129]. A current is applied flowing from the injector 2 to the 100 μm distant contact 1. A non-local voltage V_{NL} is measured between contacts 3 and 5 outside the charge current path, see Fig. 13(a).

V_{NL} is detected by standard lock-in techniques using a small ac-modulation I_{AC} on top of a dc-injection current I_{DC}. The measurements are performed in a dilution refrigerator equipped with a home-built 3-axis vector magnet, allowing us to determine the magnetization direction of the iron bars to better than 1° by rotating the magnetic field during continued spin-valve measurements.

Hanle satellite peaks

Electron spin polarization pointing along the Fe easy-axis $\hat{\mathbf{x}}$ is injected into the semiconductor below contact 2 [128, 147], diffuses away and can be detected at contact 3 (the electron spin diffusion length exceeds the detector distance [129]). DNP can easily be produced in presence of non-zero I_{DC} [127, 129, 175], where the electron spins are imprinted onto the nuclear spins via flip-flops. The nuclear spin polarization then acts back on the electron spins as an effective Overhauser field B_N [124] causing electron spin precession. In a perpendicular field B_Z, the electron spins precess, diffuse and dephase, giving a characteristic Hanle peak around $B_Z = 0$ [128, 137, 152]. For $\mathbf{B_N}$ antiparallel to $\mathbf{B}$, additional satellite peaks, see Fig. 13(b), appear [129] when dephasing is suppressed by a cancellation of the external field by the internal Overhauser field: $\mathbf{B} = -\mathbf{B}_N$. In the following, we will use this well established signature as a sensitive measure for the nuclear field B_N [108, 129, 176, 177]. Nuclear fields achieved are $\sim 50\,\mathrm{mT}$, roughly one percent of the $5.3\,\mathrm{T}$ for fully polarized nuclei in GaAs [105]. The average nuclear field B_N in our experiments is linear in B_X [129] along the Fe bars and for the following we fix $B_X = -1.5\,\mathrm{mT}$.

4.4 Nuclear relaxation measurements: the pump-probe cycle

The pump-probe cycle used to find the NSR times is sketched in Fig. 14(a). First, a nuclear polarization is built-up by DNP while continuously sweeping B_Z back and forth (‘initialize’), see Fig. 14(b), until a steady state is reached, typically after an hour. The asymmetry, alternating positions and alternating widths of the satellite peaks are a consequence of ramping and alternating sweep directions (DNP is most efficient at $B_Z \sim 0$ followed by slow decay at $B_Z \neq 0$ during ramping). After initialization, DNP

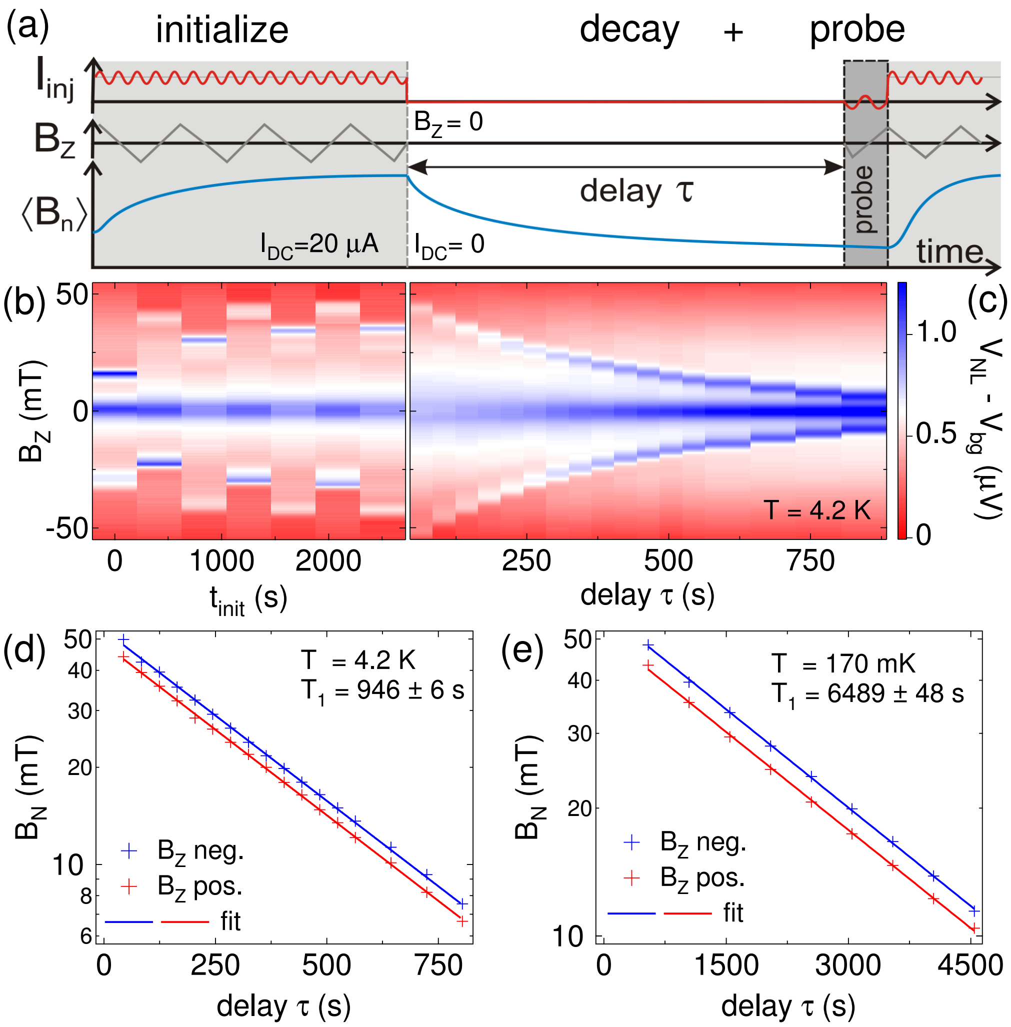

Figure 14: (a) Pump-probe scheme used to measure the nuclear spin relaxation rate. (b) Initialization: Alternating B_Z Hanle sweeps $(0.3\,\mathrm{mT/s})$ with $I_{DC} = 20\,\mu\mathrm{A}$, see text. Sweeps start at $B_Z = +75\,\mathrm{mT}$ and then run between $B_Z = \pm 75\,\mathrm{mT}$. (c) B_Z probe-traces $(0.9\,\mathrm{mT/s})$ after a delay τ. Time-decay of the satellites is clearly visible. A parabolic background was subtracted (same for all τ). (d) and (e) Log-plot of Overhauser field B_N (crosses) – extracted from satellite peak positions such as in (c) – as a function of τ at 4.2 K in (d) and 170 mK in (e). Blue data is from satellites at $B_Z < 0$, red from $B_Z > 0$. *Single*-exponential fits (solid lines) give excellent agreement, and long T_1 times characteristic of NSR.

is switched off ($I_{DC,AC} = 0$) and B_Z is ramped to zero. The nuclear polarization is then allowed to decay for a time τ ('decay'), keeping $B_X = -1.5\,\mathrm{mT}$ fixed. Subsequently, a fast Hanle scan to read out B_N is performed ('probe') with only a small I_{AC} and $I_{DC} = 0$ to avoid further DNP during probing.

4.5 Single exponential decay of the Overhauser field

Repeating this cycle for various delays τ (including reinitializing each time), data sets reflecting the decay of B_N over time are obtained, as shown in Fig. 14(c). By fitting Lorentzians to the satellite peaks, we determine B_N (peak position) as a function of τ, as shown in Fig. 14(d)/(e) (crosses), for both positive (red) and negative (blue) B_Z satellites. The small difference between the two satellite positions is a result of slow ramping. From single-exponential fits, we get excellent agreement with the data, and T_1 times which are the same within the error bars for the two satellites. Further, we observe sharpening of the satellites with growing τ, indicating increasing homogeneity of the nuclear spins with time. At temperatures above 1 K, the T_1 times obtained here are in good agreement with previous T_1 measurements by NMR for all three isotopes (^{69}Ga,^{71}Ga,^{75}As) at comparable charge density [180, 183].

4.6 Temperature dependence of the nuclear T_1 time

The temperature dependence of the NSR rate is shown in Fig. 15 on a log-log plot for two cool downs (open and closed squares) of the same sample. Measurements of a second sample (not shown) fabricated from another part of the same wafer give very similar results. Both ac and dc currents were chosen to avoid self-heating over the measured T-range. However, in the refrigerator used, sample temperatures saturate around 100 mK due to poor thermalization, causing the relaxation rates to saturate at 100 mK. Nevertheless, at the lowest temperatures, very long T_1 times exceeding 3 hours are found. Since the NSR rate in the log-log plot is linear over two orders of magnitude in T, we fit a power law $1/T_1 \propto T^\alpha$ for $0.1\,\mathrm{K} \leq T \leq 10\,\mathrm{K}$ and find $\alpha = 0.6 \pm 0.04$. The data at $T > 10\,\mathrm{K}$ is excluded from the fit due to well known phonon contributions [130]. For comparison, the Korringa law extrapolated from NMR data at $T > 1\,K$

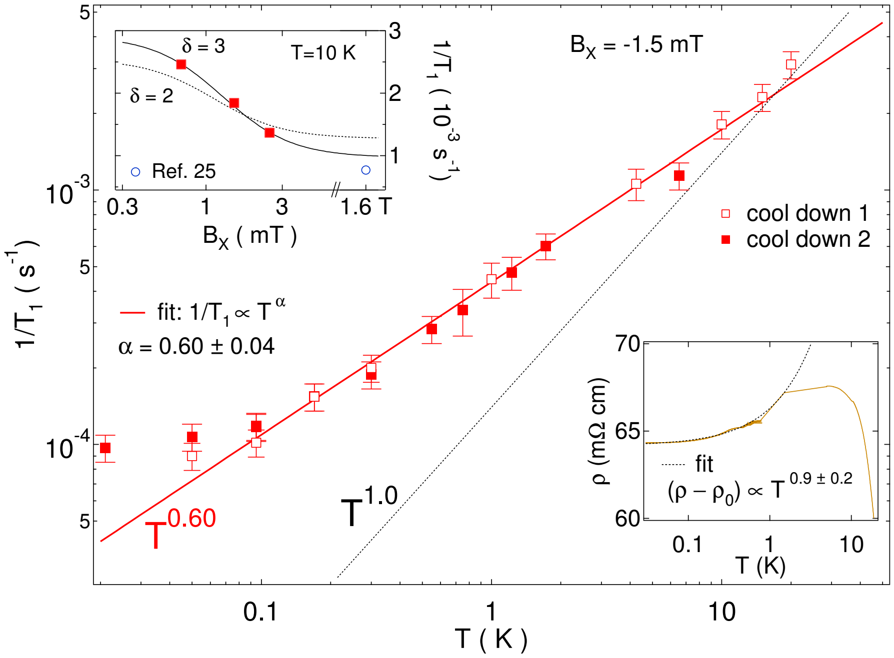

Figure 15: The nuclear spin relaxation rate $1/T_1$ versus temperature measured for two cool downs (open and solid squares) on the same sample, always for $B_X = -1.5\,\mathrm{mT}$. Error bars are from repeated measurements. The solid line is a power-law fit $1/T_1 \propto T^\alpha$ giving $\alpha = 0.6 \pm 0.04$ for $0.1\,\mathrm{K} \leq T \leq 10\,\mathrm{K}$. As a comparison, an estimated Korringa law $1/T_1 \propto T$ is added (dashed line) based on NMR data [183], see text. Upper inset: B_X dependence of the nuclear T_1-rate at $T = 10\,\mathrm{K}$ with theory (black curves, eq. (37)), see text. An NMR data point at $B = 1.6\,T$ and $T = 10\,K$ from Ref. [183] is also added (rescaled using $1/T_1 \propto n^{2/3}$ to match the carrier density here), demonstrating very good agreement with the present spin-valve data. Lower inset: T-dependence of the resistivity from van der Pauw measurements on the same GaAs wafer, indicating metallic behavior for $T < 10\,\mathrm{K}$. Dashed curve is a fit for $0.1\,K \leq T \leq 1\mathrm{K}$ to $(\rho(T) - \rho_0) \propto T^\gamma$ giving $\gamma = 0.9 \pm 0.2$.

[183] is indicated in Fig. 15 (dashed line), rescaled from high density $n = 2 \times 10^{18}\,\mathrm{cm}^{-3}$ where the Korringa law holds to match the density in our samples using $1/T_1 \propto n^{2/3}$ (Korringa scaling) and field corrected from 1.6 T (NMR data) to 1.5 mT with a factor of 1.9 (see upper inset in Fig. 15). The Korringa T-dependence is clearly inconsistent with our data, which decreases more weakly with T and gives relatively fast NSR rates at low-T.

4.7 Discussion of nuclear relaxation mechanisms

We now discuss the possible mechanisms of the nuclear spin relaxation responsible for the temperature dependence of the T_1^{nuc} rates.

4.7.1 Phonon relaxation and diffusion

First, we exclude phonon contributions since these have been shown to be relevant only well above 10 K and further would result in a quadratic temperature dependence [130, 183]. Also, NSR by paramagnetic impurities is known to be very weak in GaAs [183]. Next, we consider nuclear spin diffusion out of the 1 μm thick epilayer. This random-walk process is in principle temperature independent in the regime applicable here and is inconsistent with the clear single-exponential decay of $B_N(\tau)$ which we find for all temperatures, also making it unlikely that the observed low-T saturation of T_1^{-1} is caused by nuclear spin diffusion. Therefore, we can exclude diffusion alone as a relevant relaxation channel.

4.7.2 Hyperfine relaxation in non-degenerate semiconductors

Next, we consider the hyperfine Fermi contact interaction as a possible NSR mechanism. In non-degenerate semiconductors, where the Fermi energy is well below the conduction-band edge, the mobile charge carriers follow a Boltzmann distribution, and the nuclear spin relaxation rate is $T_1^{-1} \propto \sqrt{T}$ [120], not far from the measured $T_1^{-1} \propto T^{0.6}$. However, since here $E_F \gg k_B T$ and since the measured resistivity $\rho(T)$ in the relevant temperature range $T < 10\,\mathrm{K}$ does not display a thermally activated behavior expected for a non-degenerate semiconductor (see lower inset of Fig. 15), this mechanism is most likely not applicable here.

4.7.3 Hyperfine relaxation in normal metals

In simple metals and degenerate semiconductors, the Korringa law is expected [120, 133]

$$\frac{1}{T_1} = \frac{256\pi^3}{9\hbar}\frac{\gamma_n^2}{\gamma_e^2}\, n^2|\phi(0)|^4\chi^2 \cdot k_B T\ , \tag{36}$$

with gyromagnetic ratio γ_n of the nuclei and γ_e of the electrons, electron spin susceptibility χ and $n\,|\phi(0)|^2$ is the electron density at the nuclear site. Indeed, this temperature dependence is observed in much more highly-doped bulk GaAs ($n = 2 \times 10^{18}\,\mathrm{cm}^{-3}$) [183] measured with NMR above 1 K, but is not seen in the present samples.

4.7.4 Field dependence of the nuclear relaxation and the correlated local environment

To learn more about the mechanism of NSR present here, we investigate the B_X dependence of T_1^{-1}, shown in the upper inset of Fig. 15 at 10 K. Note that $B_Z = 0$ during the decay step of the T_1 measurement. A clear reduction of relaxation rates is seen for increasing B_X, as expected for applied fields comparable with B_L, which is the local rms field acting on each individual nuclear spin, including nuclear dipole-dipole fields B_d and electronic Knight fields. The theoretically expected rate is [135, 185]

$$T_1^{-1}(B) = a\frac{B^2 + \delta(5/3)B_L^2}{B^2 + (5/3)B_L^2}\ , \tag{37}$$

with large-field rate $a = T_1^{-1}(B \gg B_L)$. Note that the zero-field rate $T_1^{-1}(B = 0) = \delta a$ and the correlation parameter δ is ranging from 2 for uncorrelated to 3 for fully spatially correlated fields B_L. Independent measurements give a very small B-field offset $<$ 0.1 mT, which we assume to be zero here. We perform a fit and obtain $\delta = 3.0 \pm 0.3$, $B_L = 1 \pm 0.2\,\mathrm{mT}$ and $a = (9.6 \pm 1.5) \times 10^{-4}\,\mathrm{s}^{-1}$. The dashed curve shows a best-fit with $\delta = 2$, clearly inconsistent with the present data. Taking the B-dependence from $\delta = 3$ theory (solid curve, upper inset Fig. 15), this brings the spin-valve NSR rate at $B_X = -1.5\,\mathrm{mT}$ into very good agreement with NMR data measured at $B \sim 1.6$ T and the same $T = 10\,\mathrm{K}$ [183] (blue circle). Since $\delta = 3$, B_L is spatially highly correlated with a local field B_L much larger than the estimated $B_d \sim 0.1\,\mathrm{mT}$ [105] alone. This suggests an electronically induced hyperfine mechanism causing NSR, due to electrons extended on a length scale much larger than the lattice constant $a_0 = 5.7\,\text{Å}$.

4.7.5 Metallic resistivity in the impurity band

Since NSR appears to be electron mediated, we now discuss electronic transport measurements characterizing the epilayer. The lower inset of Fig. 15 shows $\rho(T)$ from van der Pauw measurements done on separate samples from the same wafer. Clearly, metallic behavior ($d\rho/dT > 0$) is seen for $T < 10\,\mathrm{K}$, as expected for the present doping of $5 \times 10^{16}\,\mathrm{cm}^{-3}$, well above the well-known MIT in GaAs at $\mathrm{n_c} \sim 2 \times 10^{16}\,\mathrm{cm}^{-3}$ [26]. However, $\rho(T)$ is only weakly T-dependent below 4 K and follows $(\rho(T) - \rho_0) \propto T^{0.9\pm0.2}$ for $0.1\,\mathrm{K} \leq T \leq 1\,\mathrm{K}$, deviating from the expected $\propto -T^{1/2}$ for the weak localization and Altshuler-Aronov corrections in 3D [184]. We note that the simple Fermi liquid (FL) $\propto T^2$ is not expected here [186]. Above 10 K, $\rho(T)$ shows simple thermal activation of donors [183]. The carrier density at 4 K is the same as at base temperature (within measurement error), therefore excluding significant T-dependent carrier localization below 4 K. Further, a perpendicular magnetic field has no significant effect for $\mathrm{B} < 5\,\mathrm{T}$ and gives a positive magnetoresistance at larger fields. Therefore, the resistivity data shows clear metallic behavior, lacking any hints of incipient localization.

In addition, control experiments have confirmed that the highly-doped surface layer does not significantly contribute to lateral transport apart from facilitating the spin injection. The interaction parameter $r_S = E_C/E_F$ is about 0.6, with Fermi energy $E_F = 7.4\,\mathrm{meV}$ and average Coulomb energy $E_C = 4.1\,\mathrm{meV}$, indicating that the samples are approaching the interacting regime $r_S \gtrsim 1$. Further, disorder is quite strong: $k_F \ell \sim 1.7$, with a transport mean free path $\ell = 15\,\mathrm{nm}$ for $T < 10\,\mathrm{K}$. Therefore, the epilayer behaves like a degenerately doped semiconductor showing clear metallic behavior, in the interacting and strongly disordered regime.

4.7.6 Breakdown of the Korringa law in a disordered, interacting metal

Returning now to the NSR mechanism, the Korringa formula eq. (36) (where free electrons were assumed) would need to be properly recalculated, including the combined effects of disorder and interactions not far from the MIT. In lack of an appropriate theory in this regime, naively, a renormalized, temperature dependent electron spin susceptibility $\chi(T)$ can be introduced in eq. (36) [184, 187–192]. Here, $\chi \propto T^{-\beta}$ with $\beta = 0.2 \pm 0.02$ would be required to result in $T_1^{-1} \propto T^{0.6}$ as measured, assuming no other T dependencies in eq. (36). While $\beta = 0$ corresponds to a regular FL, $\beta = 0.2$ is in good agreement with expectations ($0 < \beta < 1$) for the regime often associated with coexistence of localized moments and itinerant electron states well within the metallic density range [37, 38]. Also, such a low-temperature divergence of the spin susceptibility $\chi \propto T^{-\beta}$ has been observed in other semiconductors for $n \gtrsim n_c$ above but not far from the MIT [36, 193, 194]. The density dependence of β would be interesting to investigate, indeed, but is beyond the scope of this study.

4.8 Inhomogeneity of the nuclear polarization and double satellite peaks

Finally, we investigate nuclear spin inhomogeneities apparent in the Hanle measurements. When fixing $\mathrm{B_Z} = 0$ during initialization, significantly broadened satellite peaks result, see Fig. 16(a)/(b), though the extracted NSR rates remain unchanged within experimental error (not shown). As seen by comparing Fig. 14(c) with Fig. 16(b), sweeping B_Z (during initialization) has the effect to narrow the Hanle peaks, apparently homogenizing the nuclear spins.

Further, we find additional satellite peaks, see Fig. 16(c)/(d), suggesting two distinct species of electrons and/or nuclear polarization regions. We note that the extra satellites are visible whenever they are sufficiently sharp and well-enough separated, independent of the current direction and the sign of B_X. Further studies are needed to elucidate these additional satellite peaks as well as inhomogeneity effects.

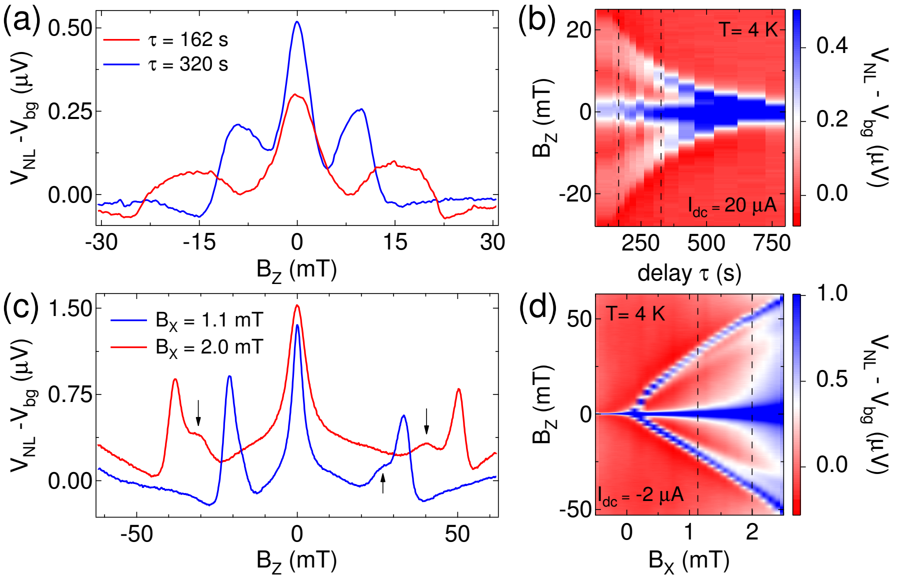

Figure 16: (a) and (b) are Hanle probe sweeps with $B_Z = 0$ during initialization, showing broadened Hanle peaks but resulting in very similar NSR rates (not shown). (c) and (d): Double satellite peaks in slow Hanle measurements (0.25 mT/s) become visible (arrows in (c)) for $B_X > 0.8\,\mathrm{mT}$.

4.9 First summary

In summary, using a new, versatile method to measure NSR in spin-valve devices, we report the breakdown of the Korringa-law in GaAs doped a factor of ~ 2.5 above the MIT displaying clearly metallic conductivity. Over a factor of 100 in T, the NSR rate follows a rather weak power-law $1/T_1 \propto T^{0.6}$, resulting in relatively strong coupling and NSR rates enhanced beyond the Korringa law at low-T, potentially useful for nuclear cooling. This power-law is consistent with a weakly diverging electron spin susceptibility $\chi \propto T^{-0.2}$ in the simultaneously interacting and disordered metallic-regime not far from the MIT currently lacking appropriate theory.

Acknowledgments

We are very thankful for discussions with B. Braunecker, D. Loss, M. Maslov, and S. Valenzuela. This work was supported by the Swiss Nanoscience Institute (SNI), Swiss NSF, NCCR NANO, NCCR QSIT and an ERC starting grant (D.M.Z.).

5 Transport spectroscopy of disordered graphene quantum dots etched into a single graphene flake

Dominikus Kölbl, Dominik M. Zumbühl
Department of Physics, University of Basel, Klingelbergstrasse 82, CH-4056 Basel, Switzerland

Abstract

We present transport measurements of graphene dots of sizes 45, 60 and 80 nm etched into a single graphene flake, allowing a size comparison avoiding effects from different flakes. The transport gap and Coulomb energies increase with decreasing dot size, as expected, and display a strong correlation, suggesting the same physical origin for both, i.e. disorder-induced localization. A dominant role of disorder is further substantiated by the gate dependence and the magnetic field behavior, allowing only approximate identification of the electron-hole crossover and spin filling sequences. Finally, we extract a g-factor consistent with $g = 2$ within the error bars.

This chapter will be submitted for publication in Nano Letters.

5.1 Introduction

Spins in condensed matter systems have become an important field of research motivated by spintronics and quantum information and the underlying fundamental physics. Graphene has several exceptional properties [48] and is an exciting material promising long spin relaxation and coherence times as a result of weak spin-orbit interaction and weak hyperfine effects due to the predominant natural abundance of the nuclear-spin free ^{12}C [12, 14]. Recent progress taking micron-scale 2D systems [44, 45] to nano-scale ribbons and quantum dots has opened the door to study the physics of confined charges and spins in graphene [77, 93, 195–198], paving the way towards nano-device applications. Challenges include overcoming the gapless nature of graphene [77, 195, 196], defining tunnel barriers [197], and achieving controlled tunability of devices [199].

Despite these significant advances, most experiments in graphene nano-devices are currently dominated by disorder, often masking the intrinsic (graphene) physics. Disorder is thought to arise from surface, substrate and edge imperfections as well as intrinsic graphene defects. Investigating and suppressing disorder is therefore crucial for further progress. Further, when studying graphene nano-devices, it is important to change the relevant parameters such as dot size or ribbon width without significantly or qualitatively changing disorder.

5.2 Device structure and fabrication

Here, we report electronic transport spectroscopy of quantum dots of three different sizes fabricated on the same graphene sheet with essentially identical disorder broadening of the Landau levels across the entire graphene flake.

The devices are approximately square-shaped graphene quantum dots with designed widths $w = 45$, 60, and 80 nm placed on the same graphene sheet exfoliated from HOPG onto a Si wafer [9] with a backgate separated by a 294 nm thick oxide [200]. Ti/Au (5/40 nm) contacts are defined via standard e-beam lithography (EBL). Dots with slightly narrower connections to the graphene reservoirs are etched with an Ar/O$_2$ plasma using a PMMA-mask predefined in a second EBL step. The insets in Figure 17a-c show AFM images of each dot. The fabricated devices are a few nm smaller in diameter than designed due to slight under-etching. Graphene regions separated from the dots by 15-25 nm wide etched trenches are also contacted and used for side gating the dots individually with side gate voltage V_{SG}. The overall charge density can be tuned with back gate voltage B_{BG}.

Two-terminal measurements in the quantum Hall regime [201] using bulk regions of the flake showed it to be single-layer graphene. We extract a field-effect mobility of about 3'000 $\mathrm{cm}^2/\mathrm{Vs}$ at a density of $2 \mathrm{x} 10^{11} \mathrm{cm}^{-2}$ before removal of PMMA. This mobility is a lower bound as the PMMA was removed prior to the measurements presented below. High-field Landau level broadening in the four graphene regions surrounding the three quantum dots distributed across the $\sim 20\,\mu$m long graphene sheet was essentially identical in each region, indicating homogeneous disorder across the entire graphene flake and therefore for all three dots, allowing a size-comparison of transport properties without significantly changing disorder. The backgate voltage $\mathrm{V}_{BG} = 0$ except where stated otherwise. Measurements are performed in a dilution refrigerator unit at $T = 4\,\mathrm{K}$ and $T \sim 100\,\mathrm{mK}$ (electron temperature). Conductance across the graphene nano ribbons (GNRs) is probed with a standard lock-in technique using a small ac modulation on top of a variable dc-bias.

5.3 Observation of the low-temperature transport gap in graphene quantum dots

First, we investigate the transport gap as a function of side gate voltage V_{SG} for each dot, shown in Figure 17a-c at 4K. Around the charge neutrality point (CNP) located within a few volts from zero gate voltage similar for all dots, we find a strongly suppressed conductance with sharp characteristic Coulomb blockade (CB) peaks over a wide range of gate voltages and strong conductance fluctuations at elevated densities, both typical for GNR devices measured at low temperatures [77, 196–198]. The extent in side gate voltage ΔV_{SG} of this transport gap region is extracted by evaluating the maximum difference between gate voltages where the valley conductance is suppressed below $10^{-4}\,\mathrm{e}^2/\mathrm{h}$ as indicated by the gray bars in Figure 17a-c. The resulting transport gap, shown in Figure 17d, is strongly size dependent, giving larger gaps for the smaller

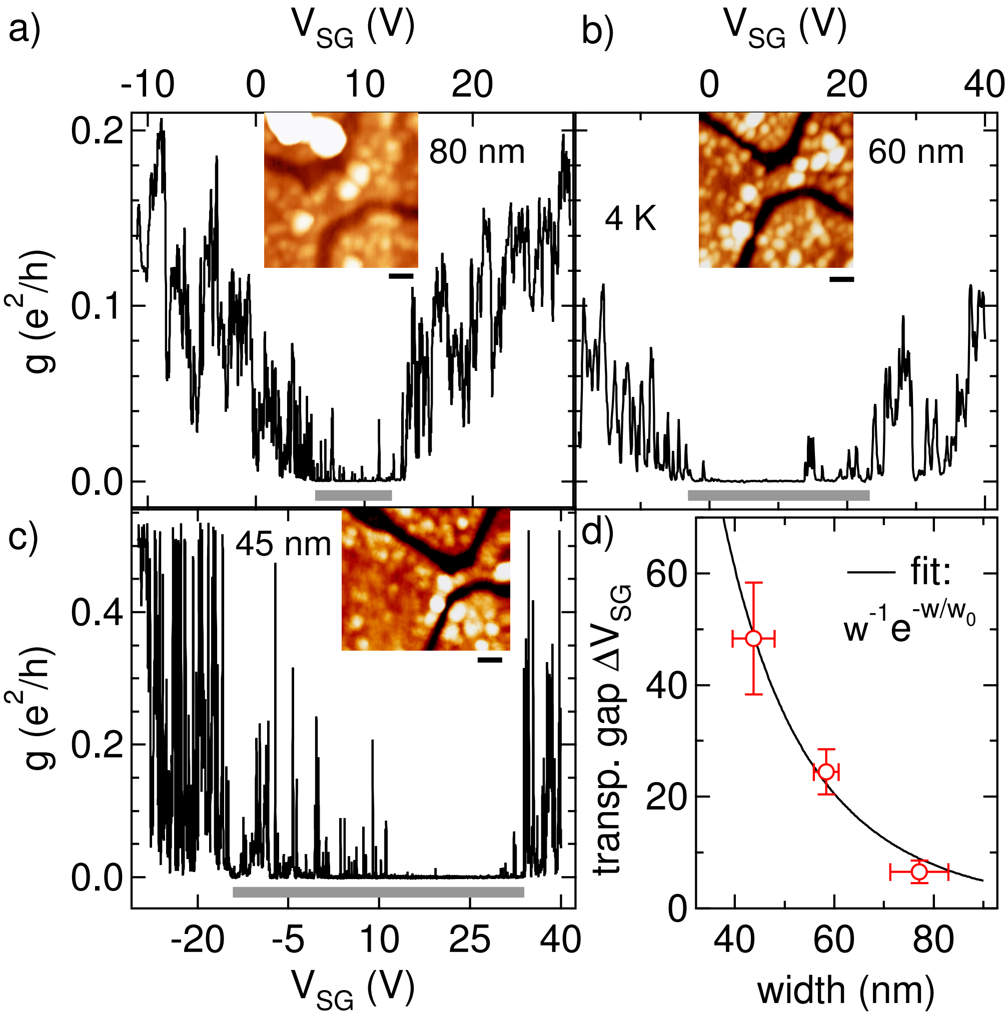

Figure 17: **Transport gaps at 4K.** (a)-(c) Zero dc-bias differential conductance g as a function of side gate voltage V_{SG} for each dot as labeled. The gray bars indicate the transport gap ΔV_{SG}, defined as the V_{SG} range around the charge neutrality point where the valley conductances remain smaller than $10^{-4}\,e^2/h$. The insets show AFM-images (all scale bars 50 nm). White speckles presumably are PMMA or other residues. (d) Transport gap ΔV_{SG} determined from (a)-(c) (open circles) as a function of dot size. The solid curve is a fit to Ref. [202], see text.

devices, as expected [77, 79, 203].

5.4 Size dependence of the transport gap

Several theories predict the formation of a confinement gap E_g in graphene, including tight-binding [80], *ab-initio* [82], Anderson localization [204], and many-body theory [202], all giving similar results. The latter suggests a width w dependence given by $E_g \sim w^{-1} e^{-(w/w_0)}$ (with decay length w_0), which is widely used to analyze experimental results and also fits our data $\Delta V_{SG}(w)$ quite well using $w_0 = 29.4 \pm 4.2\,nm$ (see Fig.1(d)). However, converting ΔV_{SG} to energy ($\delta E = \alpha_{SG} \cdot \Delta V_{SG}$) using an average lever arm $\alpha_{SG} = 0.117 \pm 0.049$ eV/V extracted from CB diamonds (see below, Fig.2(c)) results in an absolute energy scale of several eV, far exceeding predictions for a simple confinement induced band gap by about two orders of magnitude. Therefore, the transport gap ΔV_{SG} most likely is not due to geometric confinement only. Further, the appearance of numerous CB peaks (rather than a large region of very low conductance) and conductance fluctuations surrounding the transport gap indicate the strong influence of disorder. A large transport gap could then result from disorder localization and Coulomb blockade in presence of a much smaller confinement gap necessary to inhibit Klein tunneling [53].

5.5 Edge roughness and charged impurities

Possible sources of this disorder include graphene defects and edge disorder, trapped charges nearby, partially due to adsorbates and PMMA residues which are clearly visible in AFM images throughout the devices (see Figure 17, insets), as well as other substrate and surface disorder. However, since all dots are fabricated on the same graphene sheet showing nearly identical Landau level broadening in all regions across its length, we expect this disorder to be of similar quality for the three dots. We note that the importance of a fabrication induced edge roughness of the order of a few nm should increase from the 80 nm to the 45 nm device, where it is reaching 10% of the device width [86, 204].

5.6 Size dependence of Coulomb blockade in graphene quantum dots

Clear Coulomb diamonds are seen in finite bias measurements for all three dots, shown in Figure 18a,b for the larger dots at 100 mK, indicating the formation of a tunnel coupled quantum dot in the transport gap region. We find signatures of excited states in sequential tunneling (typically at ∼meV energies), but also cotunneling features. We extract the addition energies E_A and V_{SG} lever arms from similar data extending over a larger V_{SG}-range for the two larger dots, shown in Figure 18c. Both dots show similar lever arms, as expected due to similar geometry, roughly independent of V_{SG}. The addition energies are larger in the smaller dot, on average, as expected. Further, a maximum in E_A as a function of V_{SG} – indicated by the blue dashed curves – is seen close to the bulk CNP, roughly marking the electron-to-hole crossover. However, we cannot identify the zero-occupation diamond and the absolute charge-number in these dots, though the expected confinement-induced band gap [82] is comparable to the observed addition energies. Overall, the findings strongly indicate predominant transport across single quantum dots within these devices.

The size dependence of the average addition energy $\langle E_A \rangle$ obtained from Coulomb diamond measurements over a large gate voltage range is shown in Figure 2d (red squares), in good agreement with previous reports of similar size devices (black circles) [196, 197, 199, 205, 206]. Decent agreement is found with $\langle E_A \rangle = \epsilon / w$ [202] (see dashed curve), resulting in $\epsilon = 870 \pm 70\,\mathrm{meV\,nm}$, in agreement with expectations for single dots [202] and with other experiments [77, 79]. Interestingly, for the present three dots, we find a clear correlation between the average addition energy $\langle E_A \rangle$ and the transport gap size ΔV_{SG} (see inset Figure 2d), suggesting the same physical origin for both energy scales.

5.7 Single- to double-dot transitions by electrostatic tuning

However, we also find a number of overlapping diamonds or diamonds that do not close at low bias, indicating formation of double or multiple dots [210] in a repeatable way (during the same cool down) as a function of gate voltage. This is further substantiated

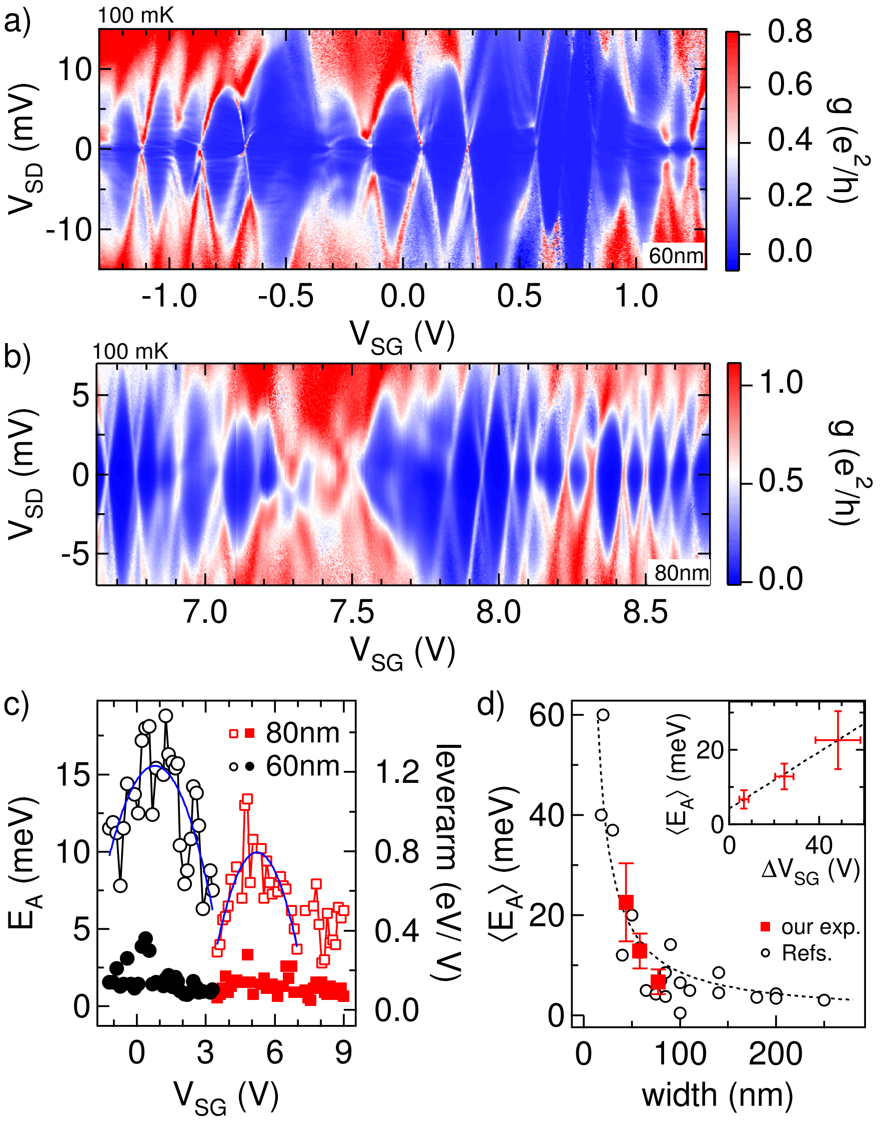

Figure 18: **Coulomb diamonds** (a),(b) Differential conductance (color scale) as a function of source-drain voltage V_{SD} and side gate voltage V_{SG} at $T \sim 100$ mK of the 60 and 80 nm dots, as labeled. (c) Addition energies (left axis, open symbols) and corresponding V_{SG} lever arms (right axis, filled symbols) from Coulomb diamonds as in (a) and (b) but with extended V_{SG} range. Blue curves (parabolas) are shown as a guide to the eye, indicating a peak in E_A at the CNP for both dots, also confirmed by $B_\perp$ data, see text. (d) Size-dependence of the average addition energy $\langle E_A \rangle$ (squares). Error bars denote standard deviation. Circles are from Refs. [196, 197, 199, 203, 205–209]. The dashed curve is an ϵ/w fit with $\epsilon = 870 \pm 70$ meV nm, see text. The inset shows $\langle E_A \rangle$ vs. ΔV_{SG} with a line fit (dashed black) indicating a strong correlation.

by V_{SG} and V_{BG} scans shown in Figure 19a,b. Regions in gate space of single-sloped, parallel lines arising from a single dot are alternating (again repeatable in gate voltage) with non-parallel, honey-comb like features [195, 206, 211], indicating double or multiple-dot formation [212] reflecting the pronounced disorder potential. As gate voltage is changed monotonously, the dot appears to sporadically rearrange its geometry, deforming between a simple, single dot and more complicated configurations.

Nevertheless, we observe good agreement of the addition energies and the calculated gate capacitances following a simple parallel plate capacitor model and using the relative gate leverarms for the 60 and 80nm device. This is different for the 45 nm device as the etched trenches separating the GNR from its side gates are no longer small compared to the dot size giving additional contributions. We conclude that apart from disorder induced variations of the confinement potential our short GNRs mainly form single quantum dots.

5.8 The electron-hole crossover of graphene quantum dots in perpendicular magnetic fields

We now turn to perpendicular magnetic field $B_\perp$ measurements, shown in Figure 3c-e for all three dots at $V_{SD} = 0$ and $T = 100\,\mathrm{mK}$. Besides a strong variation of the peak conductance, the peak positions of the 80 nm-device bend towards $V_{SG} \sim 5\,\mathrm{V}$ for large $B_\perp$, as expected for the $0th$ graphene Landau level at the CNP [207, 213, 214]. Therefore, we can extract the CNP in this device to be located around 5 V, consistent with the highest value of E_A found for $V_{SG} = 4.8\,\mathrm{V}$ (Figure 2c). Similarly, for the 60 nm device, the electron-hole crossover is found around $V_{SG} \sim 1\,\mathrm{V}$, again consistent with the previously determined maximal E_A at $V_{SG} = 1.25\,\mathrm{V}$ (Figure 2c), though for this devices the $B_\perp$ bending of the peaks is weaker. Therefore, the CNPs in both dots are separated by only a few Volts, both close to zero. Landau level bending becomes visible at high fields when the magnetic length $l_B = \sqrt{\hbar/eB}$ is much smaller than the device size w [213, 214], making the effect weakest in the smallest dot (Figure 3e).

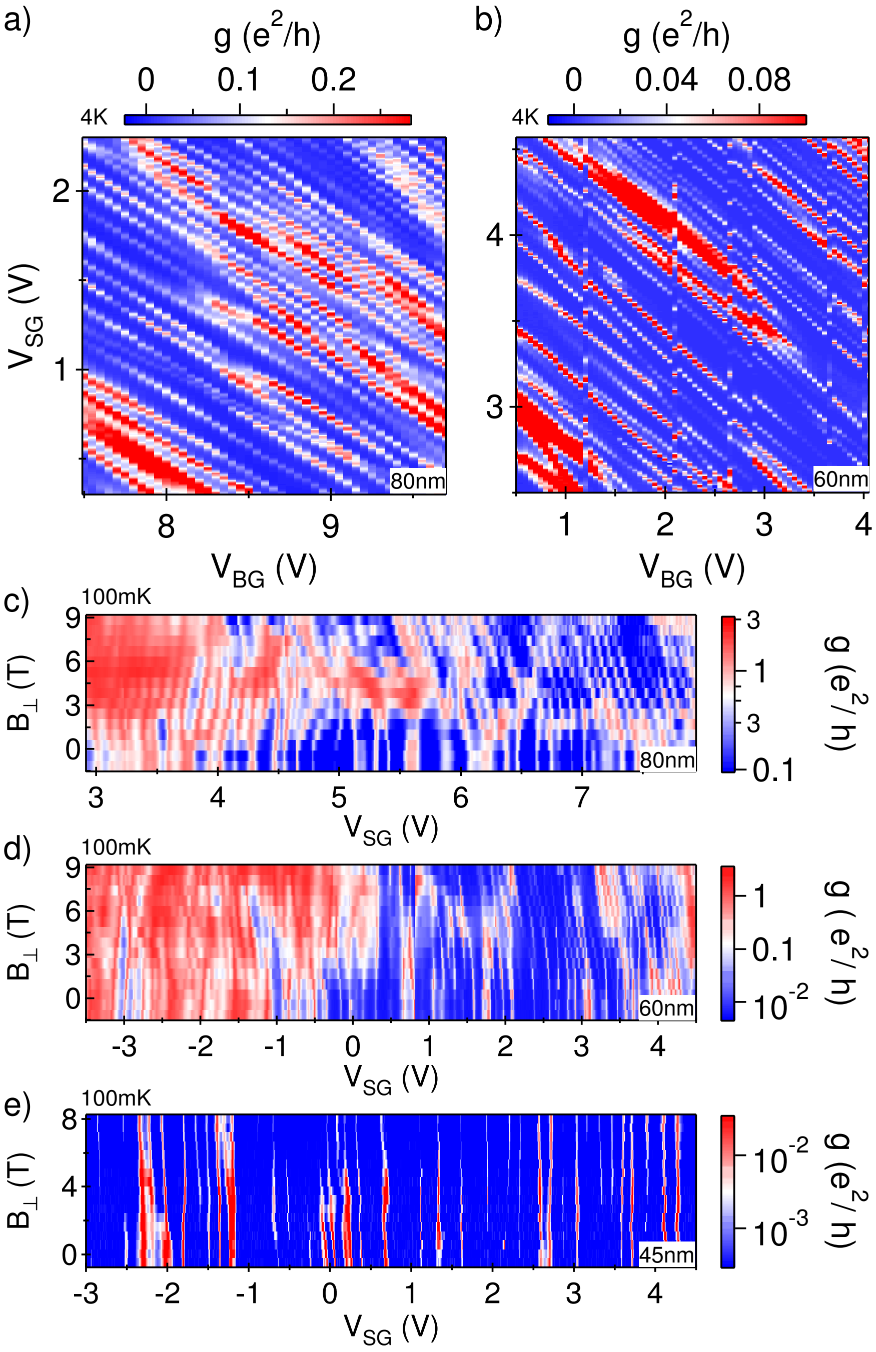

Figure 19: **Gate-gate sweeps and $B_\perp$ peak motion:** (a),(b) Differential conductance showing CB peaks as a function of V_{SG} and V_{BG} at 4 K. Parallel lines indicating single dot behavior alternate with wiggly and merging features that can arise from multiple-dot formation (repeatable). (c)-(e) CB peak evolution in a perpendicular field $B_\perp$ of the 80, 60 and 45 nm dots at 100 mK. At large $B_\perp$, peaks bend towards the graphene zero Landau-level around the electron-hole transition ($V_{SG} \sim 5$ V for 80 nm dot, and $V_{SG} \sim 1$ V for 60 nm dot), more clearly visible for the larger dots, see text.

5.9 Orbital effects of perpendicular fields on spin-pairs

Beyond Landau levels, paired peak motion due to consecutive filling of the same orbital with opposite spins (spin pairs) can also be observed in the $B_\perp$ dependence. Here, this is most clearly visible for the largest device (where the $\mathrm{B}_\perp$ effect is most pronounced), where some pairs particularly at high and low densities away from the CNP exhibit reproducible parallel evolution over a significant range in $B_\perp$, see e.g. Figure 19c, $3\,\mathrm{V} < V_{SG} < 4.5\,\mathrm{V}$. However, the low-density region around the CNP which is more strongly affected by disorder [214] appears more complicated and clear pairs could not be found, similar to the smaller dots, which are also more weakly coupled to the reservoirs. These efforts are further hampered by disorder driven dot rearrangements (single to double dot transitions as a function of V_{SG}) as described before and sporadic switching in gate voltage observed in these devices.

5.10 Graphene quantum dots in parallel magnetic fields

The evolution of the CB peak spacing in an in-plane magnetic field $B_\parallel$ reflects the spin filling sequence. In graphene quantum dots, spin-orbit coupling can be assumed to be very weak and the Landé g-factor $g \sim 2$. For dot-diameters $d < 100\,\mathrm{nm}$, the orbital level spacing $\Delta \gg 1\,\mathrm{meV}$ remains much larger then the Zeeman splitting $E_Z = g\mu_B B$ (with Bohr magneton μ_B) for $B_\parallel \leq 10\,\mathrm{T}$. In this case, and if electron-electron interactions are negligible, one might expect a simple alternating Pauli spin sequence giving peak spacings which increase or decrease with slope $g\mu_B$. $B_\parallel$-independent peak spacings (slope zero), however, would be absent in this simple picture, since these indicate a filling of two subsequent identical spins induced by interactions [215], resulting in total spin $S > 1/2$.

Figure 20a,b shows the CB peak positions of the 80 nm and 60 nm devices at 100 mK as a function of $B_\parallel$ (separate cool down) over a range of V_{SG} including the electron-hole transitions. We fit Gaussians to the CB peaks to obtain the peak positions and evaluate the peak spacing as a function of $B_\parallel$. While some peak spacings show the expected slopes (zero or $\pm g\mu_B$), others exhibit more complicated, nonlinear $B_\parallel$ dependence. This could be due to disorder driven dot-rearrangements as a function of V_{SG} as mentioned

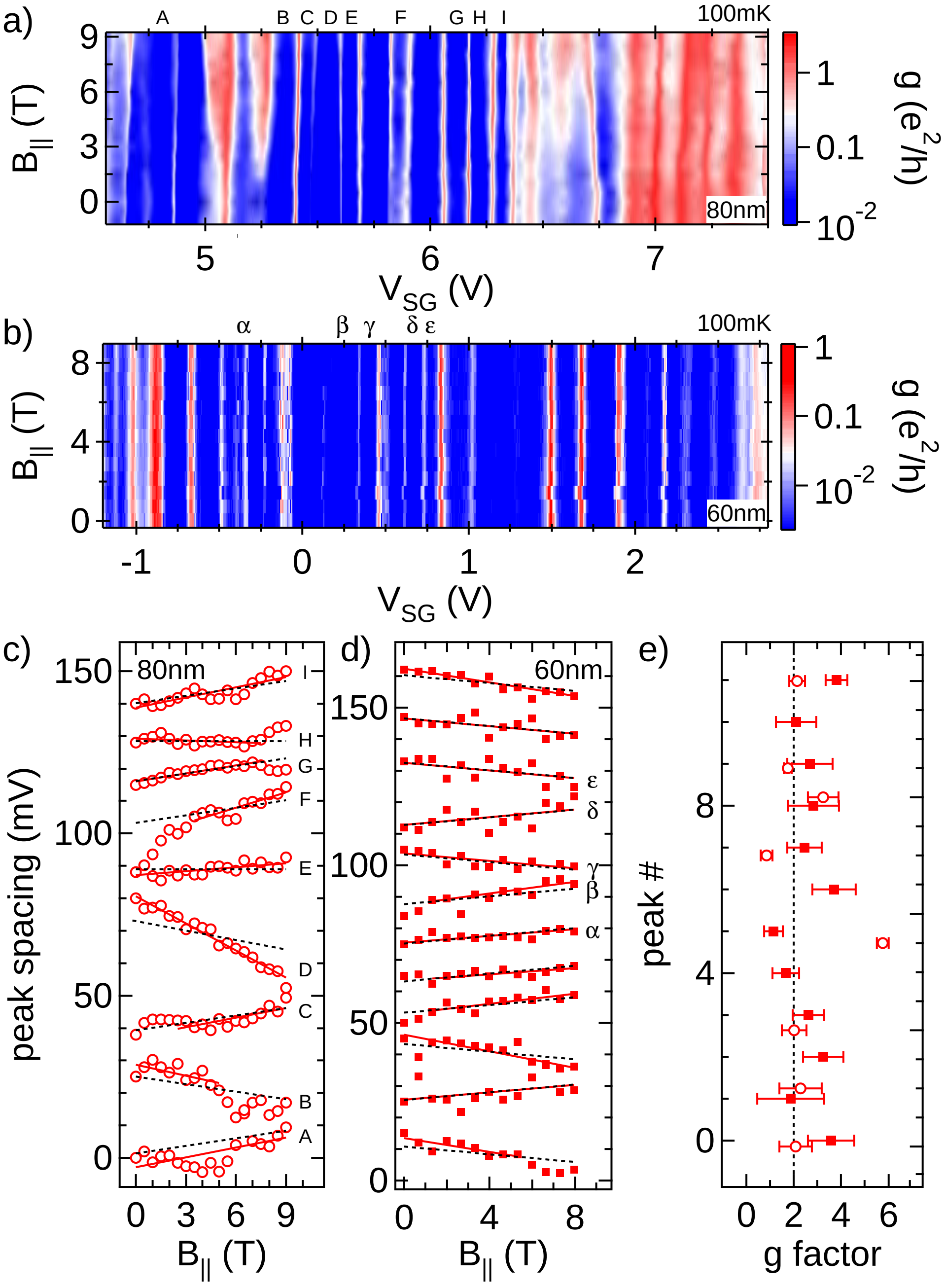

Figure 20: **(a),(b) CB peaks as a function of sidegate voltage and in-plane magnetic field** for the 80nm and 60nm dot, respectively ($T_e \approx 100$ mK). (c),(d) spacings for a selection of peaks from (a) and (b)(labeled A-I), which show a roughly linear evolution with $B_{||}$ (spacings are offset for clarity). Black dashed lines show slopes expected for the Zeeman effect with $g = 2$. (e) g factors extracted from line fits (solid red) to peak spacings in (c)(open circles) and (d)(closed squares). Vertical positions are offset to align with the according spacings in (c) and (d).

above, a slight $B_{\parallel}$ misalignment with a resulting $B_{\perp}$ component of $B_{\parallel}$ (a few degrees here) or other orbital coupling of $B_{\parallel}$, for examples by threading flux through the graphene surface ripples [216].

5.11 Extraction of the graphene g factor from Coulomb blockade peak splitting

In an attempt to avoid these $B_{\parallel}$ complications, we select peaks spacings approximately linear over a sufficiently large range of $B_{\parallel}$ without rejecting any slope, plotted in Figure 20c,d (offset for clarity), also labeled (A-I and α-ϵ) above their corresponding peaks in Figure 20a,b. We extract the slopes with best fits (solid red lines) and also indicate the closest standard slope (dashed black lines, slopes 0, $\pm g\mu_B$) for comparison, using the average lever arms previously measured from Coulomb diamonds of each dot. The resulting g-factors are summarized in Figure 20e for both dots. While in several cases, good agreement with the expected $g \sim 2$ is found (see e.g. A,B,C,G,I), we also notice horizontal, $B_{\parallel}$ independent peak spacings indicating non-trivial spin filling (e.g. E and H). Further, slopes strongly deviating from $g = 2$ are also seen, which is not surprising considering the $B_{\parallel}$ issues mentioned before. Nevertheless, averaging over the data in Figure 20e from both dots, we obtain $g = 2.7 \pm 1.1$ (excluding the obvious near-zero points?), consistent with $g = 2$ as expected and in line with other experiments [93, 217, 218].

5.12 Second summary

In summary, we have presented transport spectroscopy of graphene quantum dots on the same graphene flake with nearly identical disorder broadening. This allows a size comparison without changing disorder, displaying the expected size dependence of transport and Coulomb gaps as well as clear correlation between both, suggesting disorder induced localization as a physical origin for both effects. Even though the electron-hole transitions could not be precisely located (± few electrons) and the spin filling sequences were not fully tractable, both ultimately due to disorder, the average g-factor is consistent with $g = 2$, though with significant error bar. Overall, the combined data clearly draw a consistent picture of pronounced disorder effects which are masking the interesting low-density, few electron regime in these graphene devices. For future nano-graphene experiments, it will therefore be very important to investigate and suppress disorder, e.g. by removal of substrate [219] and adsorbate disorder, by a high degree of control over the graphene edges [88–90] and elimination of any residual intrinsic graphene defects.

The authors thank G. Burkhard and B. Trauzettel for helpful discussions. This work was supported by the University of Basel, the Swiss Nanoscience Institute (SNI), Swiss NSF, NCCR nano, and NCCR QSIT.

6 Summary and Outlook

Graphene nanostructures

All graphene nanostructures, including the ones presented in this thesis, show severe effects of disorder and thereby do not show much of the predicted specifics of graphene compared to conventional semiconductor quantum devices. On the contrary, in bulk graphene experiments, e.g. μm-sized Hall bar structures, where the influence of the edges is negligible graphene specific effects including a $\nu = 0$ insulating phase along with fractional quantum Hall states [220, 221] and a Zeeman-induced spin Hall effect [222, 223] have been observed in situations of reduced charge disorder. However, both charge and edge disorder have been shown to be a major problem for confined devices and applied fabrication techniques.

As pronounced charge disorder effects are seen in all kind of experiments on single-layer graphene devices, many groups have investigated possible ways around it. The first step mostly includes suspending the device by removing the substrate and with that the related charged impurities. In most samples this turned out to be not enough, as the graphene flakes usually get contaminated during processing with adsorbates and residues from resists. Therefore, current-annealing is regularly used to clean suspended devices via ohmic heating in vacuum [159]. This very promising procedure requires pretty good device robustness (e.g. current carrying capability) and therefore will always have a limited yield, especially for fragile graphene nanostructures. An alternative route might be to use ultra-clean and atomically flat hexagonal boron nitride crystals as a substrate material which has been shown to support very high mobility devices and is believed to reduce the inherent rippling of graphene flakes giving way to very small residual densities.

For graphene nanostructures also a series of studies concerning the fabrication of controlled edge termination has recently been started. As mentioned before, this includes physical methods like unzipping of carbon nanotubes [88], anisotropic dry-etching of graphene [89] and cautious exfoliation of natural GNRs relying on preferential cleavage along symmetry directions of the honeycomb structure [90, 91].

Preliminary experiments in the latter direction were done in our lab using a poly-

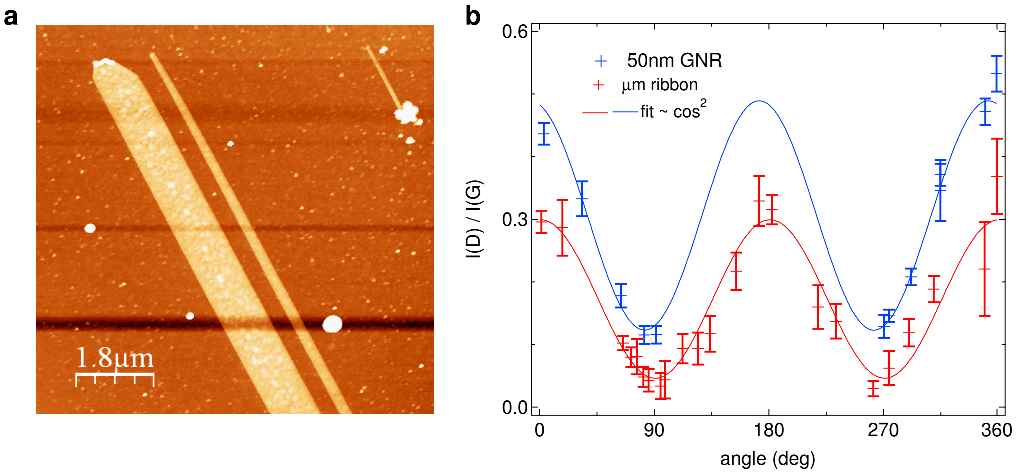

Figure 21: **Natural graphene nanoribbons with predominant armchair termination. a,** Atomic force microscopy image of three single-layer ribbons exfoliated with a PDMS stamp. The straight and aligned edges suggest a preferential cleaving direction. **b,** Relative intensity of the Raman D- and G-band for the 50nm and the 1 μm ribbon in **a** for various angles between excitation polarization and ribbon edges. As the D-mode is not active on clean zigzag edges and the data follows a $\cos^2$ dependence, this indicates mainly armchair edge termination of these ribbons.

dimethylsiloxane (PDMS) stamp instead of adhesive tapes to cleave and transfer graphene flakes from a graphite source. We regularly find ribbon-shaped few-layer graphene and graphite flakes with widths of several 100 nm and lengths up to 10 μm. Very rarely we can also identify single-layer GNRs with widths below 100 nm. Figure 21a shows an example of three such natural GNRs of 50nm, 200nm and 1μm width, respectively. The atomic force microscopy measurements in Fig. 21a suggest overall straight edges over almost the entire ribbon length.

Raman spectroscopy, see Fig. 21b, in dependence of the relative orientation of excitation polarization and ribbon edges further indicates a clear predominance of armchair termination for this device as the D-mode is not active at clean zigzag edges and the relative intensity $I(D)/I(G)$ of the graphene-specific Raman D- and G-band follows a $\cos^2$ dependence [224]. Nevertheless, the fact that $I(D)$ does not vanish for perpendicular polarization is a sign for either a principal armchair edge with saw-tooth ±60° armchair segments or edge disorder like point defects and edge reconstructions. Unfortunately, contacting with metallic electrodes using e-beam lithography (sample PDMS-II, see List of Samples - Appendix) resulted in insulating contacts, most likely due to residues covering the ribbon surface or due to problems arising from a possible

Schottky-barrier at the metal-GNR interface. However, this might be a comparably simple way to fabricate graphene nanostructures with a more controlled edge structure than what is achieved with etching through lithography defined masks.

More recently, some effort was put into the technique of anisotropic dry-etching in our group, namely by Dorothee Hug. Exposure of graphene to a hydrogen plasma has been shown to selectively etch away carbon atoms from armchair sites via hydrogenation of edge-atoms and methane formation [225]. The idea is to etch bulk graphene layers into zig-zag terminated structures starting from holes predefined via lithography and isotropic oxygen-plasma etching [89]. This method of edge structuring would allow a flexible and more controlled fabrication of different device structures and sizes when compared to the alternative approaches described above.

Nuclear spins in low-doped semiconductors

The breakdown of the Korringa law observed in our experiments might by taken as good or bad news, depending on the respective point of few. For the method of adiabatic demagnetization cooling, employed to cool semiconductor devices to ultra-low temperatures, the increase of the nuclear relaxation rate above the expectation from the Korringa law can be seen as an advantage as it enables faster equilibration between the electron and nuclear spin systems.

As the measured T_1 times are still extremely long ($\sim$ 1h) the slightly enhanced relaxation is of no significance even for schemes which rely on long nuclear lifetimes like usage of the nuclear spins as quantum memory [226]. Electron spin coherence, however, is limited not by the decay of the average nuclear polarization but by fluctuations of the local Overhauser field which would be suppressed only for fully polarized nuclear spins [12]. As 100% polarization is hard to realize but might be achievable in a ferromagnetic nuclear state possibly induced by RKKY-type interaction between nuclei mediated by the electrons in a 2DEG[227], it is interesting to look at the impact that interactions and disorder within the electron system have on the dynamics of the nuclear spins of the host lattice. The specific regime somewhat close to the MIT where we observe the unexpected nuclear relaxation, probably is most relevant for spin-coherent semiconductor devices as it provides extremely long electron spin lifetimes [228–230].

To substantiate our observations and gain detailed insight into the responsible relaxation mechanism a number of related experiments are possible.
First of all, nuclear spin relaxation times and especially their temperature dependence should be measured for increased doping densities. This would allow to find the transition to the Korringa-regime previously observed at $\mathrm{n} \sim 1 \times 10^{18}\,\mathrm{cm}^{-3}$ [183] and would enable a comparison with the evolution of other thermodynamic properties away from the MIT [31, 33]. Such experiments using the spin valve geometry and the measurement scheme introduced here are easily possible using an increased doping level in the bulk layer. The feasible density range might be limited as spin injection and detection across Schottky barriers will become difficult at high bulk densities due to the prerequisite of thin barriers with large contact resistances [162].

Second, the relaxation measurements could be extended to a wider magnetic field range to achieve further confidence on the amount of local correlation and the local field observed by each nucleus. This is easily possible by slight adaption of the measurement scheme presented here, which is by now limited to fields $\mathrm{B}_X \lesssim 2\,\mathrm{mT}$ below the coercive fields of the Fe contacts. For measurements of the relaxation in fields above the coercive fields one needs to re-align the magnetizations by an additional in-plane field sweep prior to the probe scans, which should not affect the measured relaxation times apart from intrinsic field dependencies.
Further, it would be interesting to measure the nuclear T_1 times at even lower temperatures using better thermalization in the dilution refrigerator or even more advanced cooling methods. This would allow to map out the temperature range in which nuclear relaxation by delocalized electrons dominates. At very low temperatures this will be ultimately limited by relaxation via fixed magnetic moments and nuclear spin diffusion.

The signatures of nuclear inhomogeneities and the not well-understood appearance of the double satellite peaks require further studies with different device geometries and layouts. Extending the ferromagnetic contacts over the full width of the active transport layer will help to avoid problems due to lateral charge current spread. Additionally, with the help of several, closely spaced Fe-contacts it would be possible to artificially create nuclear spin polarization patterns in a controlled way. This could provide important information on the detailed influence of inhomogeneity on the detected spin signals.

Ultimately, it would be very interesting to realize similar experiments in more confined structures like a GaAs/AlGaAs 2DEG, probably closer to actual spin-coherent devices, where interaction effects are generally stronger. Electrical spin injection and detection from ferromagnetic contacts into 2DEGs are currently suffering severe problems [1] but other methods like spin polarized currents from quantum point contacts as spin source [231] might open the way for interesting experiments probing the interplay of electron and nuclear spins in such systems.

Appendix - List of Samples

name	**picture**	**device info**
GI 2374-I (finished 08/12/08) [damaged]	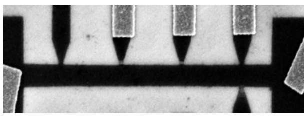	width = 1 μm length = 12 μm contact distance = 3 μm probe width = 260 nm
GI 2374-II (finished 20/01/09) [damaged]	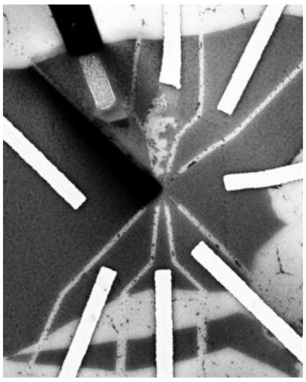	dot diameter = 35 nm barrier width = 20 nm trench width = 15 nm QPC width = 30 nm
GI 2374-III (finished 28/01/09) [damaged]	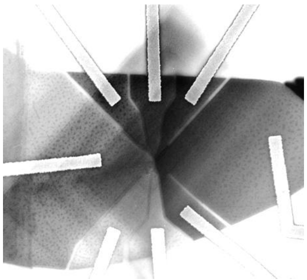	dot diameter = 50 nm barrier width = 35 nm QPC width = 30 nm
GI 2372 (finished 09/02/09)	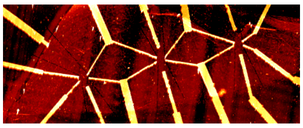	dot diameter = 43, 58, and 77 nm barrier width = 38, 55, and 70 nm trench width = 15-25 nm
GD016 (finished 27/11/08) [damaged]	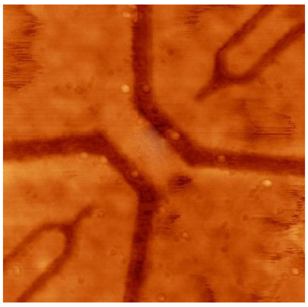	GNR width = 80 nm GNR length = 165 nm QPC width = 68 nm trench width = 65 nm
GD019 (finished 29/10/08) [damaged]		dot diameter = 35 nm barrier width = 25 nm QPC width = 30 nm

GD020 (finished 10/11/08) [damaged]	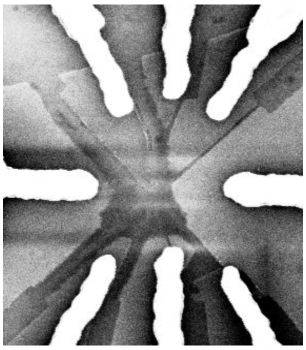	dot diameter = 35 nm barrier width = 25 nm QPC width = 30 nm
PDMS-II (finished 02/08/11) [insulating contacts]	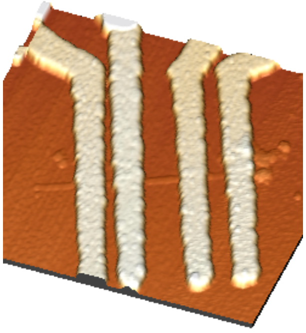	GNR width = 50 nm contact separation = 47, 130, and 250 nm contact width = 220 - 240 nm
IQEII A8_e-beam_D (finished 07/07/09) 2 devices	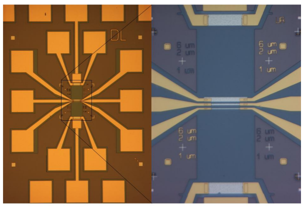	Fe-bar width = 1, 2, and 6 μm edge to edge = 4.5 and 3 μm length = 60 μm reference distance = 100 μm
IQEII A8_e-beam_CL (finished 07/07/09) 1 device	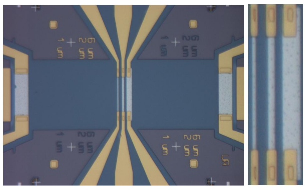	Fe-bar width = 1, 2, and 6 μm edge to edge = 4.5 and 6 μm length = 60 μm reference distance = 100 μm
IQEII A21bI (finished 24/02/11) unprocessed surface	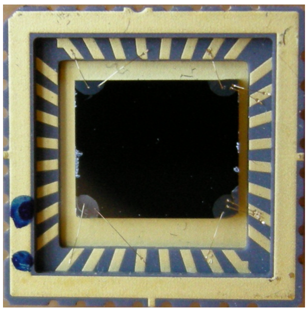	l_1 = 5.75 mm l_2 = 5.0 mm van der Pauw geometry

IQEII A21bII (finished 24/02/11) 5 min sputtered	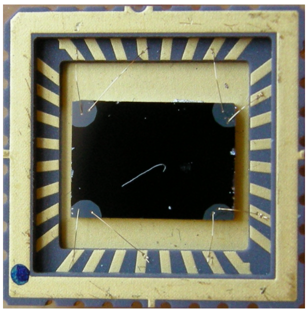	$l_1 = 5.75$ mm $l_2 = 4.1$ mm van der Pauw geometry

List of Figures

References

[1] D. D. Awschalom, D. Loss, and N. Samarth. *Semiconductor Spintronics and Quantum Computation.* Nanoscience and Technology (Springer-Verlag, Berlin, 2010). (Original work published in 2002).

[2] S. A. Wolf, D. D. Awschalom, R. A. Buhrman, J. N. Daughton, S. von Molnár, M. L. Roukes, A. Y. Chtchelkanova, and D. M. Treger. *Spintronics: A Spin-Based Electronics Vision for the Future.* Science **294**, 1488 (2001).

[3] A. M. Nielson and I. L. Chuang. *Quantum Computation and Quantum Information.* Cambridge Series on Information and the Natural Sciences (Cambridge University Press, Cambridge, 2000).

[4] D. DiVincenzo. *Quantum computation.* Science **270**, 255 (1995).

[5] D. Loss and D. DiVincenzo. *Quantum computation with quantum dots.* Phys. Rev. Lett. **57**, 120 (1995).

[6] I. Zutic, J. Fabian, and S. Das Sarma. *Spintronics: Fundamentals and applications.* Rev. Mod. Phys. **76**, 323 (2004).

[7] R. Hanson, L. P. Kouwenhoven, J. R. Petta, S. Tarucha, and L. M. K. Vandersypen. *Spins in few-electron quantum dots.* Rev. Mod. Phys. **79**, 1217 (2007).

[8] M. Eizenberg and J. M. Blakely. *Carbon monolayer phase condensation on Ni(111).* Surface Science **82**, 228 (1979).

[9] K. S. Novoselov, A. Geim, S. V. Morozov, D. Jiang, Y. Zhang, S. Dubonos, I. Grigorieva, and A. A. Firsov. *Electric Field Effect in Atomically Thin Carbon Films.* Science **306**, 666 (2004).

[10] C. Soldano, A. Mahmood, and E. Dujardin. *Production, properties and potential of graphene.* Carbon **48**, 2127 (2010).

[11] D. S. L. Abergel, V. Apalkov, J. Berashevich, K. Ziegler, and T. Chakraborty. *Properties of graphene: a theoretical perspective.* Adv. Phys. **59**, 261 (2010).

[12] J. Fischer, B. Trauzettel, and D. Loss. *Hyperfine interaction and electron-spin decoherence in graphene and carbon nanotube quantum dots.* Phys. Rev. B **80**, 155401 (2009).

[13] P. Recher and B. Trauzettel. *Quantum dots and spin qubits in graphene.* Nanotech. **21**, 302001 (2010).

[14] B. Trauzettel, D. V. Bulaev, D. Loss, and G. Burkard. *Spin qubits in graphene quantum dots.* Nat. Phys. **3**, 192 (2007).

[15] K. M. Svore, B. M. Terhal, and D. DiVincenzo. *Local fault-tolerant quantum computation.* Phys. Rev. A **72**, 022317 (2005).

[16] C. Ashby and A. Baca. *Fabrication of GaAs Devices.*, volume 6 of *EMIS Processing Series* (The Institution of Engineering and Technology, Cornwall, 2010).

[17] J. S. Blakemore. *Semiconducting and other major properties of gallium arsenide.* J. Appl. Phys **53**, R123 (1982).

[18] E. H. Hall. *On a New Action of the Magnet on Electric Currents.* American Journal of Mathematics **2**, 287 (1879).

[19] K. v. Klitzing, G. Dorda, and M. Pepper. *New Method for High-Accuracy Determination of the Fine-Structure Constant Based on Quantized Hall Resistance.* Phys. Rev. Lett. **45**, 494 (1980).

[20] D. C. Tsui, H. L. Stormer, and A. C. Gossard. *Two-Dimensional Magnetotransport in the Extreme Quantum Limit.* Phys. Rev. Lett **48**, 1559 (1982).

[21] B. J. van Wees, H. van Houten, C. W. J. Beenakker, J. G. Williamson, L. P. Kouwenhoven, D. van der Marel, and C. T. Foxon. *Quantized conductance of point contacts in a two-dimensional electron gas.* Phys. Rev. Lett **60**, 848 (1988).

[22] S. Amasha, K. MacLean, I. P. Radu, D. M. Zumbühl, M. A. Kastner, M. P. Hanson, and A. C. Gossard. *Electrical Control of Spin Relaxation in a Quantum Dot.* Phys. Rev. Lett **100**, 046803 (2008).

[23] J. R. Petta, A. C. Johnson, J. M. Taylor, E. A. Laird, A. Yacoby, M. D. Lukin, C. M. Marcus, M. P. Hanson, and A. C. Gossard. *Coherent Manipulation of Coupled Electron Spins in Semiconductor Quantum Dots.* Science **309**, 2180 (2005).

[24] K. C. Nowack, F. H. L. Koppens, Y. V. Nazarov, and L. M. K. Vandersypen. *Coherent Control of a Single Electron Spin with Electric Fields.* Science **318**, 1430 (2007).

[25] Y. Ohno, D. K. Young, B. Beschoten, F. Matsukura, H. Ohno, and D. D. Awschalom. *Electrical spin injection in a ferromagnetic semiconductor heterostructure.* Nature **402**, 790 (1999).

[26] R. Rentzsch, K. J. Friedland, A. N. Ionov, M. N. Matveev, I. S. Shlimak, C. Gladun, and H. Vinzelberg. *Variable-Range Hopping in Neutron-Transmutation-Doped Gallium Arsenide.* phys. stat. sol.(b) **137**, 691 (1986).

[27] J. R. Sites and A. K. Nedoluha. *GaAs impurity band transport in large magnetic fields.* Phys. Rev. B **24**, 4309 (1981).

[28] B. I. Shklovskii and A. L. Efros. *Electronic Properties of Doped Semiconductors.* Springer Series in Solid-State Sciences (Springer-Verlag, Berlin, 1984).

[29] N. F. Mott. *The Basis of the Electron Theory of Metals, with Special Reference to the Transition Metals* . Proc. Phys. Soc. A **62**, 416 (1949).

[30] P. W. Anderson. *Absence of Diffusion in Certain Random Lattices.* Phys. Rev. **109**, 1492 (1958).

[31] R. N. Bhatt. *Magnetic Properties of Doped Semiconductors.* Physica Scripta **T14**, 7 (1986).

[32] M. Milovanovic, S. Sachdev, and R. N. Bhatt. *Effective-Field Theory of Local-Moment Formation in Disordered Metals.* Phys. Rev. Lett. **63**, 82 (1989).

[33] M. A. Paalanen, J. E. Graebner, R. N. Bhatt, and S. Sachdev. *Thermodynamic Behavior near a Metal-Insulator Transition.* Phys. Rev. Lett. **61**, 597 (1988).

[34] M. Lakner, H. v. Löhneysen, A. Langenfeld, and P. Wölfle. *Localized magnetic moments in Si:P near the metal-insulator transition.* Phys. Rev. B **50**, 17064 (1994).

[35] R. N. Bhatt and D. S. Fisher. *Absence of Spin Diffusion in Most Random Lattices.* Phys. Rev. Lett. **68**, 3072 (1992).

[36] M. A. Paalanen, A. E. Ruckenstein, and G. A. Thomas. *Spins in Si:P Close to the Metal-Insulator Transition.* Phys. Rev. Lett. **54**, 1295 (1985).

[37] E. Miranda and V. Dobrosavljevic. *Disorder-driven non-Fermi liquid behaviour of correlated electrons.* Rep. Prog. Phys. **68**, 2337 (2005).

[38] A. H. Castro Neto, G. Castilla, and B. A. Jones. *Non-Fermi Liquid Behavior and Griffiths Phase in f-Electron Compounds.* Phys. Rev. Lett. **81**, 3531 (1998).

[39] V. Dobrosavljevic and G. Kotliar. *Dynamic mean-field studies of metal-insulator transitions.* Phil. Trans. R. Soc. Lond. A **356**, 57 (1998).

[40] R. Hanson, O. Gywat, and D. D. Awschalom. *Room-temperature manipulation and decoherence of a single spin in diamond.* Phys. Rev. B **74**, 161203 (2006).

[41] G. Balasubramanian, P. Neumann, D. Twitchen, M. Markham, R. Kolesov, N. Mizuochi, J. Isoya, J. Achard, J. Beck, J. Tissler, V. Jacques, P. R. Hemmer, F. Jelezko, and J. Wrachtrup. *Ultralong spin coherence time in isotopically engineered diamond.* Nature Materials **8**, 383 (2009).

[42] S. Iijima. *Helical microtubules of graphitic carbon.* Nature **354**, 56 (1998).

[43] H. W. Kroto, J. R. Heath, S. C. O'Brien, R. F. Curl, and R. E. Smalley. *C_{60}: Buckminsterfullerene.* Nature **318**, 162 (1985).

[44] Y. Zhang, Y.-W. Tan, H. L. Stormer, and P. Kim. *Experimental observation of the quantum Hall effect and Berry's phase in graphene.* Nature **438**, 201 (2005).

[45] K. S. Novoselov, A. Geim, S. V. Morozov, D. Jiang, M. I. Katsnelson, I. Grigorieva, S. Dubonos, and A. A. Firsov. *Two-dimensional gas of massless Dirac fermions in graphene.* Nature **438**, 197 (2005).

[46] M. I. Katsnelson and K. S. Novoselov. *Graphene: New bridge between condensed matter physics and quantum electrodynamics.* So. Stat. Comm **143**, 3 (2007).

[47] R. Saito, G. Dresselhaus, and M. S. Dresselhaus. *Physical Properties of Carbon Nanotubes.* (Imperial College Press, London, 1998).

[48] A. H. Castro Neto, F. Guinea, N. M. R. Peres, K. S. Novoselov, and A. K. Geim. *The electronic properties of graphene.* Rev. Mod. Phys. **81**, 109 (2009).

[49] P. R. Wallace. *The Band Theory of Graphite.* Phys. Rev. **71**, 622 (1947).

[50] D. C. Elias, R. V. Gorbachev, A. S. Mayorov, S. V. Morozov, A. A. Zhukov, P. Blake, L. A. Ponomarenko, I. V. Grigorieva, K. S. Novoselov, F. Guinea, and A. K. Geim. *Dirac cones reshaped by interaction effects in suspended graphene.* Nat. Phys. **7**, 701 (2011).

[51] V. Gavryushin. *Graphene Brillouin Zone and Electronic Energy Dispersion.* Wolfram Demonstrations Project (Wolfram, http://demonstrations.wolfram.com, 2012).

[52] D. P. DiVincenzo and E. J. Mele. *Self-consistent effective-mass theory for intralayer screening in graphite intercalation compounds.* Phys. Rev. B **29** (1984).

[53] M. I. Katsnelson, K. S. Novoselov, and A. K. Geim. *Chiral tunnelling and the Klein paradox in graphene.* Nat. Phys. **2**, 620 (2006).

[54] P. L. McEuen, M. Bockrath, D. H. Cobden, Y.-G. Yoon, and S. G. Louie. *Disorder, Pseudospins, and Backscattering in Carbon Nanotubes.* Phys. Rev. Lett. **83**, 5098 (1999).

[55] O. Klein. *Die Reflexion von Elektronen an einem Potentialsprung nach der relativistischen Dynamik von Dirac .* Z. Phys A **53**, 157 (1929).

[56] V. V. Cheianov and V. I. Fal'ko. *Selective transmission of Dirac electrons and ballistic magnetoresistance of n-p junctions in graphene.* Phys. Rev. B **74**, 041403 (2006).

[57] N. Stander, B. Huard, and D. Goldhaber-Gordon. *Evidence for Klein Tunneling in Graphene p-n Junctions.* Phys. Rev. Lett. **102**, 026807 (2009).

[58] J. Tworzydlo, B. Trauzettel, M. Titov, A. Rycerz, and C. W. J. Beenakker. *Sub-Poissonian Shot Noise in Graphene.* Phys. Rev Lett. **96**, 246802 (2006).

[59] M. I. Katsnelson. *Zitterbewegung, chirality, and minimal conductivity in graphene.* Eur. Phys. J. B **51**, 157 (2006).

[60] K. Ziegler. *Delocalization of 2D Dirac Fermions: The Role of a Broken Supersymmetry.* Phys. Rev Lett. **80**, 3113 (1998).

[61] A. W. W. Ludwig, M. P. A. Fisher, R. Shankar, and G. Grinstein. *Integer quantum Hall transition: An alternative approach and exact results.* Phys. Rev B **50**, 7526 (1994).

[62] Y.-W. Tan, Y. Zhang, K. Bolotin, Y. Zhao, S. Adam, E. H. Hwang, S. Das Sarma, H. L. Stormer, and P. Kim. *Measurement of Scattering Rate and Minimum Conductivity in Graphene.* Phys. Rev. Lett. **99**, 246803 (2007).

[63] K. Bolotin, K. J. Sikes, J. Hone, H. L. Stormer, and P. Kim. *Temperature-Dependent Transport in Suspended Graphene.* Phys. Rev. Lett. **101**, 096802 (2008).

[64] C. R. Dean, A. F. Young, I. Meric, C. Lee, L. Wang, S. Sorgenfrei, K. Watanabe, T. Taniguchi, P. Kim, K. L. Shepard, and J. Hone. *Boron nitride substrates for high-quality graphene electronics.* Nat. Nano. **5**, 722 (2010).

[65] S. Adam, E. H. Hwang, V. M. Galitsky, and S. Das Sarma. *A self-consistent theory for graphene transport.* PNAS **104**, 18392 (2007).

[66] J.-H. Chen, C. Jang, S. Adam, M. S. Fuhrer, and M. Williams, E. D.and Ishigami. *Charged-impurity scattering in graphene.* Nat. Phys. **4**, 377 (2008).

[67] J. Martin, N. Akerman, G. Ulbricht, T. Lohmann, J. H. Smet, K. von Klitzing, and A. Yacoby. *Observation of electron-hole puddles in graphene using a scanning single-electron transistor.* Nat. Phys. **4**, 144 (2008).

[68] S. Cho and M. S. Fuhrer. *Charge transport and inhomogeneity near the minimum conductivity point in graphene.* Phys. Rev. B **77**, 081402 (2008).

[69] S. V. Morozov, M. I. Novoselov, K. S. Katsnelson, F. Schedin, D. C. Elias, J. A. Jaszczak, and A. K. Geim. *Giant Intrinsic Carrier Mobilities in Graphene and Its Bilayer.* Phys. Rev. Lett. **100**, 016602 (2008).

[70] F. D. M. Haldane. *Model for a Quantum Hall Effect without Landau Levels: Condensed-Matter Realization of the "Parity Anomaly".* Phys. Rev. Lett. **61**, 2015 (1988).

[71] K. S. Novoselov, E. McKann, S. V. Morozov, V. I. Fal'ko, M. I. Katsnelson, U. Zeitler, D. Jiang, F. Schedin, and A. Geim. *Unconventional quantum Hall effect and Berry's phase of 2π in bilayer graphene.* Nat. Phys. **2**, 177 (2006).

[72] S. Y. Zhou, G.-H. Gweon, A. V. Fedorov, P. N. First, W. A. de Heer, D.-H. Lee, F. Guinea, A. H. Castro Neto, and A. Lanzara. *Substrate-induced bandgap opening in epitaxial graphene.* Nat. Mater. **6**, 770 (2007).

[73] E. Rotenberg, A. Bostwick, T. Ohta, J. L. McChesney, T. Seyller, and K. Horn. *Origin of the energy bandgap in epitaxial graphene.* Nat. Mater. **7**, 258 (2008).

[74] E. V. Castro, K. S. Novoselov, S. Morozov, N. M. R. Peres, J. M. B. Lopes dos Santos, J. Nilsson, F. Guinea, A. K. Geim, and A. H. Castro Neto. *Biased Bilayer Graphene: Semiconductor with a Gap Tunable by the Electric Field Effect.* Phys. Rev. Lett. **99**, 216802 (2007).

[75] J. B. Oostinga, H. B. Heersche, X. Liu, A. F. Morpurgo, and L. M. K. Vandersypen. *Gate-induced insulating state in bilayer graphene devices.* Nat. Mater. **7**, 151 (2007).

[76] C. Berger, Z. song, X. Li, X. Wu, N. Brown, C. Naud, D. Mayou, T. Li, J. Hass, A. N. Marchenkov, E. H. Conrad, P. N. First, and W. A. de Heer. *Electronic Confinement and Coherence in Patterned Epitaxial Graphene.* Science **312**, 1191 (2006).

[77] M. Y. Han, B. Özyilmaz, Y. Zhang, and P. Kim. *Energy Band-Gap Engineering of Graphene Nanoribbons.* Phys. Rev. Lett. **98**, 206805 (2007).

[78] Z. Chen, Y.-M. Lin, M. J. Rooks, and P. Avouris. *Graphene nano-ribbon electronics.* Physica E **40**, 228 (2007).

[79] F. Molitor, C. Stampfer, J. Güttinger, A. Jacobsen, T. Ihn, and K. Ensslin. *Energy and transport gaps in etched graphene nanoribbons.* Semicond. Sci. Technol. **25**, 034002 (2010).

[80] K. Nakada, M. Fujita, G. Dresselhaus, and M. S. Dresselhaus. *Edge state in graphene ribbons: Nanometer size effect and edge shape dependence.* Phys. Rev. B **54**, 17954 (1996).

[81] L. Brey and H. A. Fertig. *Electronic states of graphene nanoribbons studied with the Dirac equation.* Pys. Rev. B **73**, 235411 (2006).

[82] Y. W. Son, M. L. Cohen, and S. G. Louie. *Energy gaps in graphene nanoribbons.* Phys. Rev. Lett. **97**, 216803 (2006).

[83] Y. W. Son, M. L. Cohen, and S. G. Louie. *Half-metallic graphene nanoribbons.* Nature **444**, 347 (2006).

[84] L. Yang, C.-H. Park, Y. W. Son, M. L. Cohen, and S. G. Louie. *Quasiparticle Energies and Band Gaps in Graphene Nanoribbons.* Phys. Rev. Lett. **99**, 186801 (2007).

[85] C. . Girit, J. C. Meyer, R. Erni, M. D. Rossell, M. D. Kisielovski, L. Yang, C.-H. Park, M. F. Crommie, M. L. Cohen, S. G. Louie, and A. Zettl. *Graphene at the Edge: Stability and Dynamics .* Science **323**, 1705 (2009).

[86] E. R. Mucciolo, A. H. Castro Neto, and C. H. Lewenkopf. *Conductance quantization and transport gaps in disordered graphene nanoribbons.* Phys. Rev. B **79**, 075407 (2009).

[87] I. Martin and Y. M. Blanter. *Transport in disordered graphene nanoribbons.* Pys. Rev. B **79**, 235132 (2009).

[88] X. Wang, Y. Ouyang, L. Jiao, H. Wang, L. Xie, J. Wu, J. Guo, and H. Dai. *Graphene nanoribbons with smooth edges behave as quantum wires.* Nature Nanotech. **6**, 563 (2011).

[89] Z. Shi, R. Yang, L. Zhang, Y. Wang, D. Liu, D. Shi, E. Wang, and G. Zhang. *Patterning Graphene with Zigzag Edges by Self-Aligned Anisotropic Etching.* Adv. Mater. **23**, 3061 (2011).

[90] M. Moreno-Moreno, A. Castellanos-Gomez, G. Rubio-Bollinger, J. Gomez-Herrero, and N. Agrait. *Ultralong Natural Graphene Nanoribbons and Their Electrical Conductivity.* Small **5**, 924 (2009).

[91] Y. M. You, Z. H. Ni, T. Yu, and Z. X. Shen. *Edge chirality determination of graphene by Raman spectroscopy.* Appl. Phys. Lett. **93**, 163112 (2008).

[92] L. Ciric, A. Sienkiewicz, B. Náfrádi, M. Mionic', A. Magrez, and L. Forró. *Towards electron spin resonance of mechanically exfoliated graphene.* phys. stat. sol. B **246**, 2558 (2009).

[93] J. Güttinger, T. Frey, C. Stampfer, T. Ihn, and K. Ensslin. *Spin States in Graphene Quantum Dots.* Phys. Rev. Lett. **105**, 116801 (2010).

[94] L. M. Roth, B. Lax, and S. Zwerdling. *Theory of Optical Magneto-Absorption Effects in Semiconductors.* Phys. Rev. **114**, 90 (1959).

[95] G. Salis, Y. Kato, K. Ensslin, D. C. Driscoll, A. C. Gossard, and D. D. Awschalom. *Electrical control of spin coherence in semiconductor nanostructures.* Nature **414**, 619 (2001).

[96] M. Q. Weng and M. W. Wu. *Spin dephasing in n-type GaAs quantum wells.* Phys. Rev. B **68**, 075312 (2003).

[97] D. Stich, J. Zhou, T. Korn, R. Schulz, D. Schuh, W. Wegscheider, M. W. Wu, and C. Schüller. *Effect of Initial Spin Polarization on Spin Dephasing and the Electron g Factor in a High-Mobility Two-Dimensional Electron System.* Phys. Rev. Lett. **98**, 176401 (2007).

[98] S. Das Sarma, S. Adam, E. H. Hwang, and E. Rossi. *Electronic transport in two-dimensional graphene.* Rev. Mod. Phys. **83**, 407 (2011).

[99] A. N. Chantis, M. van Schilfgaarde, and T. Kotani. *Ab Initio Prediction of Conduction Band Spin Splitting in Zinc Blende Semiconductors.* Phys. Rev. Lett. **96**, 08640 (2006).

[100] H. Min, J. E. Hill, N. A. Sinitsyn, B. R. Sahu, L. Kleinman, and A. H. MacDonald. *Intrinsic and Rashba spin-orbit interactions in graphene sheets.* Phys. Rev. B **74**, 165310 (2006).

[101] M. Gmitra, S. Konschuh, C. Ertler, C. Ambrosch-Draxl, and J. Fabian. *Band-structure topologies of graphene: Spin-orbit coupling effects from first principles.* Phys. Rev. B **80**, 235431 (2009).

[102] D. Huertas-Hernando, F. Guinea, and A. Brataas. *Spin-orbit coupling in curved graphene, fullerenes, nanotubes, and nanotube caps.* Phys. Rev. B **74**, 155426 (2006).

[103] F. Kuemmeth, S. Ilani, D. C. Ralph, and P. L. McEuen. *Coupling of spin and orbital motion of electrons in carbon nanotubes.* Nature **452**, 448 (2008).

[104] M. Ishigami, J.-H. Chen, W. G. Cullen, M. S. Fuhrer, and E. D. Williams. *Atomic Structure of Graphene on SiO2.* Nano Lett. **7**, 1643 (2007).

[105] D. Paget, G. Lampel, B. Sapoval, and V. I. Safarov. *Low field electron-nuclear spin coupling in gallium arsenide under optical pumping conditions.* Phys. Rev. B **15**, 5780 (1977).

[106] W. Cai, R. D. Piner, F. J. Stadermann, S. Park, M. A. Shaibat, Y. Ishii, D. Yang, A. Velamakanni, S. J. An, M. Stoller, J. An, D. Chen, and R. S. Ruoff. *Synthesis and Solid-State NMR Structural Characterization of 13C-Labeled Graphite Oxide.* Science **321**, 5897 (2008).

[107] J. Fischer, M. Mircea Trif, W. A. Coish, and D. Loss. *Spin interactions, relaxation and decoherence in quantum dots.* Sol. Stat. Comm. **149**, 1443 (2009).

[108] F. Meier and B. P. Zakharchenya (edt.). *Optical Orientation.* Modern Problems in Condensed Matter Sciences (North-Holland, Amsterdam, 1984).

[109] R. J. Elliot. *Theory of the Effect of Spin-Orbit Coupling on Magnetic Resonance in Some Semiconductors.* Phys. Rev. **96**, 266 (1954).

[110] M. W. Wu and M. Q. Weng. *Spin dynamics in semiconductors.* Phys. Rep. **493**, 61 (2010).

[111] N. Tombros, C. Jozsa, M. Popinciuc, H. T. Jonkman, and B. J. van Wees. *Electronic spin transport and spin precession in single graphene layers at room temperature.* Nature **448**, 571 (2007).

[112] D. Huertas-Hernando, F. Guinea, and A. Brataas. *Spin-Orbit-Mediated Spin Relaxation in Graphene.* Phys. Rev. Lett. **103**, 146801 (2009).

[113] W. Han and R. K. Kawakami. *Spin Relaxation in Single-Layer and Bilayer Graphene.* Phys. Rev. Lett. **107**, 047207 (2011).

[114] T.-Y. Yang, J. Balakrishnan, F. Volmer, A. Avsar, M. Jaiswal, J. Samm, S. R. Ali, A. Pachoud, M. Zeng, M. Popinciuc, G. Güntherodt, B. Beschoten, and B. Özyilmaz. *Observation of Long Spin-Relaxation Times in Bilayer Graphene at Room Temperature.* Phys. Rev. Lett. **107**, 047206 (2011).

[115] G. E. Pikus and G. L. Bir. *Exchange Interaction in Excitons in Semiconductors.* Sov. Phys. JETP **33**, 108 (1971).

[116] J. Zhou and M. W. Wu. *Spin relaxation due to the Bir-Aronov-Pikus mechanism in intrinsic and p-type GaAs quantum wells from a fully microscopic approach.* Phys. Rev. B **77**, 075318 (2008).

[117] G. S. Uhrig. *Keeping a Quantum Bit Alive by Optimized π-Pulse Sequences.* Phys. Rev. Lett. **98**, 105044 (2007).

[118] J. Du, X. Rong, N. Zhao, Y. Wang, J. Yang, and R. B. Liu. *Preserving electron spin coherence in solids by optimal dynamical decoupling.* Nature **461**, 1265 (2009).

[119] T. Maassen, J. J. van den Berg, N. Ijbema, F. Fromm, T. Seyller, R. Yakimova, and B. J. van Wees. *Long Spin Relaxation Times in Wafer Scale Epitaxial Graphene on SiC(0001).* Nano Lett. **12**, 1498 (2012).

[120] A. Abragam. *Principles of Nuclear Magnetism.* International Series of Monographs on Physics; Vol. 32 (Oxford University Press, New York, 1961).

[121] C. P. Slichter. *Principles of magnetic resonance.* Solid State Sciences 1 (Springer, New York, 1990).

[122] M. Bucher. *The electron inside the nucleus: an almost classical derivation of the isotropic hyperfine interaction.* Eur. J. Phys. **21**, 19 (2000).

[123] E. Fermi. *Über die magnetischen Momente der Atomkerne .* Zeitschr. f. Phys. **60**, 320 (1930).

[124] A. W. Overhauser. *Polarization of Nuclei in Metals.* Phys. Rev. **92**, 411 (1953).

[125] W. A. Coish and J. Baugh. *Nuclear spins in nanostructures.* Phys. Stat. Sol. B **246**, 2203 (2009).

[126] Y. Ren, W. Yu, S. M. Frolov, J. A. Folk, and W. Wegscheider. *Nuclear polarization in quantum point contacts in an in-plane magnetic field.* Phys. Rev. B **81**, 125330 (2010).

[127] J. Strand, B. D. Schultz, A. F. Isakovic, C. J. Palmstrø m, and P. A. Crowell. *Dynamic Nuclear Polarization by Electrical Spin Injection in Ferromagnet-Semiconductor Heterostructures.* Phys. Rev. Lett. **91**, 036602 (2003).

[128] X. Lou, C. Adelmann, S. A. Crooker, E. S. Garlid, J. Zhang, K. S. Madhukar Reddy, S. D. Flexner, C. J. Palmstrø m, and P. A. Crowell. *Electrical detection of spin transport in lateral ferromagnet-semiconductor devices.* Nat. Phys. **3**, 197 (2007).

[129] G. Salis, A. Fuhrer, and S. F. Alvarado. *Signatures of dynamically polarized nuclear spins in all-electrical lateral spin transport devices.* Phys. Rev. B **80**, 115332 (2009).

[130] J. A. McNeil and W. G. Clark. *Nuclear quadrupolar spin-lattice relaxation in some III-V compounds.* Phys. Rev. B **13**, 4705 (1976).

[131] F. Bridges. *Calculation of the Temperature Dependence of the Nuclear Quadrupolar Spin-Lattice Relaxation Rate for InSb Using the Normal Coordinates of a Tetrahedron.* Phys. Rev. **164**, 299 (1967).

[132] W. E. Blumberg. *Nuclear Spin-Lattice Relaxation Caused by Paramagnetic Impurities.* Phys. Rev. **119**, 79 (1960).

[133] J. Korringa. *Nuclear magnetic relaxation and resonance line shift in metals.* Physica **16**, 601 (1950).

[134] D. Pines. *Electron Interaction in Metals.* Sol. Stat. Phys. **1**, 367 (1955).

[135] A. G. Anderson and A. G. Redfield. *Nuclear spin-lattice Relaxation in Metals.* Phys. Rev. **116**, 583 (1959).

[136] D. P. Tunstall and V. G. I. Deshmukh. *Conduction electrons in an impurity band: NMR in Ge:As .* J. Phys. C: Sol. Stat. Phys. **12**, 2295 (1979).

[137] M. Johnson and R. H. Silsbee. *Interfacial Charge-Spin Coupling: Injection and Detection of Spin Magnetization in Metals.* Phys. Rev. Lett. **55**, 1790 (1985).

[138] S. Datta and B. Das. *Electronic analog of the electro-optic modulator.* Appl. Phys. Lett. **56**, 665 (1990).

[139] J. Schliemann, J. C. Egues, and D. Loss. *Nonballistic Spin-Field-Effect Transistor.* Phys. Rev. Lett. **90**, 146801 (2003).

[140] H. C. Koo, J. H. Kwon, J. Eom, J. Chang, S. H. Han, and M. Johnson. *Detection of Spin-Polarized Electrons Injected into a Two-Dimensional Electron Gas.* Science **325**, 1515 (2009).

[141] G. Schmidt, D. Ferrand, L. W. Molenkamp, A. T. Filip, and B. J. van Wees. *Fundamental obstacle for electrical spin injection from a ferromagnetic metal into a diffusive semiconductor.* Phys. Rev. B **62**, R4790 (2000).

[142] S. F. Alvarado. *Tunneling Potential Barrier Dependence of Electron Spin Polarization.* Phys. Rev. Lett. **75**, 513 (1995).

[143] E. I. Rashba. *Theory of electrical spin injection: Tunnel contacts as a solution of the conductivity mismatch problem.* Phys. Rev. B **62**, R16267 (2000).

[144] A. Fert and H. Jaffrés. *Conditions for efficient spin injection from a ferromagnetic metal into a semiconductor.* Phys. Rev. B **64**, 184420 (2001).

[145] Z. W. Dong, R. Ramesh, T. Venkatesan, M. Johnson, Z. Y. Chen, S. P. Pai, V. Talyansky, R. P. Sharma, R. Shreekala, C. J. Lobb, and R. L. Greene. *Spin-polarized quasiparticle injection devices using* $Au/YBa_2Cu_3O_7/LaAlO_3/Nd_{0.7}Sr_{0.3}MnO_3$ *heterostructures.* Appl. Phys. Lett. **71**, 1718 (1997).

[146] V. Dediu, M. Murgia, F. Matacotta, C. Taliani, and S. Barbanera. *Room temperature spin polarized injection in organic semiconductor.* Sol. Stat. Comm. **122**, 181 (2002).

[147] H. J. Zhu, M. Ramsteiner, H. Kostial, M. Wassermeier, H.-P. Schönherr, and K. H. Ploog. *Room-Temperature Spin Injection from Fe into GaAs.* Phys. Rev Lett. **87**, 016601 (2001).

[148] P. Van Dorpe, W. Van Roy, J. De Boeck, and G. Borghs. *Nuclear spin orientation by electrical spin injection in an* $Al_xGa_{1-x}As/GaAs$ *spin-polarized light-emitting diode.* Phys. Rev. B **72**, 035315 (2005).

[149] J. Strand, X. Lou, C. Adelmann, B. D. Schultz, A. F. Isakovic, C. J. Palmstrø m, and P. A. Crowell. *Electron spin dynamics and hyperfine interactions in* $Fe/Al_{0.1}Ga_{0.9}As/GaAs$ *spin injection heterostructures.* Phys. Rev. B **72**, 155308 (2005).

[150] K. Ando, S. Takahashi, J. Ieda, H. Kurebajashi, T. Trypiniotis, C. H. W. Barnes, S. Maekawa, and E. Saitoh. *Electrically tunable spin injector free from the impedance mismatch problem.* Nature Mater. **10**, 655 (2011).

[151] M. Johnson and R. H. Silsbee. *Thermodynamic analysis of interfacial transport and of the thermomagnetoelectric system.* Phys. Rev. B **35**, 4959 (1987).

[152] F. J. Jedema, H. Heersche, A. T. Filip, J. J. A. Baselmans, and B. J. van Wees. *Electrical detection of spin precession in a metallic mesoscopic spin valve.* Nature **416**, 713 (2002).

[153] B. T. Jonker, A. T. Hanbicki, D. T. Pierce, and M. D. Stiles. *Spin nomenclature for semiconductors and magnetic metals.* J. Magn. Magn. Mater. **277**, 24 (2004).

[154] S. A. Crooker, M. Furis, X. Lou, C. Adelmann, D. L. Smith, C. J. Palmstrø m, and P. A. Crowell. *Imaging Spin Transport in Lateral Ferromagnet/Semiconductor Structures.* Science. **309**, 2191 (2005).

[155] G. Salis, A. Fuhrer, R. R. Schlittler, L. Gross, and S. F. Alvarado. *Temperature dependence of the nonlocal voltage in an Fe/GaAs electrical spin-injection device.* Phys. Rev B **81**, 205323 (2010).

[156] B. Endres, F. Hoffmann, C. Wolf, A. Einwanger, M. Utz, D. Schuh, G. Woltersdorf, M. Ciorga, D. Weiss, C. H. Back, and G. Bayreuther. *Bias dependence of spin injection into GaAs from Fe, FeCo, and (Ga,Mn)As contacts.* J. Appl. Phys. **109**, 07C505 (2011).

[157] A. N. Chantis, K. D. Belashchenko, D. L. Smith, E. Y. Tsymbal, M. van Schilfgaarde, and R. C. Albers. *Reversal of Spin Polarization in Fe/GaAs (001) Driven by Resonant Surface States: First-Principles Calculations.* Phys. Rev. Lett. **99**, 196603 (2007).

[158] B. D. Schultz, N. Marom, D. Naveh, X. Lou, C. Adelmann, J. Strand, P. A. Crowell, L. Kronik, and C. J. Palmstrø m. *Spin injection across the Fe/GaAs interface: Role of interfacial ordering.* Phys. Rev. B **80**, 201309 (2009).

[159] J. Moser, M. Zenger, C. Gerl, D. Schuh, R. Meier, P. Chen, G. Bayreuther, W. Wegscheider, D. Weiss, C.-H. Lai, R.-T. Huang, M. Kosuth, and H. Ebert. *Bias dependent inversion of tunneling magnetoresistance in Fe/GaAs/Fe tunnel junctions* . Appl. Phys. Lett. **89**, 162106 (2006).

[160] M. Ciorga, A. Einwanger, U. Wurstbauer, D. Schuh, W. Wegscheider, and D. Weiss. *Electrical spin injection and detection in lateral all-semiconductor devices.* Phys. Rev. B **79**, 165321 (2009).

[161] G. Salis, S. F. Alvarado, and A. Fuhrer. *Spin-injection spectra of CoFe/GaAs contacts: Dependece on Fe concentration, interface, and annealing conditions.* Phys. Rev B **84**, 041307 (2011).

[162] Q. O. Hu, E. Garlid, P. A. Crowell, and C. J. Palmstrø m. *Spin accumulation near Fe/GaAs (001) interfaces: The role of semiconductor band structure.* Phys. Rev B **84**, 085306 (2011).

[163] B. Endres, M. Ciorga, R. Wagner, S. Ringer, M. Utz, D. Bougeard, D. Weiss, C. H. Back, and G. Bayreuther. *Nonuniform current and spin accumulation in a 1 ?m thick n-GaAs channel .* Appl. Phys. Lett. **100**, 092405 (2012).

[164] J. Fabian, A. Matos-Abiague, C. Ertler, P. Stano, and I. Zutic. *Semiconductor Spintronics.* Acta Phys. Slov. **57**, 565 (2007).

[165] M. K. Chan, Q. O. Hu, J. Zhang, T. Kondo, C. J. Palmstrø m, and P. A. Crowell. *Hyperfine interactions and spin transport in ferromagnet-semiconductor heterostructures.* Phys. Rev. B **80**, 161206 (2009).

[166] C. Awo-Affouda, O. M. J. van 't Erve, G. Kioseoglou, A. T. Hanbicki, M. Holub, C. H. Li, and B. T. Jonker. *Contributions to Hanle lineshapes in Fe/GaAs nonlocal spin valve transport.* Appl. Phys. Lett. **94**, 102511 (2009).

[167] K. R. Wald, L. P. Kouwenhoven, P. L. McEuen, N. C. van der Vaart, and C. T. Foxon. *Local Dynamic Nuclear Polarization Using Quantum Point Contacts.* Phys. Rev. Lett. **73**, 1011 (1994).

[168] J. R. Petta, J. M. Taylor, A. C. Johnson, A. Yacoby, M. D. Lukin, C. M. Marcus, M. P. Hanson, and A. C. Gossard. *Dynamic Nuclear Polarization with Single Electron Spins.* Phys. Rev. Lett. **100**, 067601 (2008).

[169] K. Ono and S. Tarucha. *Nuclear-Spin-Induced Oscillatory Current in Spin-Blockaded Quantum Dots.* Phys. Rev. Lett. **92**, 256803 (2004).

[170] I. T. Vink, K. C. Nowack, F. H. L. Koppens, J. Danon, Y. N. Nazarov, and L. M. K. Vandersypen. *Locking electron spins into magnetic resonance by electron-nuclear feedback.* Nature Physics **5**, 764 (2009).

[171] C. Latta, A. Hogele, Y. Zhao, A. N. Vamivakas, P. Maletinsky, M. Kroner, J. Dreiser, I. Carusotto, A. Badolato, D. Schuh, W. Wegscheider, M. Atature, and A. Imamoglu. *Confluence of resonant laser excitation and bidirectional quantum-dot nuclear-spin polarization.* Nature Physics **5**, 758 (2009).

[172] H. Bluhm, S. Foletti, I. Neder, M. Rudner, D. Mahalu, V. Umansky, and A. Yacoby. *Dephasing time of GaAs electron-spin qubits coupled to a nuclear bath exceeding 200 μs.* Nature Physics **7**, 109 (2010).

[173] G. Yusa, K. Muraki, K. Takashina, K. Hashimoto, and Y. Hirayama. *Controlled multiple quantum coherences of nuclear spins in a nanometre-scale device.* Nature **434**, 1001 (2005).

[174] G. Lampel. *Nuclear Dynamic Polarization by Optical Electronic Saturation and Optical Pumping in Semiconductors.* Phys. Rev. Lett. **20**, 491 (1969).

[175] R. K. Kawakami, Y. Kato, M. Hanson, I. Malajovich, J. M. Stephens, E. Johnston-Halperin, G. Salis, A. C. Gossard, and D. D. Awschalom. *Ferromagnetic Imprinting of Nuclear Spins in Semiconductors.* Science **294**, 131 (2001).

[176] W. Farah, M. Dyakonov, D. Scalbert, and W. Knap. *Optically induced nuclear magnetic field in InP.* Phys. Rev. B **57**, 4713 (1998).

[177] R. J. Epstein, I. Malajovich, R. K. Kawakami, Y. Chye, M. Hanson, P. M. Petroff, A. C. Gossard, and D. D. Awschalom. *Spontaneous spin coherence in n-GaAs produced by ferromagnetic proximity polarization.* Phys. Rev. B **65**, 121202(R) (2002).

[178] W. D. Knight. *Nuclear Magnetic Resonance Shift in Metals.* Phys. Rev. **76**, 1259 (1949).

[179] R. K. Sundfors and D. F. Holcomb. *Nuclear Magnetic Resonance Studies of the Metallic Transition in Doped Silicon.* Phys. Rev. **136**, A810 (1964).

[180] G. Kaur and G. Denninger. *Dynamic Nuclear Polarization in III-V Semiconductors.* Appl. Magn. Reson. **39**, 185 (2010).

[181] O. V. Lounasmaa. *Experimental principles and methods below 1K.* (Academic Press, London, 1974).

[182] G. R. Pickett. *Microkelvin physics.* Rev. Prog. Phys. **51**, 1295 (1988).

[183] J. Lu, M. J. R. Hoch, P. L. Kuhns, W. G. Moulton, Z. Gan, and A. P. Reyes. *Nuclear spin-lattice relaxation in n-type insulating and metallic GaAs single crystals.* Phys. Rev. B **74**, 125208 (2006).

[184] B. L. Altschuler and A. G. Aronov. *Electron-Electron Interactions In Disordered Conductors.* Modern problems in condensed matter sciences; Vol 10 (North-Holland, Amsterdam, 1985).

[185] L. C. Hebel and C. P. Slichter. *Nuclear Spin Relaxation in Normal and Superconducting Aluminum.* Phys. Rev. **113**, 1504 (1959).

[186] H. K. Pal, V. I. Yudson, and D. L. Maslov. *Resistivity on non-Galilean-invariant Fermi- and non-Fermi liquids.* arXiv:1204.3591 (2012).

[187] B. S. Shastry and E. Abrahams. *What Does the Korringa Ratio Measure?* Phys. Rev. Lett. **72**, 1933 (1994).

[188] P. Fulde and A. Luther. *Effects of Impurities on Spin Fluctuations in Almost Ferromagnetic Metals.* Phys. Rev. **170**, 570 (1968).

[189] A. M. Finkel'shtein. *Spin fluctuations in disordered systems near the metal-insulator transition.* JETP Lett. **40**, 796 (1984).

[190] C. Castellani, C. DiCastro, P. A. Lee, M. Ma, S. Sorella, and E. Tabet. *Enhancement of the spin susceptibility in disordered interacting electrons and the metal insulator transition.* Phys. Rev. B **33**, 6169 (1986).

[191] D. Belitz and T. R. Kirkpatrick. *New phase of disordered Fermi systems.* Phys. Rev. B **44**, 955 (1991).

[192] H.-O. Lee and H.-Y. Choi. *Korringa ratio of ferromagnetically correlated impure metals.* Phys. Rev. B **62**, 15120 (2000).

[193] M. P. Sarachik, D. R. He, W. Li, and M. Levy. *Magnetic properties of boron-doped silicon.* Phys. Rev. B **31**, 1469 (1985).

[194] N. Manyala, J. F. DiTusa, G. Aeppli, and A. P. Ramirez. *Doping a semiconductor to create an unconventional metal.* Nature **454**, 976 (2008).

[195] K. Todd, H. Chou, S. Amasha, and D. Goldhaber-Gordon. *Quantum Dot Behavior in Graphene Nanoconstrictions.* Nano Lett. **9**, 416 (2009).

[196] L. A. Ponomarenko, F. Schedin, M. I. Katsnelson, R. Yang, E. W. Hill, K. S. Novoselov, and A. K. Geim. *Chaotic Dirac billiard in graphene quantum dots.* Science **320**, 356 (2008).

[197] X. Liu, J. B. Oostinga, A. F. Morpurgo, and L. M. K. Vandersypen. *Electrostatic confinement of electrons in graphene nanoribbons.* Phys. Rev. B. **80**, 121407 (2009).

[198] C. Stampfer, E. Schurtenberger, F. Molitor, J. Güttinger, T. Ihn, and K. Ensslin. *Tunable graphene single electron transistor.* Nano Lett. **8**, 2378 (2008).

[199] C. Stampfer, J. Güttinger, F. Molitor, D. Graf, T. Ihn, and K. Ensslin. *Tunable Coulomb blockade in nanostructured graphene.* Appl. Phys. Lett. **92**, 012102 (2008).

[200] P. Blake, E. W. Hill, A. H. Castro Neto, K. S. Novoselov, D. Jiang, R. Yang, T. J. Booth, and A. K. Geim. *Making graphene visible.* Appl. Phys. Lett. **91**, 063124 (2007).

[201] J. R. Williams, D. A. Abanin, L. Dicarlo, L. S. Levitov, and C. M. Marcus. *Quantum Hall conductance of two-terminal graphene devices.* Phys. Rev. B. **80**, 045408 (2009).

[202] F. Sols, F. Guinea, and A. H. Castro Neto. *Coulomb Blockade in Graphene Nanoribbons.* Phys. Rev. Lett. **99**, 166803 (2007).

[203] F. Molitor, A. Jacobsen, C. Stampfer, J. Güttinger, T. Ihn, and K. Ensslin. *Transport gap in side-gated graphene constrictions.* Phys. Rev. B. **79**, 075426 (2009).

[204] M. Evaldsson, I. Zozoulenko, H. Xu, and T. Heinzel. *Edge-disorder-induced anderson localization and conduction gap in graphene nanoribbons.* Phys. Rev. B. **78**, 161407 (2008).

[205] S. Schnez, F. Molitor, C. Stampfer, J. Güttinger, I. Shurobalko, T. Ihn, and K. Ensslin. *Observation of excited states in a graphene quantum dot.* Appl. Phys. Lett. **94**, 012107 (2009).

[206] C. Stampfer, J. Güttinger, S. Hellmüller, F. Molitor, K. Ensslin, and T. Ihn. *Energy Gaps in Etched Graphene Nanoribbons.* Phys. Rev. Lett. **102**, 056403 (2009).

[207] J. Güttinger, C. Stampfer, F. Libisch, T. Frey, J. Burgdörfer, T. Ihn, and K. Ensslin. *Electron-Hole Crossover in Graphene Quantum Dots.* Phys. Rev. Lett. **103**, 046810 (2009).

[208] S. Neubeck, L. A. Ponomarenko, F. Freitag, A. J. M. Giesbers, U. Zeitler, S. V. Morozov, P. Blake, A. K. Geim, and K. S. Novoselov. *From One Electron to One Hole: Quasiparticle Counting in Graphene Quantum Dots Determined by Electrochemical and Plasma Etching.* Small **6**, 1469 (2010).

[209] L.-J. Wang, G. Cao, T. Tu, H.-O. Li, C. Zhou, X.-J. Hao, G.-C. Guo, and G.-P. Guo. *Ground States and Excited States in a Tunable Graphene Quantum Dot.* Chin. Phys. Lett. **28**, 067301 (2011).

[210] S. Dröscher, H. Knowles, Y. Meir, K. Ensslin, and T. Ihn. *Coulomb gap in graphene nanoribbons.* Phys. Rev. B **84**, 073405 (2011).

[211] F. Molitor, S. Dröscher, J. Güttinger, A. Jacobsen, C. Stampfer, T. Ihn, and K. Ensslin. *Transport through graphene double dots.* Appl. Phys. Lett. **94**, 222107 (2009).

[212] W. G. van der Viel, S. De Franceschi, J. M. Elzerman, T. Fujisawa, S. Tarucha, and L. P. Kouwenhoven. *Electron transport through double quantum dots.* Rev. Mod. Phys. **75**, 1 (2003).

[213] P. Recher, J. Nilsson, G. Burkard, and B. Trauzettel. *Bound states and magnetic field induced valley splitting in gate-tunable graphene quantum dots.* Phys. Rev. B. **79**, 085407 (2009).

[214] F. Libisch, S. Rotter, J. Güttinger, C. Stampfer, and J. Burgdörfer. *Transition to Landau levels in graphene quantum dots.* Phys. Rev. B. **81**, 245411 (2010).

[215] J. A. Folk, C. M. Marcus, R. Berkovits, I. L. Kurland, I. L. Aleiner, and B. L. Altshuler. *Ground state spin and Coulomb blockade peak motion in chaotic quantum dots.* Phys. Scr. **T90**, 26 (2001).

[216] M. B. Lundeberg and J. A. Folk. *Rippled Graphene in an In-Plane Magnetic Field: Effects of a Random Vector Potential.* Phys. Rev. Lett. **105**, 146804 (2010).

[217] M. B. Lundeberg and J. A. Folk. *Spin-resolved quantum interference in graphene.* Nat. Phys. **5**, 894 (2009).

[218] S. S. Rao, A. Stesmans, K. Keunen, D. V. Kosynkin, A. Higginbotham, and J. M. Tour. *Unzipped graphene nanoribbons as sensitive O_2 sensors: Electron spin resonance probing and dissociation kinetics.* Appl. Phys. Lett. **98**, 083116 (2011).

[219] N. Tombros, A. Veligura, J. Junesch, M. H. D. Guimaraes, I. J. Vera-Marun, H. T. Jonkman, and B. J. van Wees. *Quantized conductance of a suspended graphene nanoconstriction.* Nat. Phys. **7**, 697 (2011).

[220] X. Du, I. Skachko, F. Duerr, and E. A. Luican, A. Andrei. *Fractional quantum Hall effect and insulating phase of Dirac electrons in graphene .* Nature **462**, 192 (2009).

[221] K. Bolotin, F. Ghahari, M. D. Shulman, H. L. Stormer, and P. Kim. *Observation of the fractional quantum Hall effect in graphene.* Nature **462**, 196 (2009).

[222] D. A. Abanin, S. V. Morozov, L. A. Ponomarenko, R. V. Gorbachev, A. S. Mayorov, M. I. Katsnelson, K. Watanabe, T. Taniguchi, K. S. Novoselov, L. S. Levitov, and A. K. Geim. *Giant Nonlocality Near the Dirac Point in Graphene.* Science **332**, 328 (2011).

[223] C.-L. Chen, C.-R. Chang, and B. K. Nikolić. *Quantum coherence and its dephasing in the giant spin Hall effect and nonlocal voltage generated by magnetotransport through multiterminal graphene bars.* Science **332**, 328 (2011).

[224] C. Casiraghi, A. Hartschuh, H. Qian, S. Piscanec, C. Georgi, A. Fasoli, K. S. Novoselov, D. M. Basko, and A. C. Ferrari. *Raman Spectroscopy of Graphene Edges.* Nano Lett. **9**, 1433 (2009).

[225] R. Yang, L. Zhang, Y. Wang, Z. Shi, D. Shi, H. Gao, E. Wang, and G. Zhang. *An Anisotropic Etching Effect in the Graphene Basal Plane.* Adv. Mater. **22**, 4014 (2010).

[226] J. M. Taylor, C. M. Marcus, and M. D. Lukin. *Long-Lived Memory for Mesoscopic Quantum Bits.* Phys. Rev. Lett **90**, 206803 (2003).

[227] P. Simon and D. Loss. *Nuclear Spin Ferromagnetic Phase Transition in an Interacting Two Dimensional Electron Gas.* Phys. Rev. Lett. **98**, 156401 (2007).

[228] J. M. Kikkawa and D. D. Awschalom. *Resonant Spin Amplification in n-Type GaAs.* Phys. Rev. Lett. **80**, 4313 (1998).

[229] J. M. Kikkawa and D. D. Awschalom. *Lateral drag of spin coherence in gallium arsenide.* Nature. **397**, 139 (1999).

[230] L. Schreiber, M. Heidkamp, T. Rohleder, B. Beschoten, and G. Güntherodt. *Mapping of spin lifetimes to electronic states in n-type GaAs near the metal-insulator transition.* arXiv 0706.1884 (2007).

[231] S. M. Frolov, A. Venkatesan, W. Yu, and J. A. Folk. *Electrical Generation of Pure Spin Currents in a Two-Dimensional Electron Gas.* Phys. Rev. Lett. **102**, 116802 (2009).

Curriculum Vitae

Dominikus Kölbl

1992 - 2001	Ignaz-Günther Gymnasium, Rosenheim
2001 - 2002	civil service, Klinikum Rosenheim
2002 - 2007	studies at the University of Augsburg
Dec. 2007	Diploma in physics
2008 - 2012	PhD at University of Basel

My academic education is based on lectures by:

B. Bauer, R. Claessen, J. Ebbecke, U. Eckern, S. Horn, P. Hänggi, G.-L. Ingold, H. Kielhöfer, T. Kopp, A. Krimmel, D. Loss, J. Ritter, W. Scherer, R. Tidecks, D. Vollhardt, W. Vogler, A. Wixforth

Publications

D. KÖLBL, J. EBBECKE, A. HEINRICH, and A. WIXFORTH , *Self-aligned growth of carbon nanosticks.* Nanotechnology **19**, 485304 (2008)

D. KÖLBL, D. M. ZUMBÜHL , *Transport spectroscopy of disordered graphene quantum dots etched into a single graphene flake* in prep. for submission to Nano Letters

D. KÖLBL, D. M. ZUMBÜHL, A. FUHRER, G. SALIS, and S. F. ALVARADO , *Breakdown of the Korringa Law of Nuclear Spin Relaxation in Metallic GaAs.* Phys. Rev. Lett. **109**, 086601 (2012)